Light emission in complex networks from single-photons to lasing

Gaio, Michele

Awarding institution:
King's College London

Light emission in complex networks from single-photons to lasing

Michele Gaio

A Thesis submitted in partial fulfilment of the requirements
for the degree of Doctor of Philosophy

Supervisor: Dr. Riccardo Sapienza
Examiners: Prof. Stefan Maier
Prof. William L. Barnes

School of Natural and Mathematical Sciences
Department of Physics
King's College London

June 2016

Abstract

Light-matter interaction, which is at the heart of the science and technology of light, can be controlled and designed in materials structured at the nanometre length-scale, for enhanced light emission and absorption, and down to the single photon level.

The aim of this thesis is to investigate complex photonic geometries, i.e. systems where the collective interaction of a large number of constituents defines the optical properties with emergent phenomena beyond the sum of the response of the individual constituents. In particular, a central topic is the emission of light from sources located in dielectric and plasmonic networks with different degree of disorder and correlation. Experimental and theoretical evidence of coupling of single photons to propagating modes in nano-waveguides, emission enhancement in plasmonic structures, and collective emission in disordered lasing systems are presented.

Large coupling of individual quantum dots embedded in free-standing sub-wavelength waveguides is experimentally demonstrated. These waveguides are fabricated by electrospinning, a scalable technique suitable for the realisation of large interconnected systems.

Light emission enhancement is investigated in plasmonic self-assembled systems and lithographic structures, which build on the framework of optical antennas and allows isolating local and global contributions to the local density of states around a topological percolation phase transition.

One of the most important cooperative effects between multiple emitters is lasing. Random lasing is investigated numerically and experimentally in diffusive systems with particular attention to the spectral properties of the emission and its relation with the physical and chemical parameters of the surrounding environment, which can be exploit to tune the lasing emission, thus providing a novel sensing scheme. These results provide the building blocks to construct a photonic network of emitters coupled by simple optical links.

Contents

List of publications

Part of the work presented was published or submitted for publication:

- Gaio, M., Castro-Lopez, M., Renger, J., van Hulst, N., and Sapienza, R., Percolating plasmonic networks for light emission control. Faraday Discuss., **178**, 237–252 (2015). http://doi.org/10.1039/C4FD00187G
- Gaio, M., Peruzzo, M., and Sapienza, R, Tuning random lasing in photonic glasses. Optics Letters, **40** (7), 1611–1614 (2015). http://doi.org/10.1364/OL.40.001611
- Gaio, M., Moffa, M., Castro-Lopez, M., Pisignano, D., Camposeo, A., and Sapienza, R., Modal coupling of single photons to a nanofibre. ACS Nano, 2016, **10** (6), 6125–6130 (2016). http://doi.org/10.1021/acsnano.6b02057
- Caixeiro, S., Gaio, M., Marelli B., Omenetto F. G., and Sapienza R., Silk-based Biocompatible Random Lasing. Advanced Optical Materials 4:998–1003 (2016) http://doi.org/10.1002/adom.201600185
- Gaio, M., Caixeiro, S., Marelli B., Omenetto F. G., and Sapienza R., Gain based random lasing sensing (Submitted) https://arxiv.org/abs/1608.06303

1 Introduction

In the last few decades, the study of light at the nanometre scale has seen a rapid development driven by miniaturisation and by the advances in technology, such as high-resolution lithography and microscopy techniques, that allowed to measure and fabricate structures with features of size near and beyond the wavelength of light. Similarly to how the ability to manipulate the electronic components has allowed the huge development of the electronic industry, the efficient manipulation of light-matter interaction at the nanoscale is a fundamental requirement for a variety of optical devices, including sensing, metrology, and quantum information [1].

Fluorescent emitters, as for example molecules and quantum dots which driven by an external laser pulse can emit light by spontaneous emission, are ideal local sources of light. In fact, while the limit of classical light confinement, i.e. by means of lenses, objectives or other focusing optics, is of the order of half the wavelength of light and it is typically achieved with an high numerical aperture objective and a laser beam, fluorescent emitters instead have dimensions much smaller than the wavelength of the radiation and can couple efficiently to the local excitations, making them ideal local excitation and probe channels. Working with localised emitters thus has the intrinsic advantage to access the local properties with very high spatial accuracy, as it has been done for instance to measure magnetic fields and temperature [2]. This local probing features are particularly effective when investigating nanostructures, in particular plasmonic systems for which the optimized behaviour is often restricted to specific structure locations. Probing the structure with localized emitters therefore allows to avoid the averaging effect of far-field techniques or expose the rare extreme events when spatially sampling the system properties, with resolution otherwise achievable only with near-field probing (SNOM) and electronic based techniques, such as cathodoluminescence and electron energy loss spectroscopy (EELS).

Individual fluorescent sources with a single electron excitation, as for example vacancies in solid states systems [3], semiconductor quantum dots [4], molecules [5], and trapped atoms [6] and ions [7], are also particularly appealing as they are

sources of single photons [8]. Photons are a candidate for the transport of quantum information encoded into their degrees of freedom such as polarization and energy, which can then travel over long distances interacting weakly with the environment. Indeed, upon excitation with a laser pulse and subsequent relaxation, fluorescent emitters can produce deterministically single photons (assuming close to unity extraction and quantum efficiency) which can be used to implement quantum information schemes [9].

Nevertheless, due to size mismatch between the emitter size and the radiation wavelength, point-like sources interact slowly with radiation, limiting absorption and emission; their omni-directional dipolar emission reduces the photon transport to practically zero for distances larger than a few wavelengths, and thus poses great constraints to their practical use. Therefore, one of the key requirement for the development of photonic devices interfaced with single emitters is the ability to enhance the coupling between the emitter and the optical states, for instance to achieve non-linear process [10] or to realise transistors and switches at the single photon level [11, 12]. In particular, obtaining long-range coupling between remote emitters would be a key step for the realisation of more complex platforms towards fully quantum networks [13, 14].

Nanostructuring matter below the length-scale of the wavelength allows to engineer the optical states and exploit scattering and interference in the near-field regime to achieve high fields confinement with enhanced light-matter interaction. Compared to the conventional quantum optics approach which consists in surrounding the emitter with micrometer-sized high-finesse microcavities [15], nanoscale modal engineering is typically broadband, allowing to work efficiently at room-temperature, a key step toward practical quantum-technology. Moreover, nano-optics tools are flexible and robust, allowing diverse applications such as imaging and sensing, and can provide larger opportunity of scalability.

In this work we will investigate light emission and transport with particular interest to complex systems, i.e. systems characterised by a large number of interacting components. The aim is to focus on those properties arising from the collective mutual interaction of the system components, considering global features of extended systems, such as the interplay between disorder and correlations, beyond their local details as for example the shape and dimensions of a nanoparticle, which nonetheless have to be controlled for their experimental realisation. Therefore, this requires the investigation of light behaviour at different scales: from the sub-nanometre atomic length-scale of an emitter, to the nanometre optical length-scale of its emitter near-field, to the length-scale of its interaction with the optical

environment, up to a macroscopic scale sized (~millimetres) architectures. In this introductory chapter we first revise few important concepts and tools used throughout this work.

1.1 Light emission from dipolar sources

Fluorescence is the spontaneous emission of light associated with an electronic transition in an atom, a molecule or a quantum system from an excited level to the ground state. The excited electron is usually promoted to an excited level due to the absorption of a photon. The electron then undergoes internal non-radiative transitions before returning back to the ground state by emitting a photon at a lower energy. The typical time-scale of the transition is of the order of 1–10 ns. At room temperature, which is the conditions of all systems studied in this thesis, the excited state coherence time in our system is sub-picosecond, therefore the spontaneously emitted light has no phase relation with the exciting one. We describe this as an incoherent emission process, unlike for instance scattering and stimulated emission. Fluorescence is found in many organic and inorganic molecules and in artificial semiconductor structures like quantum-dots (QDs) an it is described by different properties: the emission spectrum, the quantum yield (the ratio of the number of photons emitted to the number of photons absorbed) and the lifetime of the excited state τ. These are all influenced by the photonic environment in which the emitters are placed.

In fact, the transition from the emitter excited state to the ground level is a purely quantum-mechanical phenomenon driven by vacuum fluctuations. This can be pictured in terms of the Fermi's Golden Rule: the transition rate Γ ($\Gamma = 1/\tau$) from the initial state $|i\rangle$ to any final state $|f\rangle$ is given by [16]

$$\Gamma = \frac{2\pi}{\hbar}\sum_f |\langle f|\hat{H}'|i\rangle|^2 \delta(E_i - E_f) = \frac{2\pi}{\hbar}\sum_f |M_{if}|^2 \delta(E_i - E_f) \tag{1.1}$$

where $\hat{H}'$ is the time-dependent Hamiltonian perturbation term describing the electromagnetic interaction and each final available state $|f\rangle$ is a state of the complete emitter-radiation system, while the δ-function ensures energy conservation. Equation (1.1) states that the transition rate depends on the available decay channels $|f\rangle$ and on the matrix elements $|M_{if}|$ dependent on the interaction with the radiation states. In this picture the spontaneous emission decay rate can be decreased by removing optical states coupled to the emission wavelength or increased by adding states or enhancing their coupling to the emitter, which can

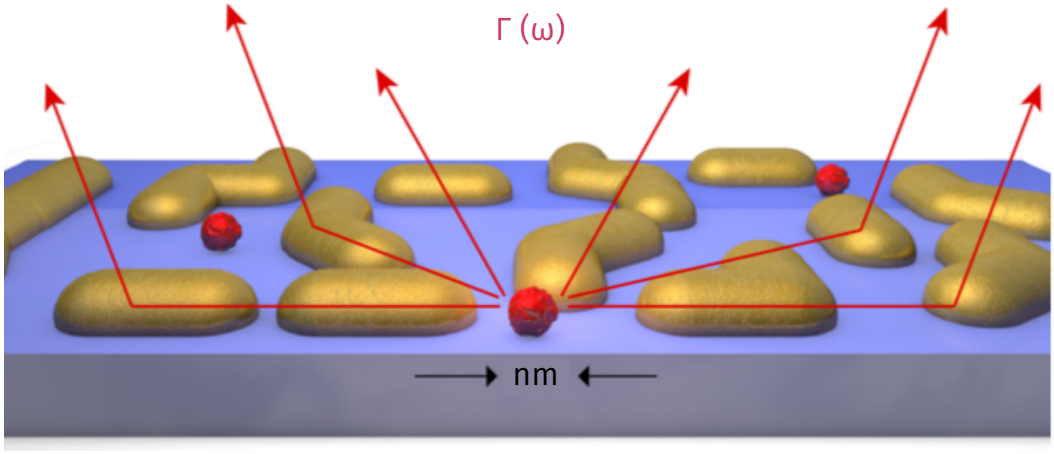

Figure 1.1: **Light emission in nanostructured materials**. Light emission by a fluorescent molecule in plasmonic system is partially mediated by the structure optical modes.

be obtained in nanostructured systems (Figure 1.1). This is for instance achieved in photonic crystals, periodic arrangements of dielectric scatterers, in which the destructive interference prevent light from propagating at certain energies and direction which define an optical band-gap; the decay of a spontaneous emitter with energy in this band-gap is thus inhibited. Conversely, close to the band edge where the density of states is larger a decay rate enhancement is expected [17].

1.1.1 Dipolar quantum emitters

In order to describe light radiation, we need first to consider the electronic transition from which it originates. Most electronic transitions are described as dipolar transitions. In fact, the size of the emitter, i.e the extension of atomic or molecular orbitals, is negligible when compared to the wavelength of the electromagnetic radiation. Therefore, in the the electromagnetic linear interaction Hamiltonian term [16]

$$\hat{H}' = e\,\hat{\boldsymbol{A}}(\omega,\boldsymbol{x})\cdot\hat{\mathbf{p}}, \tag{1.2}$$

where e is the the electron charge and $\hat{\boldsymbol{p}}$ is the momentum operator, the vector potential can be considered constant across the atomic dimensions ($\hat{\boldsymbol{A}}(\boldsymbol{x}) = \hat{\boldsymbol{A}}(0) = \hat{\boldsymbol{A}}_0$). It can be shown [18] that Equation (1.2) can be expressed as

$$\hat{H}' = e\,\hat{\boldsymbol{r}}\cdot\hat{\boldsymbol{E}}_0, \tag{1.3}$$

where $\hat{\boldsymbol{\mathcal{E}}}_0$ is the electric field operator at the emitter position. The electronic component of the transition matrix elements in Equation (1.1) therefore contains

term of the form $M_{ab} = \langle\psi_a|\hat{\boldsymbol{r}}|\psi_b\rangle \cdot \hat{\boldsymbol{E}}_0$ between two electronic states $|\psi_a\rangle$ and $|\psi_b\rangle$:

$$M_{ab} \propto e\langle\psi_a|\hat{\boldsymbol{r}}|\psi_b\rangle. \tag{1.4}$$

The terms $\langle\psi_a|e\hat{\boldsymbol{r}}|\psi_b\rangle$ has the form of the matrix element of a dipole moment operator $\hat{\boldsymbol{D}} = -e\hat{\boldsymbol{r}}$. The transition dipole $\hat{\boldsymbol{D}}_{ab}$ and its interaction with the electromagnetic fields, i.e. the field intensities along the dipole axis in the position of the dipole, defines the strength and thus the rate of the transition:

$$\Gamma \propto |M_{ab}|^2 \propto |\hat{\boldsymbol{D}}_{ab} \cdot \hat{\boldsymbol{\epsilon}}_0|^2. \tag{1.5}$$

Due to energy and momentum conservation or reason of symmetries between the electronic states ("selection rules") the dipolar transition might be forbidden, i.e the dipole elements $\hat{\boldsymbol{D}}_{ab}$ might vanish. In such cases higher order terms corresponding for instance to magnetic dipoles and electrical quadrupoles transitions, become important. While typically electric dipolar transitions dominate at optical frequencies, naturally occurring magnetic dipole transitions can be found for instance in some rare earth ions [19] (an example will be shown in Section 1.4), and are the main component for example of common fluorescent lamps.

The transition dipole $\hat{\boldsymbol{D}}_{ab}$ is solely an electronic property of the emitter and is not related to the electromagnetic environment as long as the dipolar approximation holds (in principle the assumptions of slowly varying fields on the emitter length-scale may not hold in the presence of nanostructures) and the electronic orbitals do not change. The electromagnetic components ($\hat{\boldsymbol{E}}_0$) can be accounted with a semi-classical treatment in the case of absorption and stimulated emission from an external field, while a QED approach with the quantization of the fields is required to rigorously derive the spontaneous emission. Nevertheless, also the latter turns out to be related to its classical counterpart, that is the radiation of a classical dipole, which will be describe it in the next section.

1.1.2 Radiation of a classical dipole

The radiation of a classical electric dipole $\boldsymbol{p}(t) = q[\boldsymbol{r}(t) - \boldsymbol{r}_0]$, i.e. the radiation from a point-like current $\boldsymbol{j}(\boldsymbol{r}, t) = \frac{d}{dt}\boldsymbol{p}(t)\delta(\boldsymbol{r} - \boldsymbol{r'})$ is given, assuming harmonic time dependence with frequency ω and wavevector $\boldsymbol{k}$, by the solution of the wave equation

$$\nabla \times \nabla \times \boldsymbol{E}(\boldsymbol{r}) - k^2 E(\boldsymbol{r}) = i\omega\mu_0\mu\boldsymbol{j}(\boldsymbol{r}), \tag{1.6}$$

where μ and μ_0 are the relative and free-space magnetic permeability respectively. Since the source is point-like, the solution can be expressed in the formalism of the Green function of the wave equation:

$$[\nabla \times \nabla \times -k^2]\boldsymbol{G}(\boldsymbol{r}, \boldsymbol{r_0}) = \boldsymbol{I}\,\delta(\boldsymbol{r} - \boldsymbol{r_0}). \tag{1.7}$$

If the solution of Equation (1.7) is known, the electric fields distribution can be computed as:

$$\boldsymbol{E}(\boldsymbol{r}) = \omega^2 \mu_0 \mu \boldsymbol{G}(\boldsymbol{r}, \boldsymbol{r_0}, \omega)\boldsymbol{p}, \tag{1.8}$$

from which applying the Pointing theorem the radiated energy power P can be obtained:

$$P = -\frac{1}{2}\int \mathrm{Re}\big[\boldsymbol{j}^*(\boldsymbol{r}) \cdot \boldsymbol{E}(\boldsymbol{r})\big] = \frac{\omega}{2}\mathrm{Im}\big[(\boldsymbol{p}^* \cdot \boldsymbol{E}(\boldsymbol{r_0})\big] = \frac{\mu_0 \omega^3 |\boldsymbol{p}|^2}{2}\mathrm{Im}\big[\hat{\boldsymbol{n}}_p \cdot \boldsymbol{G}(\boldsymbol{r_0}, \boldsymbol{r}_0, \omega)\hat{\boldsymbol{n}}_p\big] \tag{1.9}$$

where $\boldsymbol{G}(\boldsymbol{r}, \boldsymbol{r}', \omega)$ is the dyadic Green function and $\hat{n}_p$ is the unit vector in the direction of the dipole moment. In Equation (1.9) the Green function is evaluated at the location of the emitting system ($\boldsymbol{r} = \boldsymbol{r}' = \boldsymbol{r}_0$) and therefore describes the previously emitted electric fields arriving back at its origin.

1.1.3 Local density of states

It can be shown with a QED treatment of the electromagnetic fields that the decay rate is given by [20]

$$\Gamma = \frac{2\omega^2}{\hbar c^2}|\boldsymbol{p}|^2 \mathrm{Im}\big[\hat{\boldsymbol{n}}_p \cdot \boldsymbol{G}(\boldsymbol{r}_0, \boldsymbol{r}_0, \omega)\hat{\boldsymbol{n}}_p\big], \tag{1.10}$$

where we are now labelling $\boldsymbol{p}$ the the previously defined dipole moment operator $\hat{\boldsymbol{D}}_{ab}$. Equation (1.9) can be rewritten in the form of the Fermi's golden rule as:

$$\Gamma = \frac{2\pi}{\hbar}|\boldsymbol{p}|^2 \rho_p(\boldsymbol{r}, \omega) \tag{1.11}$$

isolating the interaction term proportional to $\boldsymbol{p}$ from the term solely depending on the electromagnetic states $\rho_p(\boldsymbol{r}, \omega)$ projected into the dipole direction

$$\rho_p(\boldsymbol{r}, \omega) = \frac{2\omega}{\pi c^2}\mathrm{Im}\big[\hat{\boldsymbol{n}}_p \cdot \boldsymbol{G}(\boldsymbol{r}_0, \boldsymbol{r}_0, \omega)\hat{\boldsymbol{n}}_p\big]. \tag{1.12}$$

It can also be proven [21] that this is linked to the spectral density of eigenmodes of the medium (when those are defined)

$$\rho(\boldsymbol{r},\omega)=\sum_n |\boldsymbol{e_n}(\boldsymbol{r})|^2\delta(\omega-\omega_n)=\frac{2\omega}{\pi c^2}\mathrm{Im}[\mathrm{Tr}\boldsymbol{G}(\boldsymbol{r}_0,\boldsymbol{r}_0,\omega)]. \tag{1.13}$$

Therefore Equations (1.13) and (1.12) define the local density of optical states (LDOS), and the partial LDOS restricted to a specific dipole orientation respectively.

The comparison of Equations (1.9) and (1.10) shows that there exists a relation between the radiation of the classical dipole and the spontaneous emission radiation from a dipolar emitter, namely

$$\frac{\Gamma}{\Gamma_0}=\frac{P}{P_0}, \tag{1.14}$$

where Γ and Γ_0 are the decay rates respectively in the environment and in free-space while P and P_0 are the correspondent emitted power by classical dipoles in the same conditions. The nature of the dipole is different but the interaction with electromagnetic modes is the same in both cases. This has few important consequences:

- We can indifferently consider the emission of a classical or quantum dipole, whenever only the optical properties of the environment are studied, which is typical in nano-optics, as the dipole moment of the emitter is not changed. However, the chemical properties of the environment can change the emitter properties (we consider this for instance when studying sensing by random lasing in Chapter 4). It is worth noting that this treatment is not valid also in the strong coupling regime, when the emitter and the environment cannot be considered as two separate systems any more [22]; nevertheless, this is not the case for the systems considered the present work.

- The LDOS is a well defined local quantity and thus it is suitable to compare theoretical calculation and experimental measurements; this comparison is particular robust as it relies on time-resolved measurements which are not affected by the collection efficiency or quenching of the emission, as long as even a small subset of the emitted photons can reach the detector. In other words lifetime measurements are a far-field probe from of the electronic states, and thus provide a well sub-wavelength resolution.

- The techniques employed in studying and solving the classical Maxwell equations can be used to compute the LDOS of a system. This can be

done for instance by means of Finite Difference Time Domain (FDTD) simulations.

1.2 Light emission in nanostructured materials

The emission of light from a dipole in an homogeneous environment can be easily calculated by solving Equation (1.7). The free-space radiation rate is found to be[22]

$$\Gamma_0 = \frac{\omega^3 n^3}{3\hbar c^3 \pi \epsilon \epsilon_0} |\boldsymbol{p}|^2,$$

and it is distributed in the far field with a typical omnidirectional "doughnut" shape oriented according to the dipole moment

$$P(\theta, \phi) \sim \cos^2(\theta) \tag{1.15}$$

for a dipole oriented in the zenith direction and θ is polar angle, as shown later in Figure 1.3. Any discontinuity of the refractive index of the optical landscape will modulate the light emission, and can provide access to the near-field components of the dipole emission. It was first shown in the seminal Drexhage's experiment [23] that a system as simple as a dielectric interface can affect the decay time. Figure 1.2 shows simulations (FDTD) of an electrical-dipole source ($\lambda = 532$ nm) placed at different positions in front of a dielectric interface with index of refraction $n_1 = 1.45$ (glass).

When the dipole is far from the interface the emission rate asymptotically approaches the bulk value $\Gamma = n\Gamma_0$, with a weak modulation due to the far-field interference with the light reflected by the interface. Instead, as the emitter moves closer to the interface near-field interactions get stronger and largely modulate the decay rates. For a dipole oriented parallel to interface, the interference between the radiation of the dipole and the induced charges inside the dielectric materials leads to large variation very close (< 50 nm) to the interface; this shows how controlling the evanescent components in the near-field is the key tool to engineer light behaviour.

Such near-field effects reflect in far-field accessible quantities as for example the angular radiation pattern. Figure 1.3 shows the calculated (FDTD) dipole emission pattern for a source in an homogeneous space. The pattern of the same dipole approaching a glass interface is also plotted. When the dipole is in close proximity to a dielectric interface the interference between the radiation of the dipole and

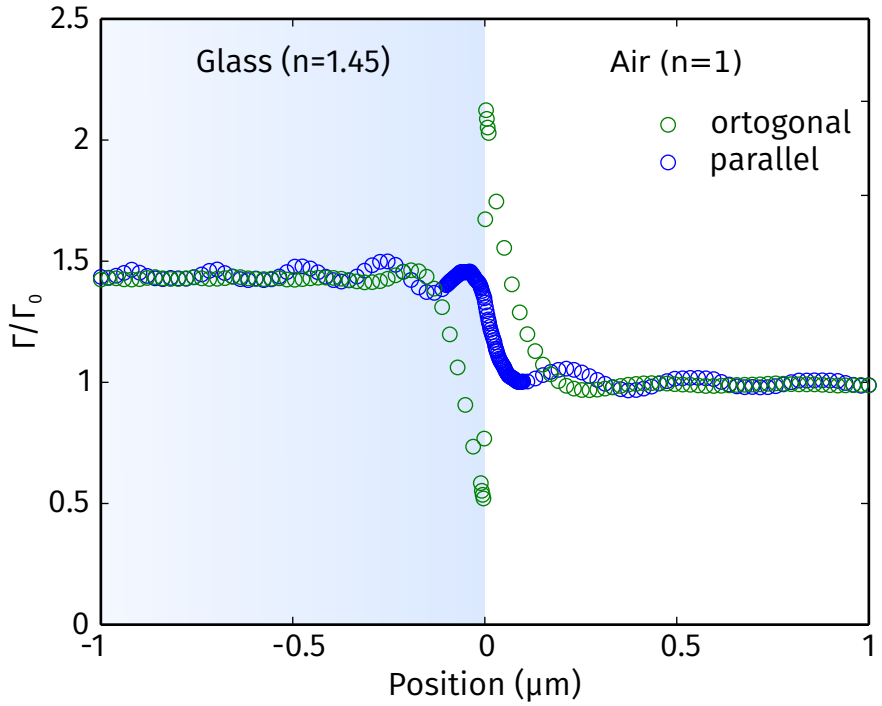

Figure 1.2: **The interface effect on lifetime**. Computed Purcell factor by means of FDTD simulations for a dipole source ($\lambda = 532$ nm) in front of a semi-infinite dielectric interface in the two orientations: dipole moment parallel to the interface (blue) and dipole moment orthogonal to the interface (green).

the induced charges inside the dielectric material reflected light strongly modifies this pattern: most of the light is emitted into the high-index material at the critical angle of total internal reflection $\theta_c = \arcsin\left(\frac{n_1}{n_2}\right)$. It is worth noting the importance of this effect as this situation describes the experimental conditions when usually the source is placed above a substrate.

The local optical modes effectively control the properties of the radiated light. Vice versa, the far-field light can be studied to obtain information on the optical modes accessible by emitter in its position, which are efficiently excited by the near-field and far-field dipole fields.

1.2.1 Plasmonic system and emission enhancement

Nanophotonic systems based on metallic structures with nano-sized features are particularly attractive as they can squeeze light into nanometre sized volumes. In fact, metallic structures sustain particular electromagnetic modes arising from the coupling between the electromagnetic waves and the collective oscillations of free electrons in noble metals called Plasmons [24]. These excitations manifest in the form of Surface Plasmons (SPs) at a flat metal-dielectric interface. SPs are

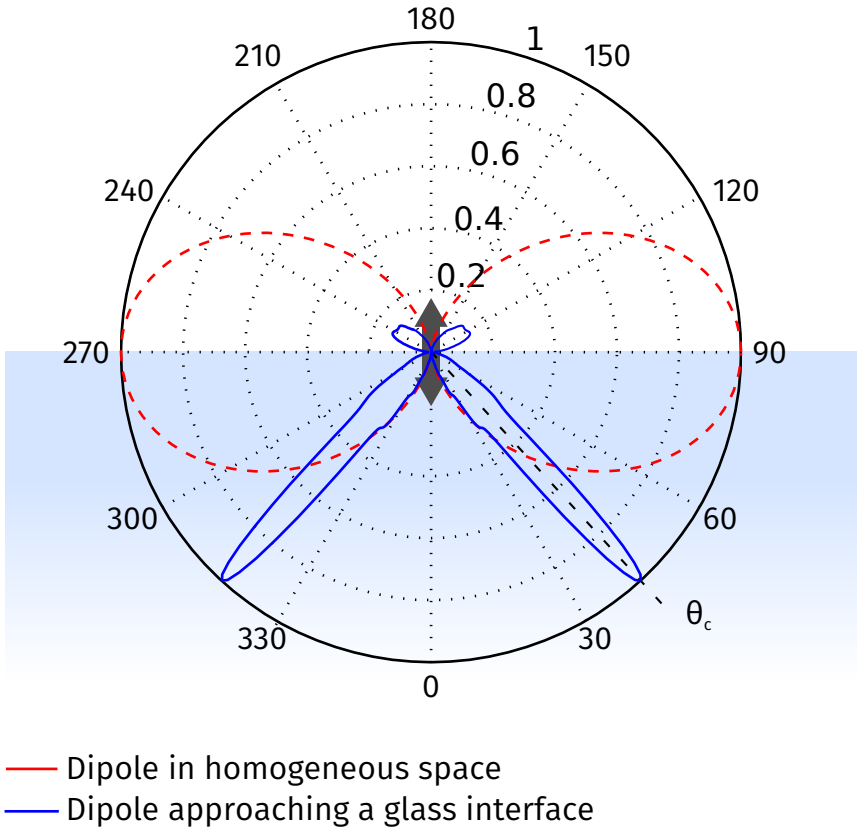

Figure 1.3: **Radiation pattern near an interface**. Power radiation pattern of a dipole source (FDTD calculations). Red dashed line: "doughnut" pattern of a dipole emitting in an homogeneous space. The blue line shows the radiation pattern of the same dipole approaching a glass interface (dielectric material, $n_2 = 1.51$) perpendicular to the dipole moment. θ_c is the critical angle of total internal reflection.

propagating waves bounded to the metal surface: the electromagnetic fields decay exponentially in the direction normal to the interface both in the dielectric and in the metal. This results in a stronger spatial localisation and field enhancement, yet, due to the absorption in the metal, SPs propagation length is finite, and complex geometries with refined fabrication techniques are required to overcome this limitations [25, 26].

The plasmonic response of a small ($\ll \lambda$) metal particle is similar to that of an optical electric dipole, therefore they can act as optical antennas. In analogy to microwave and radiowave counterparts, optical antennas are devices that improve the coupling between an object localised in their near-field and the radiation propagating in the far-field by impedance matching [27]. In nanometric metal particles the size and shape of the metal boundaries, as well as the particle composition, define a resonant frequency of the collective fluctuation of the electrical charges. This form of excitation is called Localised Surface Plasmons (LSP). At the res-

onant frequency, the electromagnetic waves can efficiently couple to the particle mode with a strong enhancement of the electromagnetic fields around these plasmonic antennas. If an emitter is placed in such electromagnetic hotspots this can result in an increase in its decay rate over one thousand times [28, 29]. The fluorescent enhancement due to the antenna is twofold:

1. Upon light excitation, the high intensity of the fields that build up around the antenna when in resonance efficiently promotes the molecule to the excited state, the absorption probability being proportional to the fields intensity.

2. More importantly, the molecule excites very efficiently the modes of the antenna as these electromagnetic-hotspots correspond to locations with a very large density of states. The antenna in turn is a classical dipole with a larger dipole-moment or multipolar components due to its larger size, and therefore emits efficiently in the far-field. Both emission rate and directionality [30, 31] can be designed for sources in the near field of the metal structure.

As in the case of SPs, the major drawback of metallic particles is the large optical absorption which is driving the search for alternative geometries and materials.

1.3 Towards complex networks

As we have seen in the previous sections, the connection between matter nanostructuring and the resulting optical properties can be done rigorously in all its details as long as one is able to consider all the microscopic aspects of the system under examination. When dealing with macroscopic systems this implies a nanometre fabrication accuracy over millimetres size, which is typically infeasible. As anticipated, the aim of this thesis is to focus on the study of complex systems, i.e. systems characterised by a large number of interacting components; their aggregate behaviour is often not derivable from the sum of the behaviour of the its individual constituents, either because due to the disordered character and long-range correlation it is not clear what interacts with what or because the importance of multiple interactions makes it difficult to treat the system numerically in all its details, for instance due to the limited calculation power.

When multiple elements are combined and coupled together, the collective response is defined from the interaction between the individual constituents. Scattering of light becomes one of the most relevant phenomena. The effect of multiple scattering on the emission of light has been studied in both dielectric and

plasmonic systems. For instance, disordered dielectric systems exhibit long tails LDOS statistics [32, 33, 34], while metallic structures combining multiple scattering and plasmonic response show large LDOS fluctuations depending on the correlation properties [35, 36, 37], as we will show in Chapter 3.

The interplay between disorder and correlation can result in peculiar optical effects, as in the case of hyperuniform structures [38, 39] showing the behaviour of photonic crystals in isotropic non-periodic structures. In these systems, a purely reductionist approach might fail or be not exhaustive. In such circumstances, describing the problem with a global approach can be more successful. For example, one possible framework to describe such systems is that of networks, a concept that pervades science and engineering [40], describing systems as diverse as food webs, power grids, and cellular metabolism [41].

1.3.1 Lasing in disordered systems

Beside fluorescence from independent emitters, when many sources are coupled in a photonic system newly collective phenomena can be investigated, among which lasing is one of the most important. Lasing is emission of light amplified by stimulated emission and is typically achieved by combining a gain-material, such as a molecular dye or semiconductor diode, with an optical cavity, required to confines light and resonantly enhances its interaction with matter and which defines the emission characteristics. When many emitters are combined in a multiple scattering medium, lasing may occur due to the interference between random paths inside the system. These random lasing systems were already theoretically discussed in the 1960s and first demonstrated in the 1990s [42] and has been thereafter widely investigated [43]. The mirror-less nature and structural simplicity of these lasing systems have attracted a lot of interest. Nowadays they have been studied in a vast variety of scattering systems ranging from semiconductor powder to biological tissue and biocompatible materials [43]. Random lasing originates from a complex out-of-equilibrium phenomenon with rich multimodes behaviour [44] and surprising statistical features [45] governed by the scattering properties of the system and the gain which couple, enhance and select specific system modes. Random lasing, which is the topic of Chapter 4, is an attractive phenomenon capable for instance of amplifying correlations in disordered systems.

*
**

In this thesis, we will consider three main aspects of light-matter interaction: the coupling of emitters to modes of interconnected structure; the emission enhancement by means of disordered plasmonic systems; collective phenomena in the form of lasing in disordered media. The study of single emitters, that is individually addressable sources emitting one photon at a time, offers a very fine spectroscopy tool, and is also a step heading towards the quantum world. We do this with an experimental approach based on the study of light emission of individual or localised fluorescent sources, as well as lasing dynamics, as discussed in the remaining part of this chapter.

1.4 Experimental methods

The experimental investigation is focused on the study of the lifetime and the angular emission pattern of fluorescent sources and is based on scanning confocal microscopy. This technique allows to achieve a diffraction-limited illumination and a high precision in the localisation of a light source. When combined with a high sensitivity single photon detection it is especially suitable for single-molecule studies. A commercial inverted microscope has been largely modified and adapted for maximum control and flexibility. A sketch of the setup is shown in Figure 1.4.

1.4.1 Confocal microscopy

In our configuration the light from different laser sources is injected into the microscope through a single-mode optical fibre, acting as a spatial filter and ensuring to achieve an homogeneous and stable beam profile. Light is then injected into the microscope and focuses to a diffraction limit spot with a high-numerical-aperture (NA) oil-immersion objective. The laser sources in use consist of both picosecond pulsed lasers (533 nm and 634 nm) and continuous wave lasers (448 nm and 633 nm).

The emitted light is collected through the same objective used for excitation. The Stoke spectral shift of the fluorescent emission allows to separate the emitted light from the excitation light by means of a dichroic beam splitter. Additional long-pass filters are employed to further remove any residual laser light more than 6 order of magnitude.

The emitted light is sent for detection to two different measurements setups, one based on avalanche photodiodes (APDs) and another based on a CCD camera and a spectrometer. An APD is a highly sensitive semiconductor electronic device

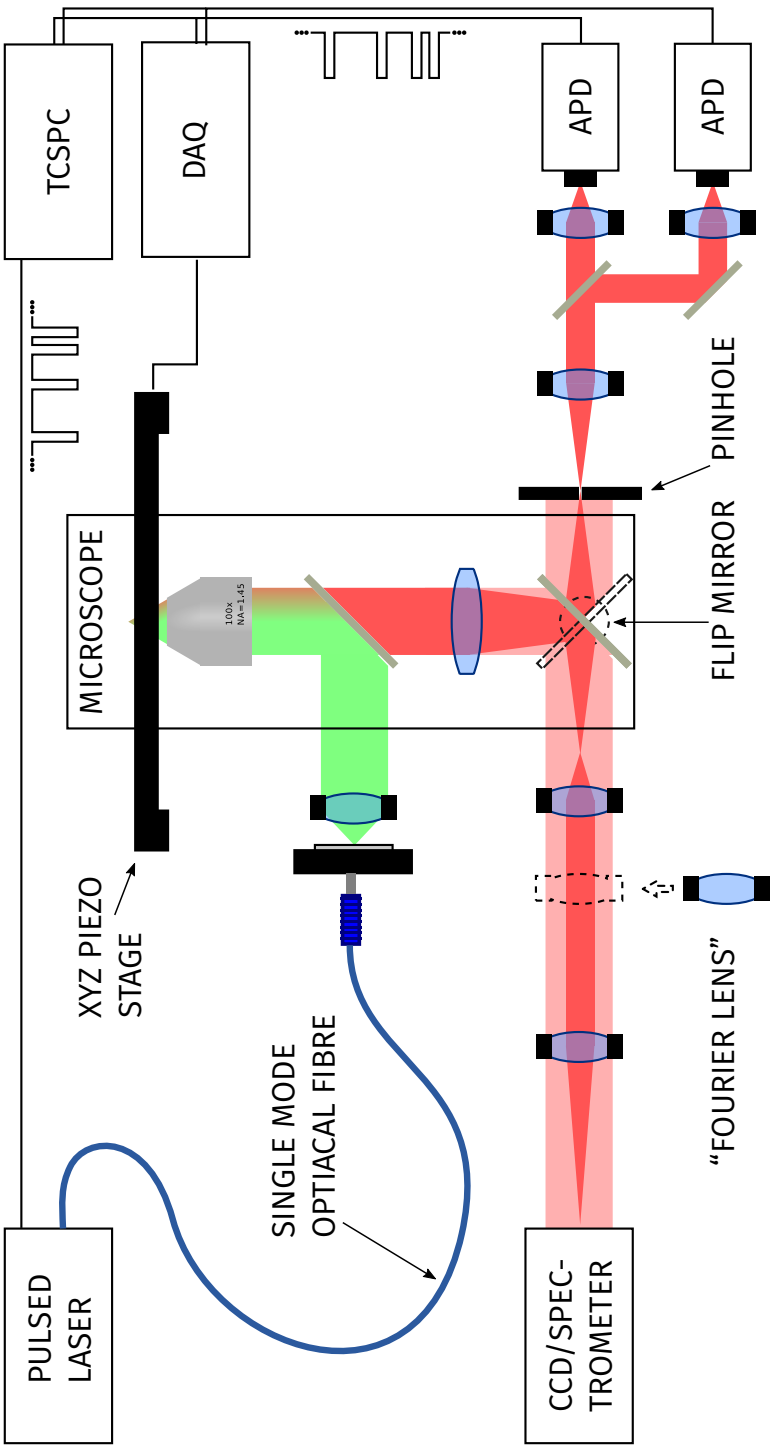

Figure 1.4: Sketch of the experimental setup. Laser light is injected into a confocal microscope on the sample placed on a piezoelectric stage. A flip mirror allows to collect the fluorescence light either on the CCD camera of a spectrometer or with an avalanche photodiode (APD). The APD signal is collected by a data acquisition interfaced with a PC that counts the emitted photons and by a time-correlated single photon counting system (TCSPC). The DAQ synchronizes the light collection and sample movements.

that exploits the photoelectric effect and avalanche multiplication of electrons to convert light to an electrical signal. It detects single photons with an high quantum efficiency ($\sim 70\%$) and timing resolution (400 ps).

In the confocal configuration (the right side in Figure 1.4) a pinhole is placed on the real plane of the microscope where the image of the sample is formed. The size of the pinhole is chosen to match the diameter of the focal spot in the image produced by the microscope. In this way light not originating from the optical axis will not pass through the pinhole and will be rejected increasing the resolution and contrast. This combined with the very low noise level of the used APD ($<$ 30 counts per second) allows to achieve a very high sensitivity and dynamic range suitable for single emitters studies.

A temporal trace of the emission from a single quantum-dot as recorded by the APD is reported in Figure 1.5. The plot shows the fluorescence intermittency or

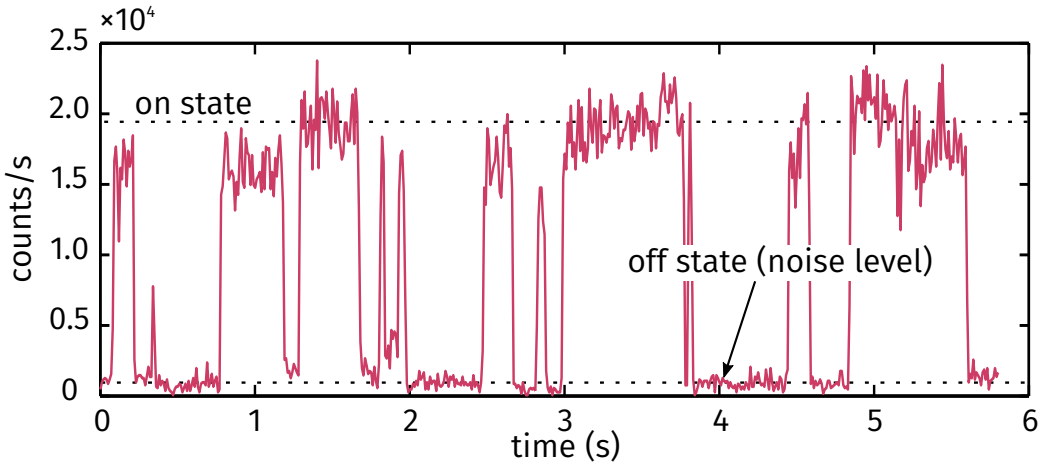

Figure 1.5: **Quantum dot blinking**. Fluorescent emission intermittency between on (bright) and off (dark) states typical of single emitters.

"blinking" phenomenon in which the QD switch randomly between on (bright) and off (dark) states under continuous excitation.

The APD is a single channel detector. In order to form a two-dimensional image of the sample has to be scanned point by point. This is achieve by means of piezoelectric stage that moves the sample while illumination and collection locations are kept fixed. The stage controls the positioning with nanometric resolution ($<$ 2 nm) in the xyz-axes at a moderately fast speed allowing a reliable raster scan up to few lines per second with a maximum scanning area of $200\,\mu\text{m} \times 200\,\mu\text{m} \times 200\,\mu\text{m}$. The photon collection is synchronised to the movement of the sample by means of a data acquisition system (DAQ) that counts the TTL pulses produced by the APD while controlling the piezo position. Dedicated software has been implemented in order to drive the DAQ, collect the data, and reconstruct the image of

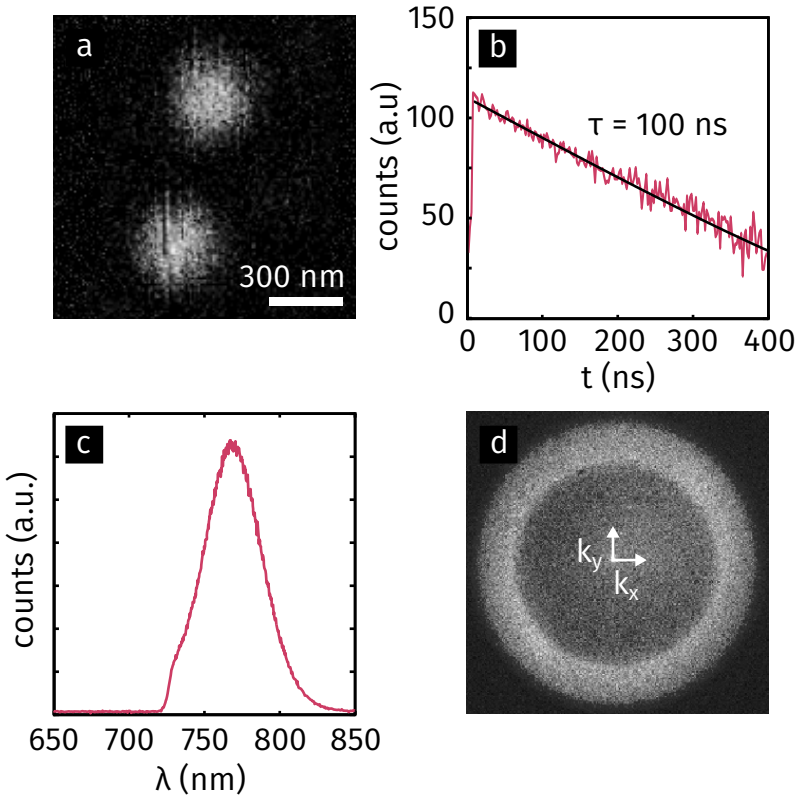

Figure 1.6: **Imaging quantum dots.** [a] APD scan of two quantum dots , [b] lifetime, [c] fluorescent spectrum and [d] angular emission pattern.

the sample, as shown in Figure 1.6a). Once the image of the sample is produced the points of interest can be localised with high accuracy. Each of these points can then be located and centred on the optical axis by means of the piezo to perform additional measurements (Figure 1.6b-d) as explained in the next paragraphs.

1.4.2 Time-correlated measurements

The train of pulses provided by the APD are recorded by a time-correleted single photon counting (TCSPC) unit, an electronic device that is able to measure the time of arrival of the photon with a very high temporal resolution (25 ps). The TCSPC unit compares the time of arrival of the pulse coming from the APD with a reference signal synchronised with the laser excitation pulse. In the optimal situation less than a photon is collected in each excitation cycle that has a typical repetition rate of 2–40 MHz. From the statistics of arrivals of the photons a lifetime measurement can be performed, as shown in Figure 1.6b for a quantum dot.

Correlated measurements between multiple detecting channels can also be performed. In particular, among correlations arising from the quantum nature of

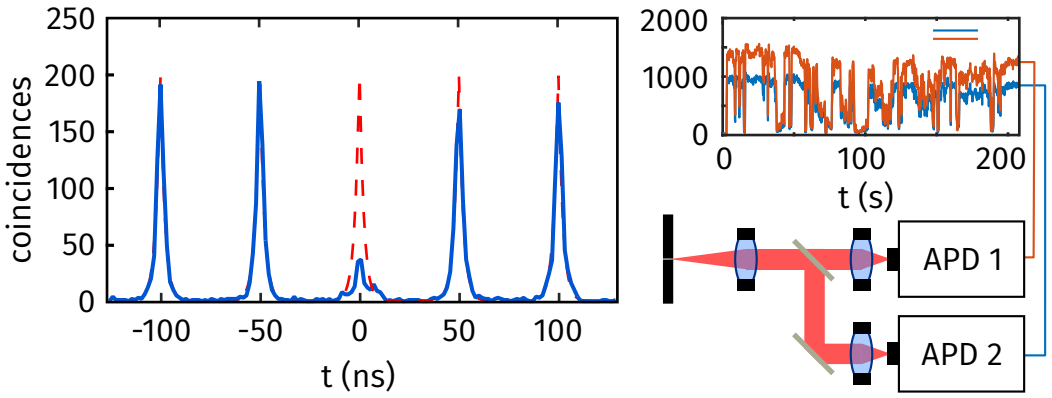

Figure 1.7: **Hanbury-Brown and Twiss interferometry**. The intensity correlation function g_2 showing the antibunching statistics is obtained from a molecule on a clean microscope cover slip is shown(when working at the single molecule level samples are never clean enough).

light, "antibunching" between the photons emitted by a source allow to characterize single photon sources [18] as shown in Figure 1.7. When recording the coincidences between two detectors in the Hanbury Brown and Twiss interferometer configuration, that is the probability of detecting two simultaneous photons when the signal is split between two detector as function of the delay between the detection Δt, a negative correlation at $\Delta t = 0$ manifests as a missing peak in the g_2 plot, corresponding to the fact that if a source cannot emit two photons at once the two apds cannot detect an event simultaneously.

1.4.3 Spectroscopy and angular emission pattern

The second detector consists of a low-noise high-sensitivity CCD camera connected to a spectrometer. Thanks to the ability to replace the grating with a mirror, the spectrometer is used both to measure spectra and as an imaging system. A system of two lenses is used to image the microscope real plane on the spectrometer slit for standard spectroscopy. The fluorescence spectrum of a QD obtained in this way is shown in Figure 1.6b. imaging capabilities are exploited in particular to measure angular emission patterns by measuring the Fourier space.

One of the remarkable properties of a converging lens is his ability to perform two-dimensional Fourier transforms [46]. The intensity of the light in the back focal plane is proportional to the Fourier transform of the front focal plane:

$$I_2(x_2, y_2) \propto \hat{I}_1(k_{x_1}, k_{y_1})$$

In our setup, the addition of a lens in the optical path allows to image the back-

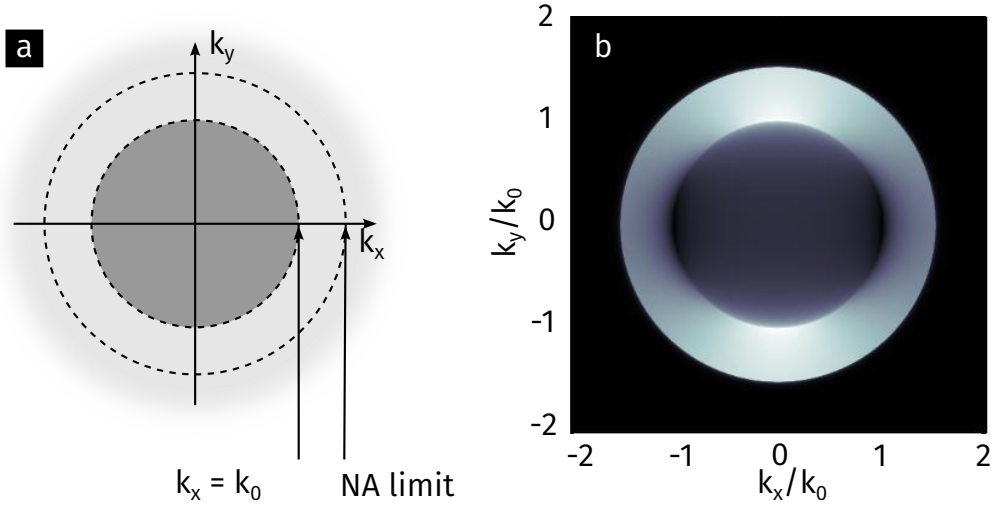

Figure 1.8: **Angular emission *k*-space patterns**. [a] Typical k-space diagram: the inner circle defines the cone of light. The accessible k-space is limited by the numerical aperture of the optical system: any k—vector outside of the outer dashed line cannot be measured. [b] Computed k-space for a dipole source, $\boldsymbol{d} = d \cdot \hat{x}$, above a dielectric ($n = 1.51$) interface (Courtesy of Dr. Francisco Rodríguez-Fortuño).

focal plane of the first lens. A typical k-space diagram is shown in Figure 1.8a. The inner circle defines the light-cone: all k-vectors in the darker area represent propagating waves and are usually accessible with far-field techniques. The accessible k-space can be increased employing high-NA objectives. Any k-vector outside of the outer circle cannot be measured. The Fourier relation $\Delta x \Delta k \geq 1/4$ links the extension in the momentum space to the spatial extension of the mode under examination. An analysis of the Fourier space is thus in principle able to give insights on the localisation properties of the optical modes that are emitting light. The limit of this analysis is the limited size of the accessible momentum space as shown in Figure 1.8a. The study of the Fourier space can also be used to identify the dipolar emission pattern of small objects and antennas or the higher orders of the multipolar expansions of more complex objects. In Figure 1.8b the computed k-space of a dipole oriented along the x-direction and positioned in close proximity to a dielectric interface is shown. The picture shows that light is emitted mostly beyond the cone of light ($k \geq k_0$) with the maximum at the critical angle in the direction perpendicular to the dipole moment (y in the figure), while there is no emission at the critical angle along the dipole axis. The angular emission pattern of a quantum dot is shown in Figure 1.6d. Most of the light is collected between the critical angle defined by the inner circle and the NA limit. Because of the symmetry of the dot and consequent level degeneracy quantum

dots do not have a defined dipole moment, therefore light is emitted without a preferred direction.

An example of Fourier spectroscopy allowing to identify the different nature of the emitting source is given by Figure 1.9. A Eu^{3+}:Y_2O_3 thin film (Courtesy of

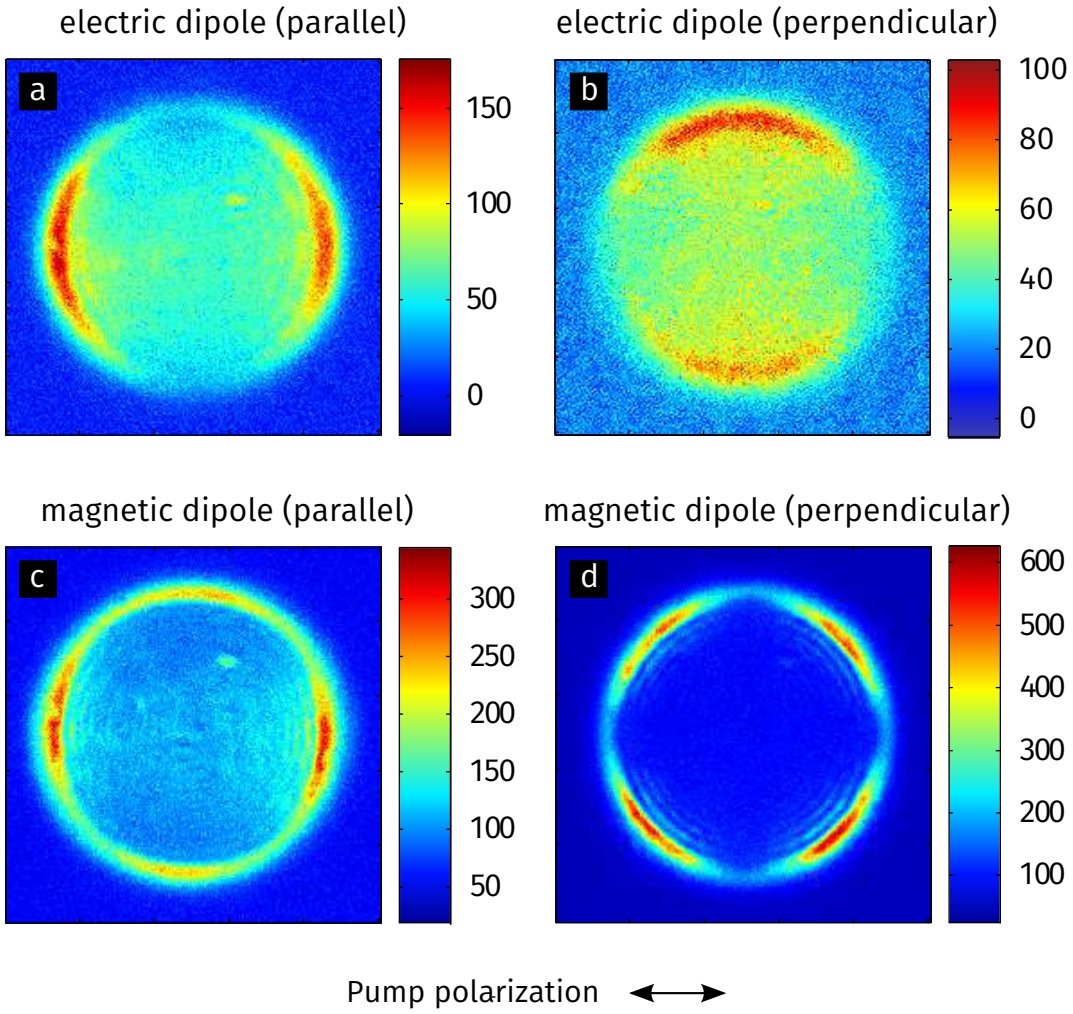

Figure 1.9: Electric and magnetic dipoles radiation patterns. Angular emission pattern of a Eu^{3+}:Y_2O_3 thin film (Courtesy of Prof. Rashid Zia) [a] [b] $\lambda <$ 600 nm (electric transition); [c] [d] $\lambda > 600$ nm (magnetic transition). Recording the light emitted with polarization parallel or orthogonal to the pump (along the horizontal plane of the figure) allows to discern between a predominately electric or magnetic dipole transition.

Prof. Rashid Zia) is illuminated with a 532 nm light polarised along the horizontal plane of the figure. This crystal manifests both an electric and magnetic dipole transition, the former being prevalent at wavelengths lower than 600 nm, the latter at wavelengths above 600 nm [19]. By considering these two region of the spectrum and analysing the two different emission polarisations – parallel and perpendicular to the pump one – it is possible to distinguish two different emission

patterns, as in Reference [19]. The electric transition pattern is similar in the two cases although the pump defines a preferred emission direction. On the other hand, the magnetic transition shows different patterns with a more prominent quadrupolar component.

1.4.4 Random lasing measurements

Random lasing measurements are performed with a configuration similar to that described in Figure 1.4. The main difference is the requirement of an excitation with a large pulse energy ($\sim\mu$J–mJ per pulse, depending on the excitation area), which is required to achieve population inversion and therefore lasing. Random lasing samples are pumped with the second harmonic of a Nd:YAG Q-switched pulsed laser, at 532 nm wavelength, 10 Hz repetition rate and 6 ns pulse duration. Moreover, due to the non-linear character of the lasing response in particular around the threshold transition, large fluctuations and pulse to pulse variabilities are often observed. Therefore, measurements are usually performed with a single pulses. The detection software registers pulse energy and the sample emission spectra in backscattering for each pulse in a large energy range of 5–6 orders of magnitude achieved by a combination of neutral density filters for the coarse control and a half-waveplate and a polariser for the fine control. This allows to extract the relevant lasing parameters such as the lasing threshold from the spectral evolution of the emission as shown in Figure 1.10a. The lasing transition is recognised from the narrowing of the emission spectrum (FWHM) and the increase of the emitted peak intensity (Figure 1.10b).

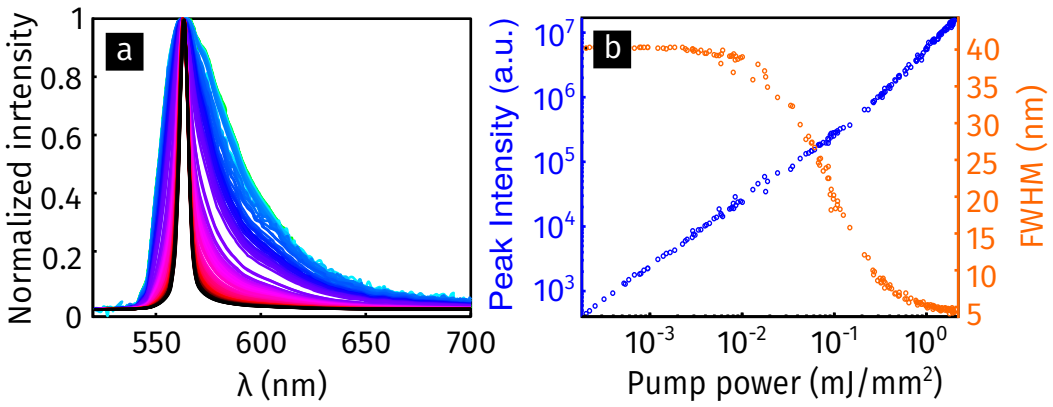

Figure 1.10: Lasing threshold in a rhodamine-6G and TiO_2random laser. a Normalised spectra at different pump power. b FWHM narrowing (orange points) and peak intensity at the lasing wavelength (blue points) at increasing pump power powers.

1.5 Outline

This rest of this thesis is structured as follows:

- In *Chapter 2* a single emitter coupled to a nanofibre waveguide is investigated, highlighting the modal coupling of the light sources to the guided modes. This is a basic building block for the realisation of more complex interconnected architectures.
- In *Chapter 3*, plasmonic systems undergoing an electrical percolation transition are investigated in self-assembled metallic films and lithographic systems of nanoantennas, as well as the role of global network-like behaviours and collective long-range effects which emerge over disorder as a complementary scheme to the near-field engineering for the control and enhancement of light emission.
- *Chapter 4* concerns fully disordered dielectric systems: diffusive media with gain are investigated in the framework of random lasing, modelling the effect of resonant scattering systems, as well as possible applications for sensing.
- The *Conclusive chapter* summarises the results of this thesis with a critical review of the work and considerations on the future extensions and expected developments.

2 Modal coupling of individual quantum dots to a nanofibre by momentum spectroscopy

A system composed of free-standing sub-wavelength polymer nanofibres with embedded individual colloidal quantum dots is investigated, demonstrating a platform providing large coupling and long range propagation of single photons. The nanofibres are fabricated by electro-spinning of a polymer solution with emitters dissolved prior to fabrication, thus the emitters are embedded in the nanofibre core, which allows for high coupling efficiency without complicated fabrication techniques. The system operates at room temperature in non-resonant conditions, therefore it provides broadband operation. We show how momentum spectroscopy of individually addressed emitters allows to measure the coupling and disentangle the different modal contributions. We report broadband coupling to the fundamental mode up to $\beta = 31 \pm 3\%$ and a propagation length of $\xi = 95 \pm 5\,\mu$m, in robust agreement with theoretical calculations.

2.1 Introduction

In this chapter, we consider the coupling of a localized source to the propagating optical modes of a nanostructure. Channelling of light emitted from a source into low-losses propagating modes, such as those of a waveguide, is a fundamental step towards the realisation of more complex architectures, as this would provide the basic building block allowing remote addressing of the emitter and eventually allowing the interaction between distant emitters. Various coupling schemes have been proposed and realised; nevertheless, a miniaturised and scalable single-photon system operating at room temperature, showing higher coupling efficiency to an individual mode and with a broadband response, is still sought after.

When considering an individual fluorescence source in this context, an important figure of merit is the *coupling efficiency* β, describing the strength of the coupling to the optical modes of interest over the other emission channels which are typically considered losses. This can be defined as the ratio between the intensity of light couple to the propagating modes I_{prop} and the total light emitted I_{tot}:

$$\beta = \frac{I_{prop}}{I_{tot}}. \tag{2.1}$$

Other figures of merit to take into account are the propagation length ξ defining the decay length of the propagating intensity I ($I(x) = I_0 \mathrm{e}^{-x/\xi}$) due to the losses in the system and describing the ability to deliver the emitted photon over long distances as well as the ability to trap it into the system, and the enhancement of the decay rate (Purcell factor)

$$P = \frac{\Gamma}{\Gamma_0}, \tag{2.2}$$

describing the emission enhancement potentially raising the photon generation efficiency.

The choice of the material and fabrication techniques strongly affects the waveguide operation and performance. Plasmonic waveguides with strongly confined surface plasmon-polariton modes have attracted a lot of attention as they can provide very high coupling efficiency [47] and small footprint, but with limited practical applications due to the strong ohmic losses in the metal, which can only be partially reduced with sophisticated geometries [25, 26]. Hybrid architectures have also been proposed [48].

Instead, dielectric nanofibres can combine a large near-field coupling with relatively low propagation losses, realising a simple interface between light emitters and propagating modes, through which energy transfer between distant sources

can be enhanced [49, 50, 51, 52].

Experimental realisations include the coupling of epitaxial quantum dots to photonic crystal waveguides in cryogenic conditions [53] with remarkable efficiency close to 100%, although this is limited to narrow-band resonances. Nevertheless, the difficulty of positioning the emitter into a specific location and the incompatibility of lithographic techniques with common organic and inorganic sources have pushed the interest towards simplified coupling schemes. One notable possibility is the employment of pulled fibres, which allow the coupling of an external emitter located nearby the fibre thanks to the evanescent fields. Evanescent coupling of colloidal quantum dots to nearby pulled silica fibres has been obtained at room temperature with efficiency up to ~ 30%, approaching experimentally [54, 55] the theoretical limit imposed by evanescence coupling [56]. The coupling can be enhanced by working in geometries exhibiting a deep subwavelength confinement [57].

An efficient albeit harder to realise scheme, where the emitter is placed inside a dielectric nanofibre has been pioneered for hollow fibres filled with a dense atomic gas [58]. More recently, coupling of up to 18% has been achieved for single molecules at cryogenic temperatures inside a pulled glass capillary [59], which is remarkable given the low index of refraction contrast, and provides increased robustness to the environmental conditions, the source being protected into the fibre core. This demonstrates the potential of this coupling scheme; in the next section, the characteristics of a dielectric cylindrical waveguide is investigated numerically.

2.2 Modal coupling calculations

A step-index waveguide can be obtained considering a cylindrical fibre composed of a material of index of refraction n standing in air ($n_{air} = 1$). A fibre sustains propagating modes, characterized by a k component in the propagation direction in between the light line in air $\omega = c_0 k$ and in the material $\omega = c_0 k/n$. For circular-symmetric step-index fibres the modes are designated as LP_{nm} according to their symmetry. A fundamental mode (with polarization degeneracy) LP_{01} (which is both TE and TM and thus also designated HE_{11}) is always available. Its dispersion relation is shown in red in Figure 2.1. Higher order modes LP_{nm}have a cut-off for small diameters. The single mode condition is given by:

$$\frac{D}{\lambda} < \frac{2.4048..}{\pi\sqrt{n^2 - n_{air}^2}},$$

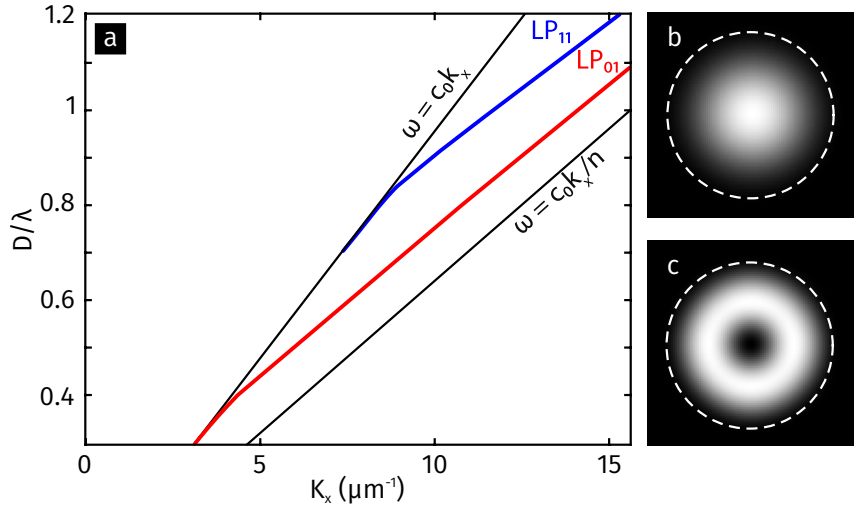

Figure 2.1: Step index fibre modes. a The dispersion relation of the propagating modes of a step index lies between the light line in air ($\omega = c_0 k_x$) and the light line in the material ($\omega = c_0 k_x / n$). a The fundamental (LP_{01}) and b first order (LP_{11}) transverse spatial profiles (fields intensities).

corresponding to $\frac{D}{\lambda} \simeq 0.7$ for $n = 1.5$ in Figure 2.1. All propagating modes lie between the air and core light lines.

The total coupling efficiency can be obtained by FDTD simulations calculating the light intensity transmitted through a monitor crossing the free-standing nanofibre 4 μm away from a electrical dipole source, which is located in the centre of the nanofibre. Figure 2.2 shows the calculated total coupling β in the case of a dipole oriented transversally and longitudinally to the fibre, and located at the centre of the fibre core of diameter. For common index of refraction ($n = 1.5 \div 2.5$), the coupling is expected to be between 50% and 70%, which can be further increased approaching 90% at $n = 4$ for single-modes fibres and transverse dipole orientation (Figure 2.2a, blue). Figure 2.2 shows also that the dependence on the dipole orientation, while for reason of symmetry the longitudinal dipole cannot couple to the fundamental mode (Figure 2.2a, orange). Large fibre diameters allow coupling to the other modes, and both dipole orientations have similar coupling efficiencies (Figure 2.2b)

When more then one mode is available, the modal coupling efficiencies $\beta^{(n)}$, *i.e.* the coupling to the n-th mode, can be defined considering only light emitted into the the specific mode $I^{(n)}_{prop}$:

$$\beta^{(n)} = \frac{I^{(n)}_{prop}}{I_{tot}}.$$

The modal coupling efficiency can numerically be obtained by mode projection

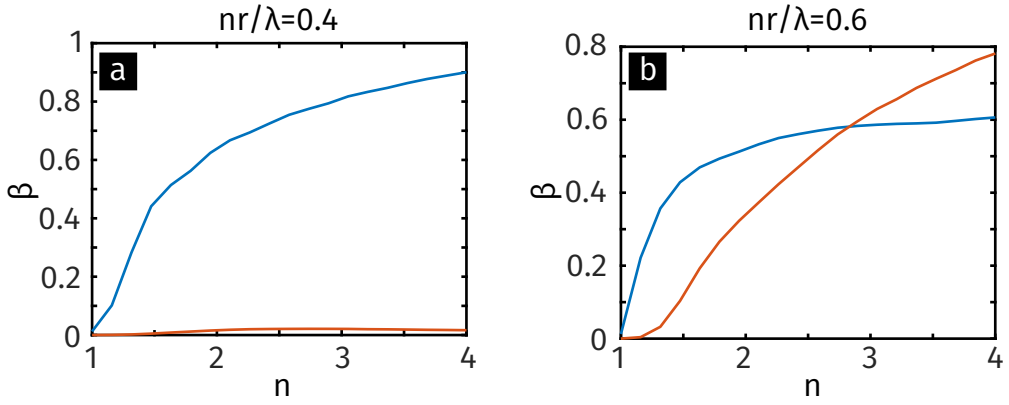

Figure 2.2: Coupling efficiency β as a function of the refractive index. The total coupling efficiency β for a transverse (blue) and longitudinal (orange) dipole for a fixed nr/λ ratio is calculated by FDTD simulations. [a] The fibre is single mode ($D/\lambda \simeq 0.55$ at $n = 1.5$) and only the transverse couple with β growing quickly to 50% up to n=2 and subsequently a slower approach of 90% for n=4. [b] In multimode regime ($D/\lambda \simeq 0.8$ at $n = 1.5$) both dipole orientations couple with growing values at higher n.

of the same total intensity onto the independently calculated nanofibres modes. In Figure 2.3 both the total coupling (β) and modal to a specific fibre modes (β_{01}, β_{11}), the first excited one LP_{11}, are plotted, for a fibre of refractive index $n = 1.49$.

While the total coupling β remains roughly constant for all diameters (red dashed line in Figure 2.3), the theoretical coupling β_{01} to the fundamental mode (red line in Figure 2.3) reaches its maximum value of $\beta_{01} = 53\%$ at $D/\lambda = 0.55$, and and then quickly drops to zero for larger diameters due to the emergence of the other modes, indicating that selective coupling to the fundamental mode is best achieved for sub-wavelength nanofibres. Figure 2.3 also highlights the selective coupling depending on the source orientation, due to the different fields profile of the different modes.

2.3 Electrospun polymer nanofibres

Given the analysis in the previous section, in order to achieve maximum coupling and efficient long-range transport, we require an architecture characterized by large contrast in the refractive index, which can be achieved with a free-standing geometry, sub-wavelength diameter and a quantum emitter is positioned at the core of fibre. This hybrid nanofibre-emitter system is sketched in Figure 2.4.

The nanofibres are fabricated by electrospinning a polymethylmetacrylate PMMA solution doped with CdSeTe colloidal quantum dots (Invitrogen QD800, emit-

ting at 790 nm). Unlike electron-beam or focussed ion-beam lithography, the electro-spinning process preserves the integrity of embedded organic and inorganic light emitters [60]. By measuring the emission spectrum of the quantum dots, we checked that the solvent, polymer matrix and organic salt do not affect the photoluminescence properties of the embedded emitters. Doped fibres are deposited either on a glass substrate or on a TEM grid producing free-standing nanostructures with length of tens to hundreds of micrometres long with isolated quantum dots. The nanofibre morphology was investigated by SEM and atomic force microscopy. The fibre diameters were in the range of 200-1200 nm, with a surface roughness (root-mean-square, RMS) of the order of few nm, and an almost circular cross section (Aspect ratio$\simeq$ 0.9–1).

Given the refractive index of PMMA (n=1.49), we expect a theoretical maximum coupling of $\beta_{01} = 53\%$, as shown before in Figure 2.3.

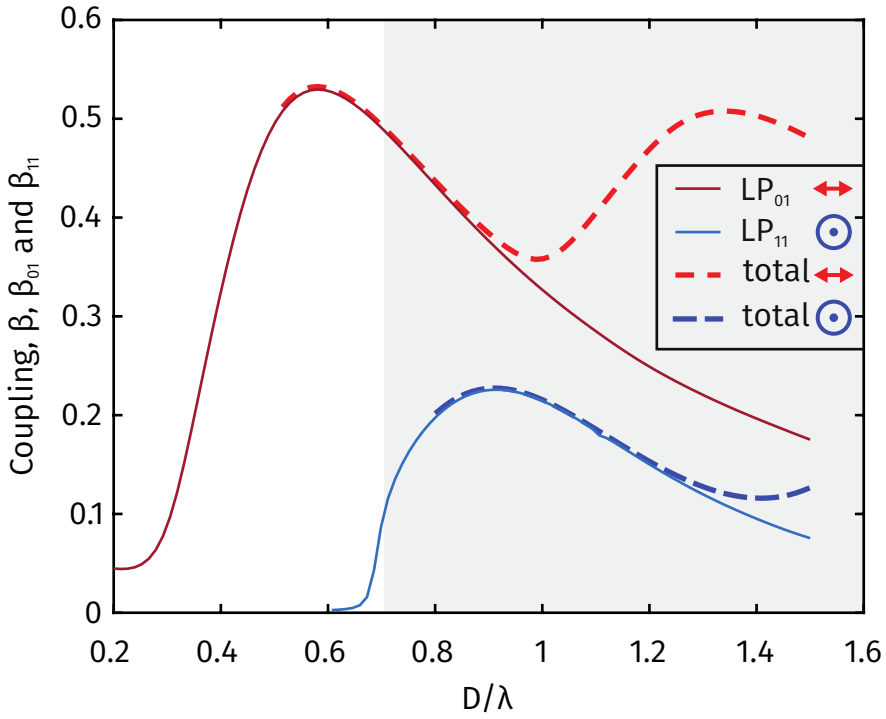

Figure 2.3: Coupling of the quantum dot to the nanofibre. Total (β) and modal (β_{01}) coupling is obtained by FDTD simulations (see Methods). While the total coupling (dashed lines) β remains constant for larger diameters, the coupling to the fundamental mode β_{01} (solid red line) and to the first mode (solid blue line) quickly drops for $D \geq \lambda$ due to the emergence of the other modes.

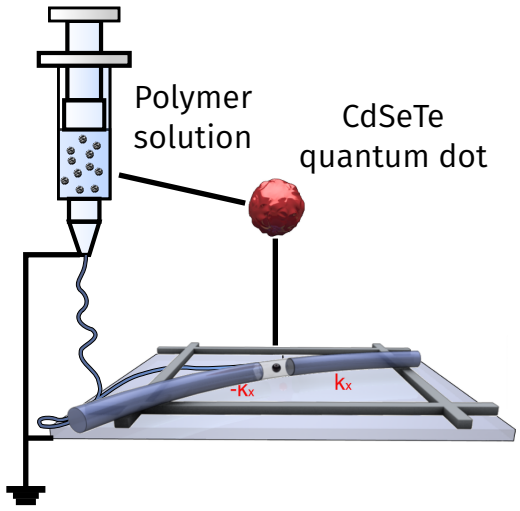

Figure 2.4: **Nanofibre fabrication**. Colloidal quantum dots are embedded into the PMMA solution from which nanofibres are obtained by electrospinning. The nanofibre is deposited on a TEM grid to obtain a free-standing design.

2.4 Single photon emission

A scanning electron microscopy (SEM) image of a typical free-standing nanofibre is shown in Figure 2.5a. When illuminated with a red laser, the emitters can be located via wide-field fluorescence imaging, as in Figure 2.5b.

The emission dynamics is studied by confocal microscopy and time correlated single-photon counting TCSPC (TimeHarp 260, PicoQuant) with an overall temporal resolution of ~100–200 ps. To prove single photon emissions we perform Hanbury-Brown and Twiss interferometry (Figure 2.6a) under CW excitation (12 μW, 633 nm) through an air objective (NA = 0.95). The light emitted was col-

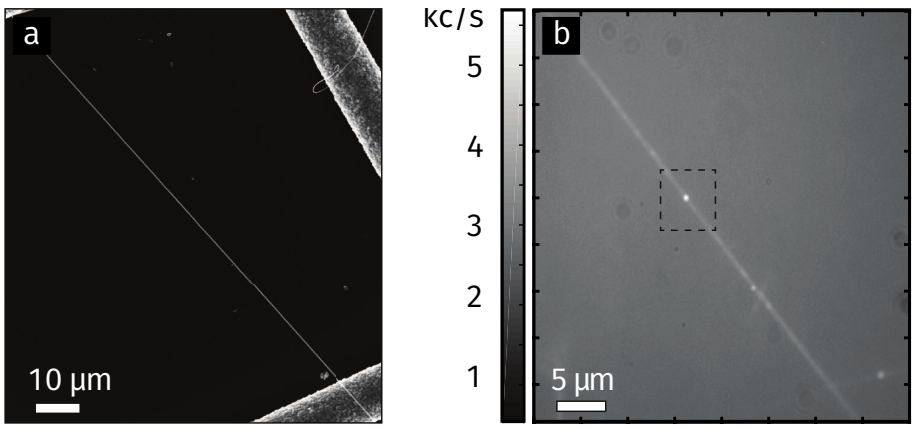

Figure 2.5: **Individual emitter in free-standing nanofibre.** a SEM picture of a free-standing nanofibre. b Wide-field fluorescence image of a similar nanofibre highlighting the presence of isolated quantum dots (dashed square)

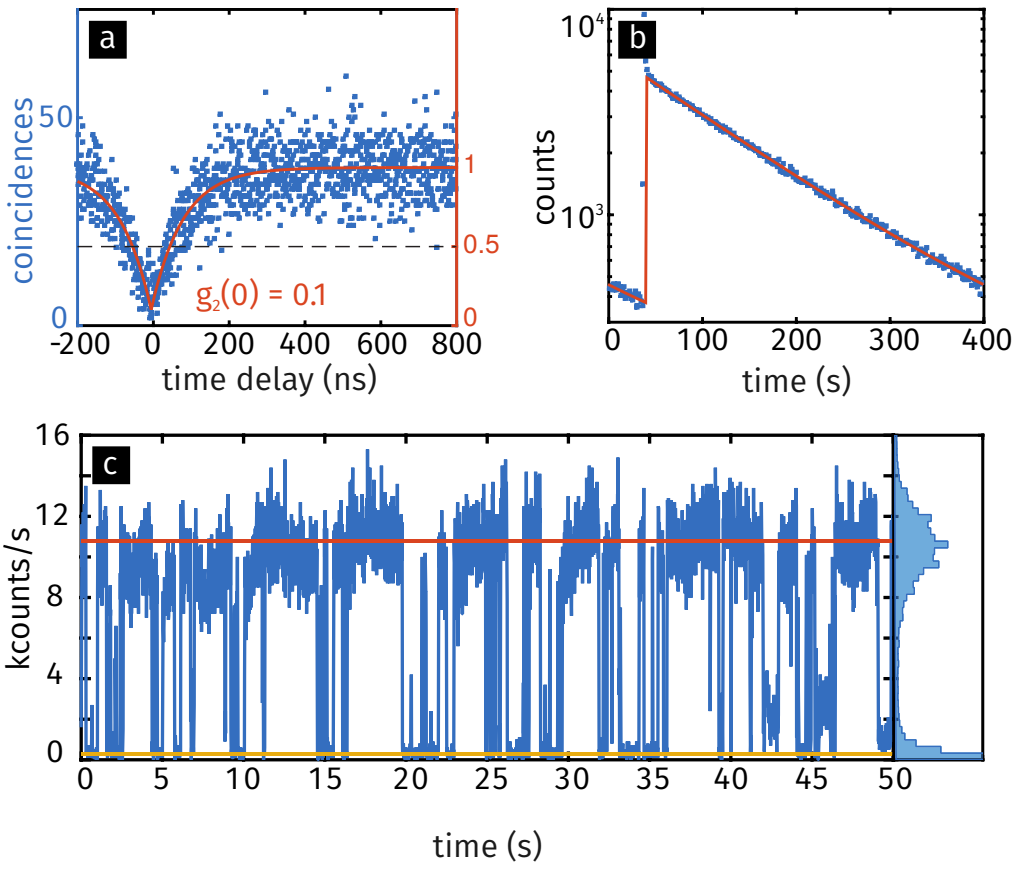

Figure 2.6: Addressing a single quantum dot coupled to a nanofibre. a The discrete nature of the photons emitted by the single quantum dot is proven by the second order correlation function, obtained via continuous-wave laser excitation (12 μW, 633 nm) which leads to $g_2(0) = 0.1 \pm 0.03$ when fitted with $g_2(t) = A(1-1/N \cdot \exp(|t|/\tau'))$. b The fluorescence dynamics of the same quantum dot under picosecond excitation (1.5 μW, 2.5 MHz, 634 nm) is fitted with a single exponential decay leading to an excited state lifetime $\tau = 137 \pm 0.1$ ns. c The time trace of the photons emitted by the quantum dot shows a blinking behaviour with on- (~10.5 kcounts/s) and off- (~0.3 kcounts/s) states as highlighted in the histogram.

lected by the same objective and directed to two avalanche photodiodes (APD) in start-stop configuration, obtaining the intensity correlation function $g_2(t)$. By fitting with

$$g_2(t) = A[1-(1/N)exp(|t|/\tau')], \tag{2.3}$$

we obtain the typical antibunching behaviour with $g_2(0) = 0.1 \pm 0.03$ (and $\tau' = 84 \pm 3$ ns) which confirms single-photon emission.

The excited state lifetime for the quantum dot is measured under picosecond pulsed excitation (100 ps, 634 nm, 2.5 MHz repetition rate, average power 1.5 μW) In the specific case shown in Figure 2.6b, a single exponential fit gives $\tau = 137 \pm 0.1$ ns. The difference between τ and τ' can be explained via an incoherent

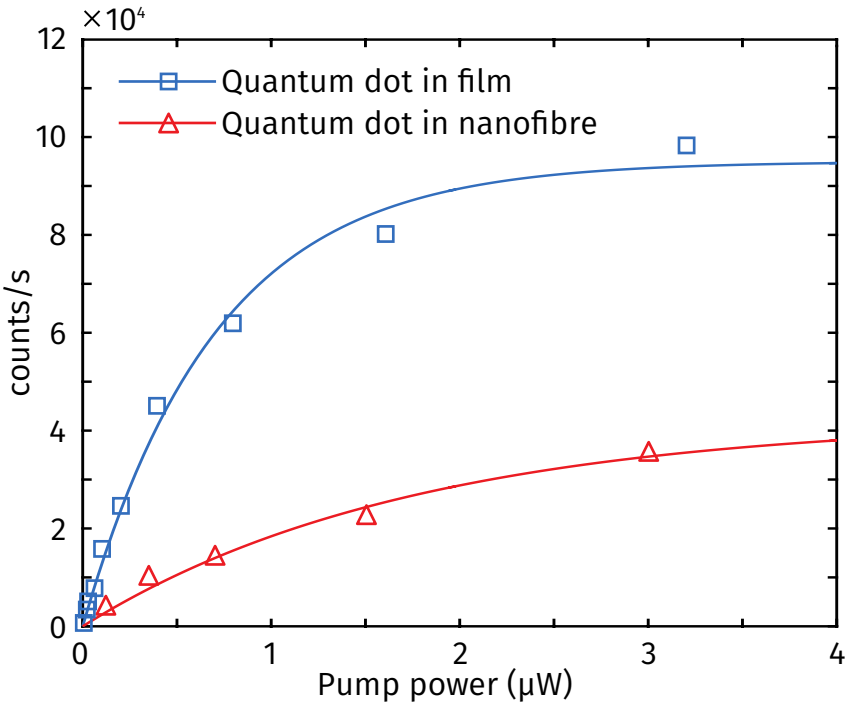

Figure 2.7: Emission saturation. Intensity emitted by a single quantum dot embedded in a nanofibre and in a reference film as a function of the illumination intensity. The repetition rate of our pulsed laser is set to 2.5 MHz. The quantum dot reaches saturation values of 35 and 95 kphotons/s respectively at around 0.5 μW (2.5 MHz, 532 nm). The red line is a fit to the data using a two level saturation model[62].

repumping term R, with $\tau' = (1/\tau + R)^{-1}$, as shown in Refs. [61, 47]. Light collected from the nanofibre-coupled quantum dots under CW excitation (12 μW, 633 nm) has a typical blinking behaviour and an average photon flux of ~10 kcounts/s, with an off state of ~300 counts/s (Figure 2.6c).

We study the emission intensity and stability stability at different pump intensities. In Figure 2.7 we compare the recorded intensities (in the on-state) for a quantum dot in an homogenous polymer film and for a quantum dot in a nanofibre for a pulsed excitation (2.5 MHz, 532 nm, pulse width $\tau_p = 100$ ps). The saturation intensity is in both cases a of 0.5 μW in a diffraction-limited illumination area (*i.e.* 0.8 W/cm^2). The solid lines are fits obtaind using the saturation curve of a two-level system

$$S = S_\infty (I/I_s)(1 + I/I_s) - 1[1 - \exp[-(1 + I/I_s)\tau_p/\tau_f)], \tag{2.4}$$

where I and I_s are respectively the excitation and the saturation intensities, and τ_f the decay time of the quantum dots. From the fit we obtain a saturation count rate $S_\infty = 95$ kHz and $I_s = 6.5$ KWcm^{-2}, and $S_\infty = 42$ kHz and $I_s = 6.1$ KWcm^{-2}

respectively. The lower count rate at saturation is due to the reduced collection efficiency of our microscope when the emission is coupled to the nanofibre, which we have estimated to be ~2–3% for polymer films and 1.45 NA oil immersion objective and ~1–2% for free-standing fibres and 0.95 NA air objective. At saturation the quantum dot emits one photon per excitation pulse, *i.e.* 2.5 Mphotons/s, given our laser repetition rate of 2.5 MHz; in reality this value is reduced by the less than unitary quantum efficiency (~0.8) and by the time the quantum dot is in the off-state (~ 30% on-state due to blinking) to a value that we estimate to be around 0.5 Mphotons/s.

2.5 Purcell enhancement

Light sources placed inside a sub-wavelength nanofibre suffer from suppressed emission rates due to a smaller than unity Purcell factor at the high-low index (PMMA-air) interface coming from the reduced local density of optical states [23]. We measured the decay rate Γ distribution of individual quantum dots inside free-standing nanofibres, as shown in Figure 2.6d, and compared them to a reference PMMA film. The lifetime traces were fitted with both a single exponential and a lognormal model, and the one providing the highest accuracy was retained. While both systems show a large Γ distribution with a full width at half maximum around ~70%, when the emitters are inside the free-standing nanofibre the average decay rate decreases from 12×10^{-3} ns^{-1} to 9×10^{-3} ns $^{-1}$ (Figure 2.8a). Assuming that the quantum dots are randomly oriented in the nanofibre, the data agrees well with the theoretical predictions that we obtained through the finite difference time domain (FDTD) method, plotted in Figure 2.8b and 2.8c, which are obtained by calculating the intensity emitted by a dipolar source in different position inside the nanofibre normalised to the emission in the bulk material. Figure 2.8b and 2.8c show the LDOS maps normalized to the bulk material for two dipolar orientations inside the PMMA sub-wavelength nanofibre. The Purcell factor is close to unity (in the range 0.8 to 1) in the case of a longitudinal dipole (Figure 2.8b) and conversely, it is reduced to around 0.5 for a transverse dipole (Figure 2.8c).

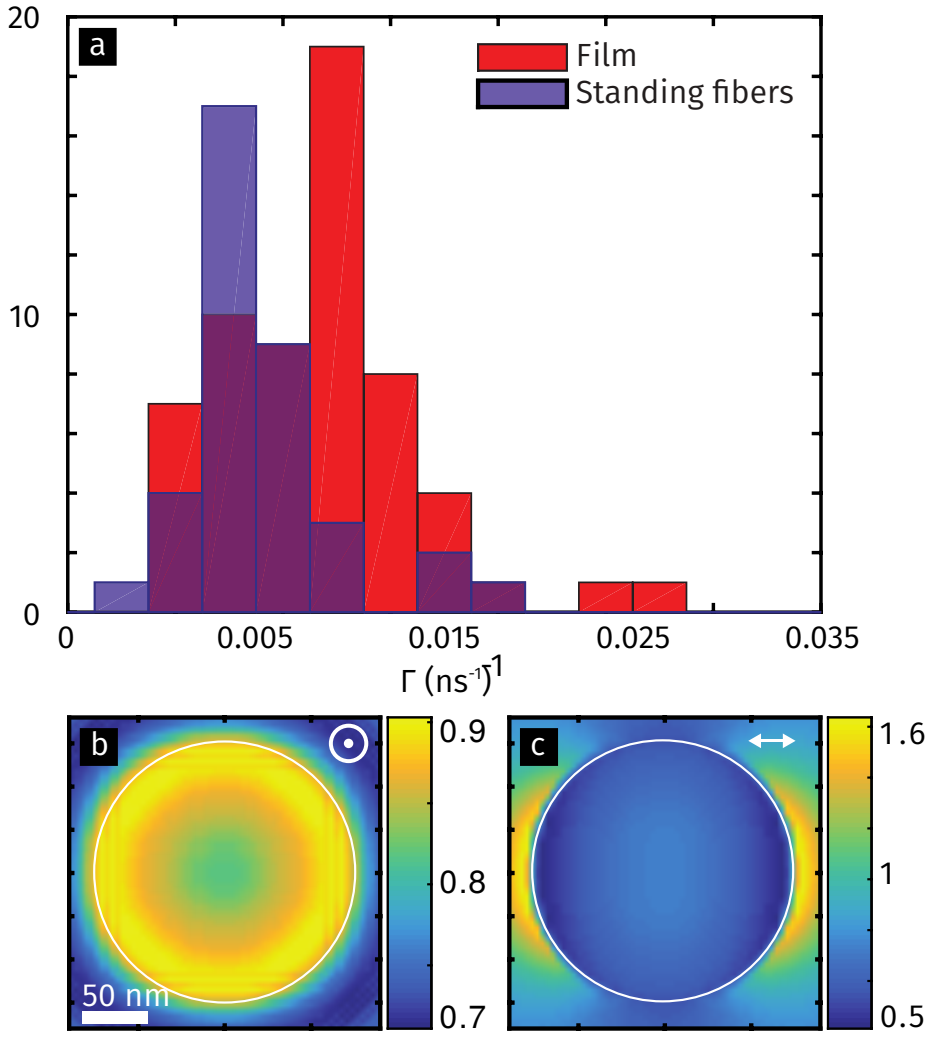

Figure 2.8: Purcell effect for the coupled emitters. [a] Decay rates distributions measured from the quantum dots in the standing fibres (blue) and in a PMMA film used here as a reference. The shift of the decay rate distribution towards smaller values, from an average of 12×10^{-3} ns^{-1} to 9×10^{-3} ns^{-1}, is compatible with the predicted values. [b] Calculated LDOS maps for a dipole longitudinal and [c] transverse to the fibre with 300 nm diameter (D) at different transverse positions. For $D < \lambda$the LDOS is almost uniform inside the nanofibre with values in the range of 0.45 to 1 depending on the dipole orientations. This is related to the presence of the interface that gets polarised by the dipole either in phase (longitudinal) or out-of-phase (transverse).

2.6 Photon transport through the nanofibre

Transport through the nanofibre can be confirmed qualitatively by studying a nanofibre lying on glass when purposely cut by a razor blade as shown in Figure 2.9. Here we present two wide-field emission maps with the excitation located at the quantum dot position (Figure 2.9a) and at the nanofibre cleaved tip (Figure 2.9b). The excitation laser is marked by the red circle. In both cases, the wide field image clearly shows the transport of light through the nanofibre. A cross section along the nanofibre is shown in Figure 2.9c and 2.9d, respectively, which allows quantification of the relative intensity of the light collected at the cleaved

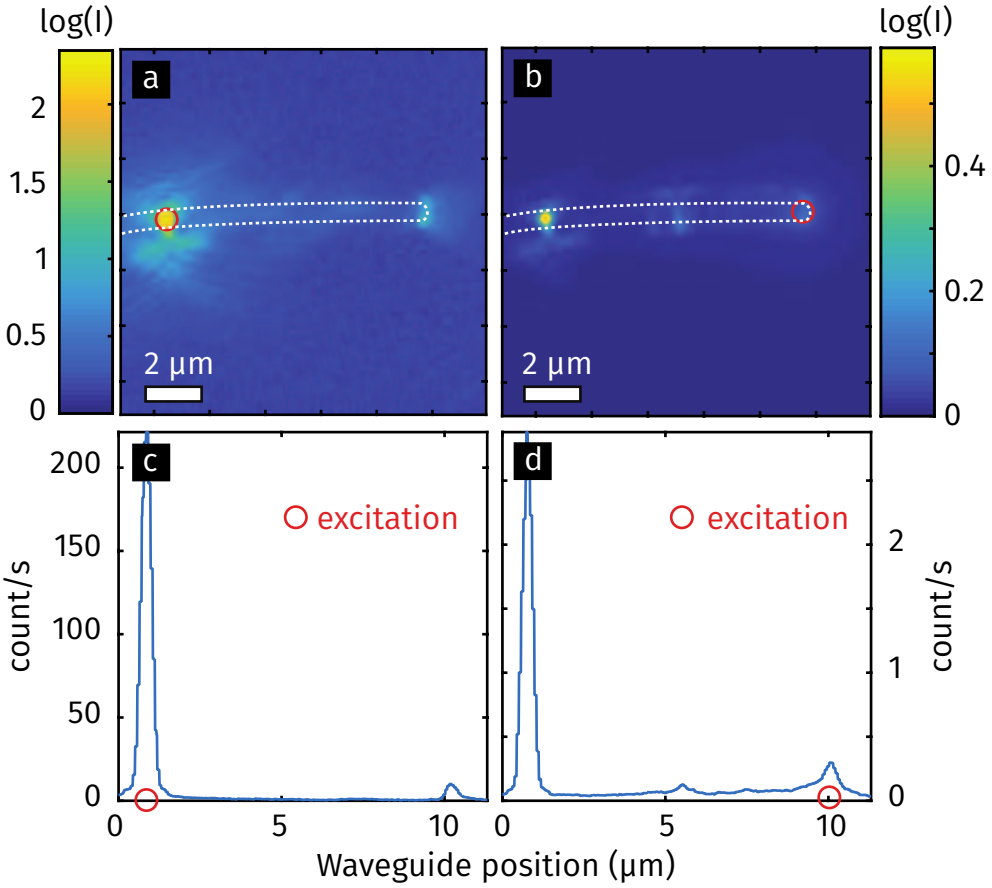

Figure 2.9: Remote addressing of individual emitters. Wide-field fluorescence images of an intentionally cut nanofibre lying on a glass substrate. [a] The exciting laser is focussed on a quantum dot. [b] The laser is moved to the nanofibre tip end as marked by the red circle. The corresponding line-plots along the nanofibre are shown below: [c] when exciting the quantum dot the bright spot at the nanofibre tip, which is ~ 10 µm away, indicates efficient light transport with a relative intensity of 12%. [d] Instead, when illuminating the exposed nanofibre tip, the laser light couples well to the nanofibres and is able to excite the distant quantum dot.

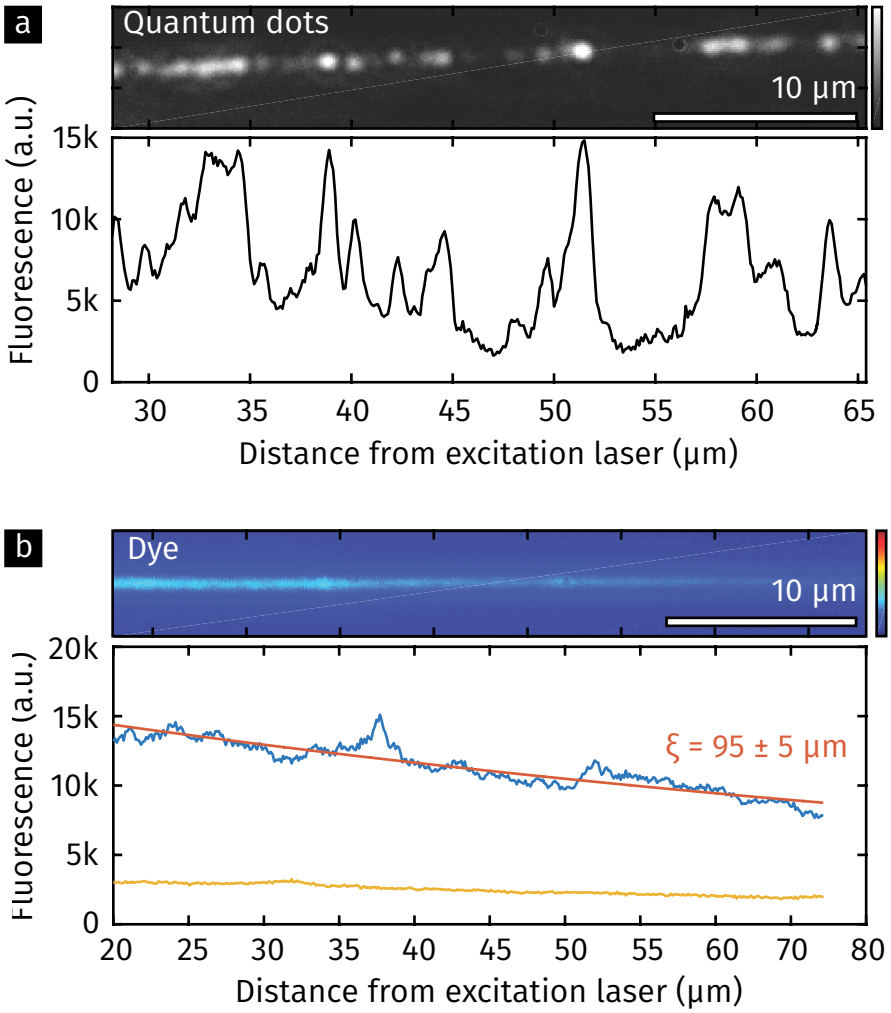

Figure 2.10: **Light transport through the nanofibre**. a A nanofibre with an intentional high-density of quantum dots which are remotely excited (the excitation position is outside the field of view and is transported through the nanofibre). b The transport length is measured by exciting a nanofibre filled with an IR laser dye (IR-140) emitting at around 800 nm. The excitation is 20 μm outside the field of view. The fluorescence intensity recorded along the fibre is fitted (orange curve) after subtracting the background (shown in yellow), obtaining a propagation length of $95 \pm 5 \mu m$, which is an underestimation of the actual propagation length in absence of the dye absorption.

tip, which is 12% of the intensity collected directly at the quantum dot location and leads to a qualitative estimation of the coupling $\beta = 24\%$, assuming a similar collection efficiency at both positions. These large values indicate that the nanofibre has a broadband response, capable of efficiently channelling the light emitted by the quantum dot in a bandwidth of more than ~ 100 nm.

To study the transport properties of the free-standing systems we consider an nanofibre intentionally doped with many quantum dots; their fluorescence at lo-

cation distant from the illumination spot is a direct evidence of transport of the exciting laser light through the nanofibre, as shown in Figure 2.10a which reports quantum dots excited as far as 60 μm from the laser spot. The granularity of the quantum dot doping impedes a quantitative estimation of the propagation length which can be obtained by recording how the fluorescence intensity leaks from a nanofibres doped with an IR dye (IR-140) which is shown in Figure 2.10b. By fitting with an exponential model ($I(x) = I_0 \exp(-x/\xi)$) the leaked light we obtain a propagation length of $\xi = 95 \pm 5 \mu m$. This is a conservative estimation as the measured propagation length is a combination of the nanofibre scattering and the dye re-absorption. Theoretically, we expect a propagation length of 100–1000 μm, as calculated by including Rayleigh scattering [63] from the nanofibre surface roughness (few nm) as measured by atomic force microscopy.

2.7 Coupling measurement from momentum spectroscopy

Whenever direct access to the coupled light is not available, probing the coupling factor requires indirect estimations, such as those drawn from the lifetime variations of on- and off-coupling [53], or from the collected scattered light [55, 57]. We have seen in Section 2.5 that in our system the emission rate is not enhanced but rather weakly reduced. Although counter-intuitive at first, this it is due to the fact that the presence of a fibre not only provides an additional decay channel but also modulates the previously available ones. Instead, momentum spectroscopy of the emitted light directly accesses the coupling of the emitter to the nanofibre modes and allows us to calculate the modal coupling in an original way, without measuring the light transported by the nanofibre. We apply Fourier patterns analysis which is emerging as a reliable quantitative tool to probe otherwise inaccessible information about the emitter [19] and its emission directionality [31]. We measure the light emitted in momentum space by recording the angular patterns of the radiation emerging from individual quantum dot inside a nanofibre lying on glass imaging the back-focal plane into a CCD camera. The excitation and collection was achieved through an oil immersion objective (100×, NA=1.45). Index matching allows access to large angles, up to the numerical aperture of our objective, which encompasses the wave-vectors of the guided modes beyond the air light-line. We collect Fourier patterns as shown in Figure 2.11a and 2.11b for two nanofibres: a thin one, in the single mode regime ($D/\lambda = 0.5$, Figure 2.11a) and a thick one, in the multimode regime ($D/\lambda = 0.9$, Figure 2.11b). These emission

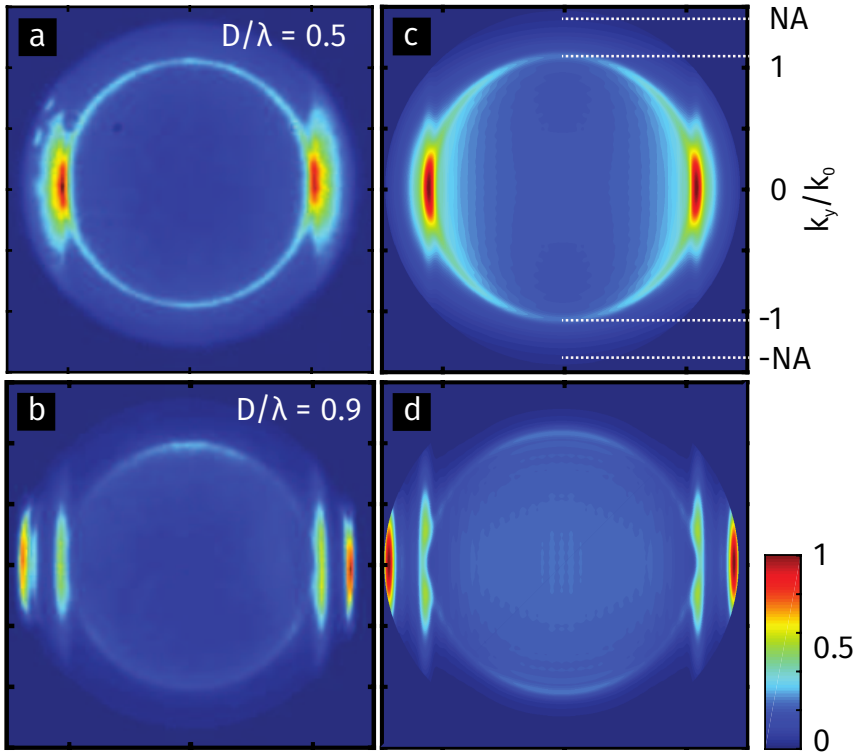

Figure 2.11: Angular pattern of quantum dots coupled to the nanofibres. a and b, Experimental angular patterns and, c and d, the corresponding theoretical calculations (FDTD) of the radiation emitted from a quantum dot in nanofibres on glass of different diameter for $D/\lambda = 0.5$ (upper plots) and for $D/\lambda = 0.9$ (lower plots).

patterns are clearly different from those obtained from an isolated quantum dot (See Figure 1.6d). Each pair of momenta lobes (positive and negative k_x) beyond the air light-line ($|k_x| > 1$), elongated in a direction orthogonal to the nanofibre, are the k-vector distribution of the distinct nanofibre modes. This is a clear experimental signature of the individual coupling of the quantum dot to each of the nanofibre modes which is in very good agreement with the calculated Fourier patterns shown in Figure 2.11c and 2.11d.

In Figure 2.12 the mode dispersion structure is reconstructed from the calculated angular pattern of a dipolar source in the centre of a nanofibre. The angular patterns are obtained by means of far field projections of the electro-magnetic fields in a plane 300 nm outside the nanofibre inside the substrate of a nanofibre laying on glass. Calculations with and without the glass substrate show that the low-refractive index interface below the nanofibre only weakly affects the modal dispersion, inducing only a spectral broadening due to the increased losses into the glass. The intensity map indicates the coupling strength of a longitudinal

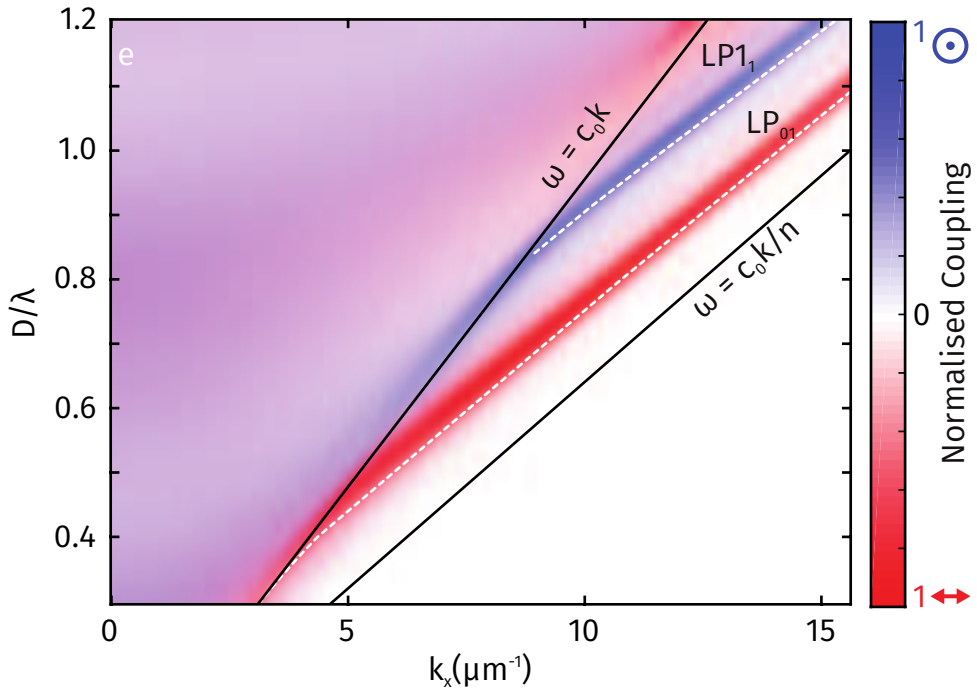

Figure 2.12: Momentum spectroscopy analysis. Theoretical calculations of the coupling of a dipole to the modes of the nanofibre obtained from the angular emission patterns of a longitudinal (blue) and transverse (red) dipole located at the centre of the nanofibre, normalized to the maximum coupling. Inside the air light-cone, the light corresponds to uncoupled emission and is therefore similar for both dipolar orientations. Instead, the emission for k-vectors beyond the air light line can couple to the nanofibre modes (high intensity red and blue bands). The emission maxima correspond to the dispersion of the two nanofibre modes. The analytical dispersion relation of the first two modes of the nanofibre in air (LP_{01} and LP_{11}) are plotted as white dotted lines.

(blue) and transverse (red) dipole to the nanofibre, normalised to unity, which is the maximal value in the plot. The guided modes are visible as two lines that stem from the air light-line $\omega = c_0 k_x$ growing to larger k-vectors up to the polymer light-line $\omega = c_0 k_x / n$. Due to the different spatial symmetry of the modes, the transverse (red) dipole couples almost exclusively to the fundamental mode LP_{01}, and the longitudinal (blue) to the second higher mode LP_{11}. Instead, the light emitted inside the light cone in air ($\omega > c_0 k_x$) corresponds to uncoupled radiation, emitted into free-space modes. We confirm this selective coupling and the nature of the modes by superimposing the analytical solution (dashed white lines) of the dispersion relations of the modes for a free-standing nanofibre [64]. The analytical solution matches the maxima of the coupling of the two dipole-orientations which confirms that the strength of the momenta peak is a direct measure of the coupling of the emitter to a specific wave-vector, *i.e.* to a specific

nanofibre mode.

Therefore, from the ratio of the coupled and uncoupled light the total coupling constant β as well as the coupling to the fundamental mode β_{01} can be estimated. From the recorded the angular emission patterns $I(k_x, k_y)$ we calculated the intensity distribution

$$I(k_x) = \sum_{k_y} I(k_x, k_y), \tag{2.5}$$

where k_x is the component of $\boldsymbol{k}$ along the nanofibre axis. We estimated the nanofibre diameter D by comparing the position of the peaks in the experimental Fourier patterns with the theoretical modal dispersion. As the nanofibre modes are only marginally affected by the glass interface, the light emitted in the k-regions beyond the light-cone in air corresponds to guided modes ($|k_x| > 1$), and the light inside the light-cone in air to the uncoupled modes. For multimodal fibres, owing to the modes' orthogonality in k-space, different modes have different wave-vectors for the same energy; this allows to assess the individual coupling to these modes by measuring the relative strength of the Fourier peaks. In this way, the coupling to the fundamental mode β_{01} can be separated from the total coupling β to all the waveguide modes. The coupling efficiency β is obtained as the ratio between the light emitted into the guided modes region ($|k_x| > 1$) and the total emitted light:

$$\beta = I(|k_x| > 1)/I, \tag{2.6}$$

while β_{01} is the ratio between the intensity of the k-vector corresponding to the mode LP_{01} and the total emitted light. This can be generalised for all other higher-energy modes.

The accuracy of this estimation can be confirmed by Finite Difference Time Domain (FDTD) calculations (Figure 2.13). The coupling to a nanofibre lying on glass calculated by far-field projections of the light emitted towards the substrate is compared to the value obtained by mode projection of the light transmitted in a free-standing nanofibre (as in Figure 2.3). The agreement between the values of β obtained from the two methods of momentum spectroscopy and direct modal coupling is within 10% for both dipole orientations, for the considered diameter range $D = 300 - 1000$ nm. The discrepancy is explained due to the variable transmissivity of different k-components to the far field. For small diameters, the overestimation is also explained in terms of light emitted in the upper direction and not collected by the objective. In the real experiment, the collection is limited by the objective NA and response, which for large k-vectors further lowers the apparent coupling.

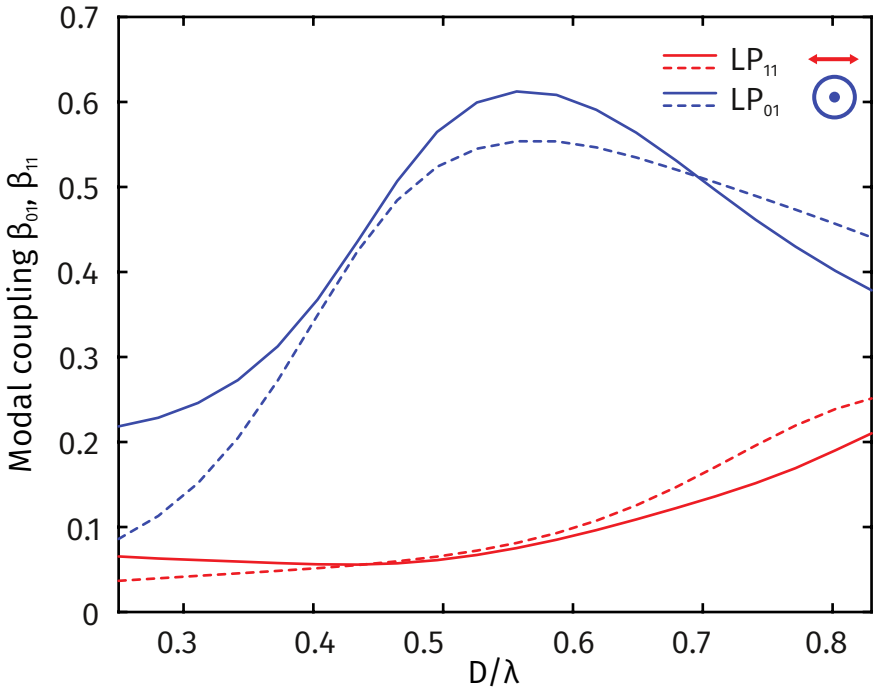

Figure 2.13: Coupling estimation from momentum spectroscopy. FDTD calculation of the coupling obtained from the momentum spectroscopy analysis (solid lines) of a nanofibre lying on glass compared to the direct probing of the transmission of a standing nanofibre (dashed line) for a longitudinally-oriented dipole (blue lines) and a transversally-oriented dipole (red lines). The comparison shows that the momentum spectroscopy analysis overestimates β by a maximum of 10% for the diameter under examination.

We obtain the coupling values from the experimental angular patterns according to Equation (2.6) as shown in Figure (2.14), where the lines represent the theoretical predictions and the points indicate the experimental data. The measured coupling values (green bars in Figure 3) are in the range $\beta_{01} = 21 \pm 2\%$–$31 \pm 3\%$ for single mode nanofibres, and $\beta_{01} = 5 \pm 1\%$ for multimode nanofibres, where also the coupling to the second higher mode LP_{11} increases (orange bars in Figure 2.14). The errors come from the uncertainty in the position of the peaks in the k-space: an uncertainty is attributed to both D and β due to the uncertainty in the k-space calibration that we quantify as 0.05. As expected, the experimental values are lower than the theoretical prediction for a transverse or longitudinal dipole, as in the experiments the quantum dot's dipole moment is randomly oriented. These findings confirm that large single mode coupling can only be achieved with sub-wavelength nanofibres.

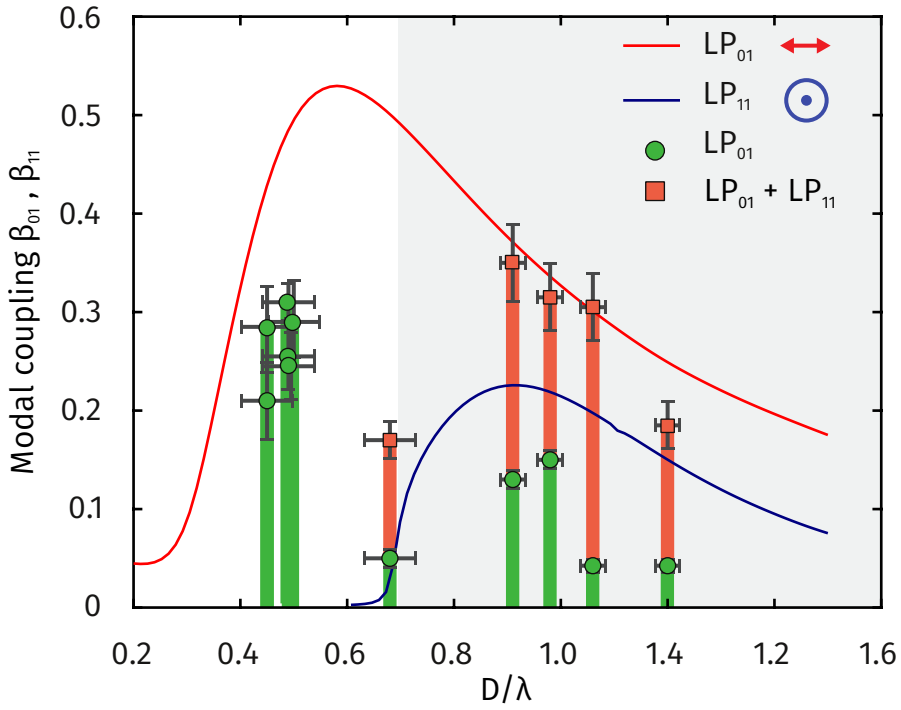

Figure 2.14: Modal coupling of the quantum dot to the nanofibre. Experimental values obtained by momentum spectroscopy. The coupling to the fundamental mode LP_{01} are plotted as circular green points (and green bar). In the multimode region (grey shaded area), coupling to the second higher mode LP_{11} are shown by an orange bar and the total coupling is marked by orange squares. The experimental values are compared to the theoretical calculations for the two dipole-orientations (red line for transverse, and blue line for longitudinal). The error bars originate from the uncertainty in the position of the peaks in the k-space.

2.8 Conclusions

In conclusion, we have developed a nanofibre single-photon light source architecture, integrating a quantum emitter into a low loss single mode optical waveguide, and operating at room temperature. Using a novel approach based on momentum spectroscopy, we have quantified the coupling efficiency of individual quantum dots to each nanofibre mode, obtaining large broadband coupling of the emitted light. The momentum spectroscopy method we developed here is also ideal for probing nanofibres with more complex modes, as for example periodically corrugated nanofibres [65], where the induced bandgaps would be evident in the dispersion relation.

The combination of large coupling and propagation length, together with the robustness and flexibility, make these soft-matter nanofibres a potential platform for further optical studies on large scale systems, by connecting them to form a

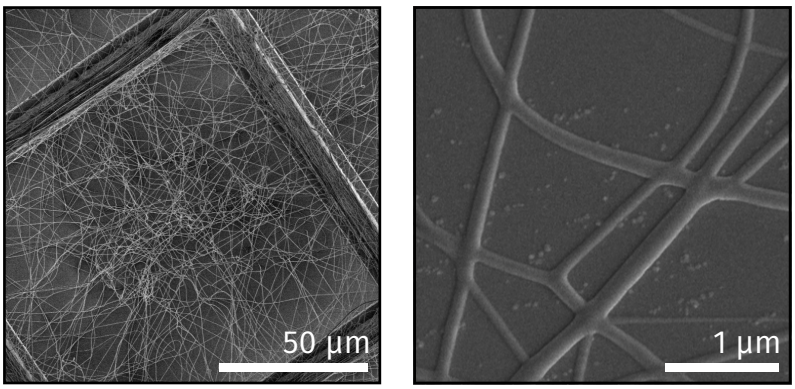

Figure 2.15: Nanofibre networks. a Complex free standing interconnected architectures can be obtained with electrospun nanofibres. b Details of nanofibres (on glass) which have been melted by annealing to form an interconnected networks.

networks (Figure 2.15). On one hand, these fibres can host a large density of dye molecules, for instance obtaining lasing systems. On the other hand, the ability to address single-photon sources have potential for quantum optics applications; moreover, these systems are compatible with cryogenic experiments, and therefore suitable for further studies on coherent interactions.

3 Percolating Plasmonic Networks for Light Emission Control

We study self-assembled semi-continuous gold films and lithographic gold networks characterized by large local density of optical states (LDOS) fluctuations around the electrical percolation threshold, a regime where the surface is characterised by large metal clusters with fractal topology. We develop on the framework of optical nanoantennas which have revolutionised the way we manipulate single photons emitted by individual light sources by enhancing the absorption and emission efficiency; to go beyond the effect of single and few nanoantennas, we fabricated plasmonic networks formed by self-assembly and by electron beam lithography. We study the formation of plasmonic networks and their effect on light emission from embedded fluorescent probes in these systems. Through fluorescence dynamics experiments we discuss the interplay between long-range properties, such as the topology of the network at the percolation phase transition, *i.e.* the formation of a fractal cluster covering the whole structure, and the short-range local features on the order of few nanometers in size which are related to the inter particle gaps and strongly affect the local field enhancement. Our experiments indicate that the fluorescence modification due to local short-range properties dominates over the effect of the collective degree of percolation.

3.1 Introduction

In the previous chapter, we have investigated how the emission of light from a single source can be coupled to the propagating modes of a nanofibre. The system was based on dielectric material, thus avoiding intrinsic losses of metals. However, these structures did not provide emission and light interaction enhancement, *i.e.* the Purcel factor was close to 1, limited by the weekly sub-wavelength spatial extension of the propagating modes. Instead, metallic nanostructures can play a dominant role in light emission control, owing to the potential of plasmon-enhanced light-matter interaction. In fact, the surface plasmon resonances of small metallic particles can lead to enhanced spectroscopy, for instance to achieve increased sensitivity [66], high resolution single molecule localization [67], and enhance non-linear processes [68].

Plasmonic particles allow to squeeze the light to sub-wavelength volumes, resulting in the the arising of electromagnetic hotspots which can increase the absorption and emission of light of emitters by few orders or magnitude [28, 29]. Different particle shapes with increasing complexity have been investigated to tune and strengthen the plasmonic response. Beyond simple spheres and rods many other shapes have been fabricated, as for example nano-shells [69], nano-rings [70] and cylinders with crescent shaped cross section [71].

Here we aim at building extended plasmon networks. When small metallic particles are coupled together, their optical modes hybridise due to near-field interactions and the resulting energy levels shift and split in analogy to molecular orbital formation [72, 73]. Many particles can be also combined in chains, with plasmonic modes delocalised over the chain; the optical response of two-dimensional and three-dimensional chains have been interpreted as composed of the contributions from smaller functional one-dimensional chains embedded within them [74]. Furthermore, coupling of many antennas into dimer, trimers, etc..., can give rise to a novel collective response, as in metamaterials based on array of parallel nanorods [75].

In ensemble of many particles, the position of the electromagnetic hotspots is often difficult to predict [76]. Moreover, the small volume of the hotspots makes it difficult to precisely place the sources in the right location, and the large dependence on the local particle shape make the performance dependent on the fabrication defects. Effects arising from the global properties of the structure, e.g. the mutual interaction of correlated particles ensemble, can instead be more robust. For instance planar deterministic plasmonic architectures have been investigated to engineering broad plasmonic resonances [77], to design transparent metallic

fractal electrodes [78], and to control the optical wavefront with sub-wavelength layers [79].

A more complex two-dimensional arrangement is constituted by metal semi-continuous films. These disordered semi-continuous metal films were firstly investigated by means of scanning near-field optical microscopy (SNOM) showing light localisation into hotspots down to few nanometers and a strong spectral dependence on the probed site on the sample [80]. The localisation and coherence properties in these and other disordered films have been investigated numerically [81] showing a peculiar coexistence at the same frequency of both localised and delocalised modes (the so-called *inhomogeneous localisation*), with eigenmodes characterised by multiple hotspots coherently distributed over large scale. In particular, the near-field intensity fluctuations in random silver films have been studied experimentally and explained in terms of the aggregates size distribution using percolation theory [82].

These systems have been extensively studied by scattering experiments aimed at identifying the plasmonic resonance. For instance, the extension of plasmonic modes at percolation have been recently obtained in wavefront shaping experiments [83] A different approach consists in studying the local density of optical states (LDOS) which, as we have seen in Chapter 1, is a fundamental quantity governing light-matter interaction. The LDOS is hard to probe by transmission and scattering experiments as it relates to all optical modes at a given frequency and spatial position. Instead, it can be obtained by fluorescence studies via the Purcell factor $P = \Gamma/\Gamma_0$, as the ratio between the decay in the medium Γ and the reference decay rate in vacuum Γ_0, given that the spontaneous emission rate of optical emitters is proportional to the LDOS.

LDOS maps require scanning of the probe dipole and can be obtained by the fluorescence dynamics of a source placed at the tip of an atomic forced microscope (AFM) [37, 84], or by scanning the probe source generated by electron impact and then by recording the cathodoluminescence signal [85]. Scanning a sub-wavelength SNOM probe over the nanostructure surface gives information on the LDOS map [86, 87, 88]. These techniques are restricted to small areas of up to few μm^2, and cannot be easily applied to the large systems we are investigating here. In disordered media, the LDOS is best studied statistically. Several works have measured the fluorescence lifetime of molecules or quantum dots dispersed through disordered nanostructures. For example, in polymers films the LDOS fluctuations have been related to the local inhomogeneities of the film [89] and polymer segmental dynamics [90]. In 2D dielectric disordered media the LDOS

has been studied around Anderson localisation [91], while in 3D structures LDOS fluctuations have been measured in the diffusive regime [34], and long long-tailed LDOS distributions have been obtained, and attributed to near-field and far-field interactions [92].

In plasmonic systems, and in particular in semi-continuous metal films, the LDOS statistical distribution of complex plasmonic systems has been recently explored [35]. Fluorescence mapping on these systems has shown an increase in fluctuations of the LDOS which has been linked to the presence of surface plasmons localised modes by relating the variance of the LDOS fluctuations to the inverse participation ratio R_{IP}, which can be used as a qualitative measure of the area occupied by hot-spots. Numerical computations have also allowed to discriminate between radiative and non-radiative contribution to the LDOS [93] and to highlight the dependence on the fluorescent distance between the source and the gold surface [36]. The overall spatial extent of the eigenmodes has been studied numerically estimating the averaged coherence length by computing the cross density of optical states which shows an overall reduction of the plasmonic modes extension around percolation [94].

Our interest in such systems is due to the fact that localised modes enhance the LDOS and therefore induce large Purcell factors while the delocalised ones can propagate the optical excitation to distant locations. Multiple coherent hot-spots would potentially allow an efficient energy transfer between distance light sources. Understanding the nature of such optical modes is therefore of fundamental importance. Here we compare LDOS distributions of self-assembled semi-continuous networks and lithographically ones designed to undergo a percolation transitions by performing fluorescence dynamics studies.

3.2 Self-assembled percolating networks

Semi-continuous metallic films can be obtained by thermal evaporation of noble metals like gold or silver onto a dielectric substrate and subsequent thermal annealing. We fabricated such sample on glass and silicon substrates: the glass substrate is ideal for confocal microscopy, instead the silicon conductive substrate is used here for the high resolution scanning electron microscope images (SEM) shown in Figure 3.1.

We expect the network topology to be qualitatively similar in both cases, nevertheless, electrical conduction experiments (reported later in the manuscript) are used to pinpoint the percolation transition on the glass samples. The properties

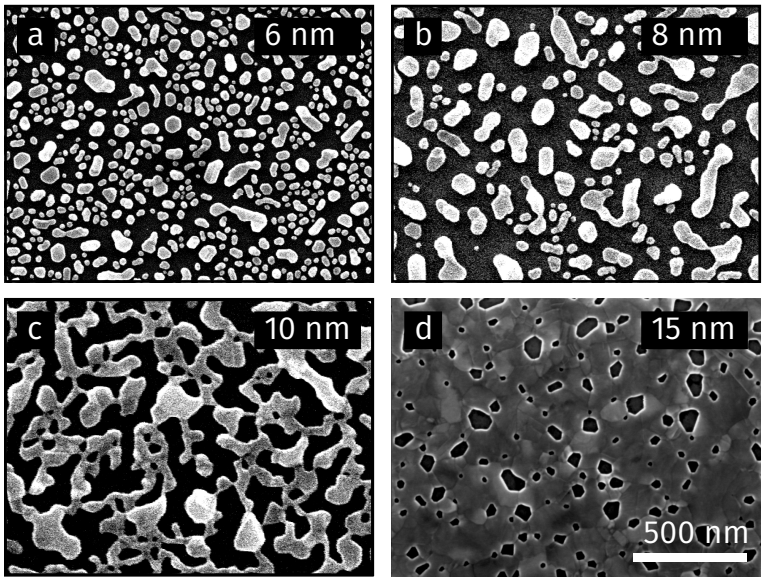

Figure 3.1: **Self-assembled gold films deposited on a silicon substrate**. SEM images of films with different amount of gold, labelled by means of the equivalent thickness t. a $t = 6$ nm: the structure is composed of mostly isolated particles. b $t = 8$ nm: larger isolated clusters form. c $t = 10$ nm: connected clusters develop, the system is above the percolation transition. d $t = 15$ nm: the sample is almost a continuous film with sparse holes. The size bar shown is the same for all images.

of the metal aggregates depend on the growth conditions and substrate and can be controlled by tuning the amount of metal evaporated, which we describe by the equivalent thickness t, which is extrapolated by scaling from large thickness films, as that the thickness the sample would have had if it was a continuous film. For small t the sample consists mostly of isolated metal particles of few nanometers size (Figure 3.1a). As the amount of gold deposited increases, the clusters grow in size with irregular shapes, changing from elongated but isolated objects to more complex structures which touch at multiple points increasing the level of connectivity of the system (Figure 3.1b); it is worth noting that the clusters also grow in thickness, as for instance at $t = 8$ nm the covered area of the sample is smaller than for $t = 6$ nm. Eventually, as the filling fraction increases further, these clusters interconnect with each other at the electrical percolation threshold, when a continuous conducting path of metal is formed between the ends of the film (Figure 3.1c). When more metal is deposited, the system starts looking like an irregular film with holes of smaller and smaller size (Figure 3.1d). As shown in the SEM images, both local properties such as shape and size of the clusters, the gaps and local connectivity, and the global network properties change across the different samples. Furthermore, it has been shown that the fractal dimension

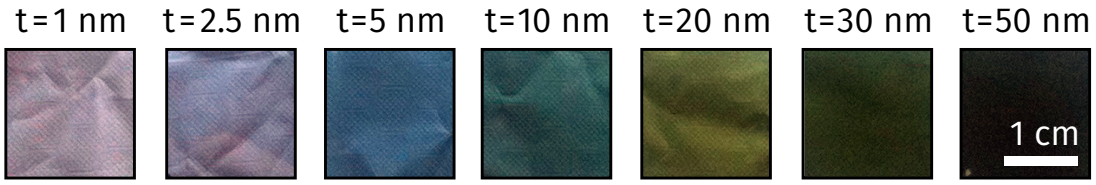

Figure 3.2: Pictures of semi-continuous gold film on glass. Each sample is realised on a 25 mm microscope coverslip. The far-field scattered colour changes with the amount of gold deposited. The size bar shown is the same for all images.

of the clusters in similar structures depends on the filling fraction [35].

The semi-continuous gold networks were made on microscope cover-slip glass substrates by thermal evaporation of gold and no further thermal annealing. The samples have an equivalent thickness ranging from 2.5 nm to 50 nm, as shown in Figure 3.2. Due to the low contrast on the SEM images on non-conducting glass, we verified the crossing of the electrical phase transition by measuring the electrical resistance between edges of the samples with a digital multimeter, as shown later in Section 3.5. The percolation transition occurs at $t \simeq 10$ nm.

3.3 Lithographic networks

Beyond thermal self-assembly, lithographic techniques allow samples of any given topology to be controlled and designed with high resolution [95]. Electron beam lithography (EBL) is a very flexible technique and allows to design and fabricate structures beyond natural limits [96, 97]. Using EBL, we fabricated plasmonic networks exhibiting a percolation transition and fractality similarly to the self-assembled network, but with a mono disperse building block, a gold nanoantenna, and a well-defined degree of percolation. The fabricated networks have an area of $\sim 10 \times 10$ μm^2 and inter-particle gaps of ~ 25 nm, while the building block is a gold nanoantenna of size 60 nm × 40 nm and 40 nm in height. The gold networks have been fabricated on ITO(10 nm)/SiO_2 substrates using Poly(methyl methacrylate) (PMMA) as photo-resist and thermally evaporating 40 nm of gold prior lift-off. We have chosen bond percolating on a square lattice as this is one of the simplest geometries that combines strong near-field hotspots and collective percolation. This is a well-known system which undergoes a percolation transition at a well-defined value, *i.e.* $p = 0.5$ [98]. In our structures, each edge (or bond) of the square lattice is occupied with a probability p with a rod as shown in Figure 3.3. We have created matrixes of up to 20000 elements and filling probability $p = 0.1$, 0.3, 0.4, 0.45, 0.48, 0.5, 0.52, 0.55, 0.6, 0.8 and 1.

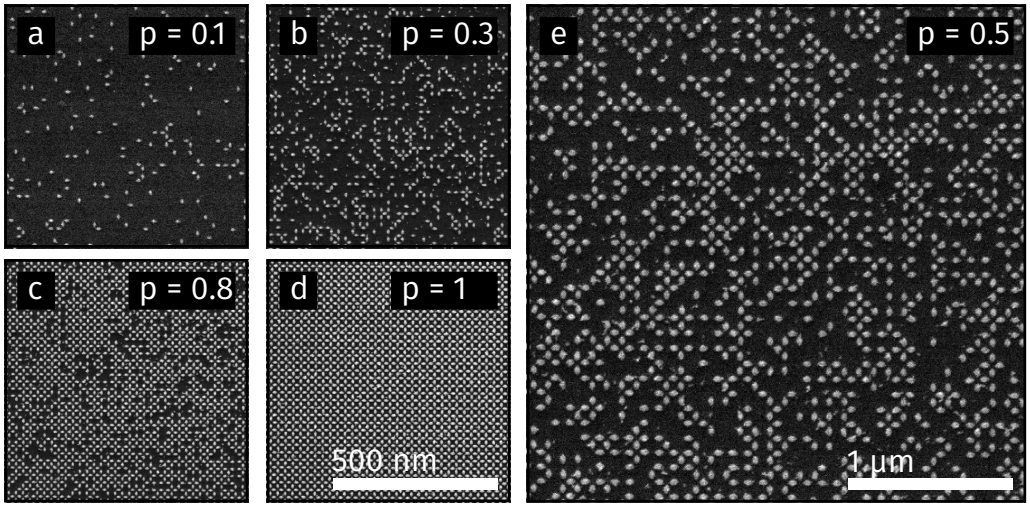

Figure 3.3: SEM images of lithographic gold networks. Lithographic networks are fabricated by EBL on glass substrates. As indicated on the images: a $p = 0.1$, b $p = 0.3$, c $p = 0.8$, d $p = 1$, e $p = 0.5$. Each element of the network is a nanoantenna of size $60 \times 40 \times 40$ (L×W×H) nm. Each network is 10×10 μm^2 and contains $\sim 10^4$ rods.

The nanorods, as sketched in Figure 3.4a, are shaped in order to obtain a narrow gap between them of about 25 nm, a distance that guarantees the near-field coupling between their electromagnetic modes.

In this design the plasmon resonance of the single rod and the coupled system is expected to be in the visible range. The single rod has a plasmon resonance at around 650 nm. The resonance of two touching rods shifts to the infrared [99] while the effect of the hybridisation of the modes of two coupled but not touching rods is not as large [72]; in our case the two-rods resonance occurs at around 720 nm. Although there is no electrical percolation as the rods are not connected, at each vertex of the grid a maximum of four rods can interact and a collective plasmon mode can build up spanning many rods and spread across the system following the rods chain. The electrical field intensity map on the structure upon excitation with a dipole source obtained by finite difference time domain (FDTD) calculations is shown in Figure 3.4b. Beside the field map visualisation, the FDTD simulations also allow to quantify the radiative and non-radiative contribution to the Purcell factor by considering the energy radiated into the far-field and the energy absorbed by the material. For a dipole oriented along the rod long axes and located 7 nm from the rod inside the gap region, the total Purcell factor calculated is ~ 100, dominated by non-radiative terms. In this case, the radiative Purcell factor is ~ 5.

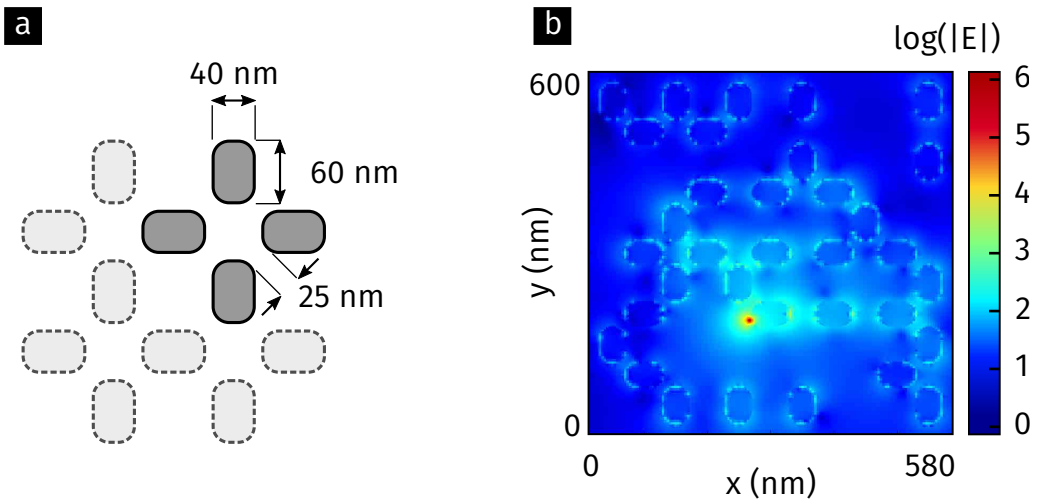

Figure 3.4: Lithographic networks geometry. a Sketch of the sample structure shown in Figure 3.3: each nanoantenna has a size of 40×60 nm and the gap between the nanoantenna tips is ~ 25 nm. b Electric field intensity at $\lambda = 720$ nm obtained by FDTD simulations upon dipolar excitation at the location of highest intensity, 7 nm from the closest gold structure: plasmonic waves of coupled nanoantennas are excited.

3.3.1 Topological properties

The topology of the network evolves with the parameter p as it can be understood by direct visualization. Figure 3.5 shows the results of Monte Carlo calculations on a grid with 100×100 nodes, thus containing up to 2×10^4 rods, which is the same size of the system we fabricated. Panels a-d show specific realisations of the system for different p-values below the percolation threshold (Figure 3.5a at $p = 0.4$ and Figure 3.5b at $p = 0.49$), at the threshold (Figure 3.5c at $p = 0.5$) and above percolation threshold (Figure 3.5d at $p = 0.6$). The cumulative cluster mass distribution is defined as

$$C(N) = \int_0^N f(n) n \, dn \tag{3.1}$$

with $f(n)$ the cluster mass distribution probability, *i.e.* the number of clusters constituted by n elements normalised on the total number of elements. $C(N)$, which is shown below each realisation in Figure 3.5, represents the fraction of the area which is filled with clusters of size up to N elements. The colour code in Figure 3.5 is used to identify the clusters of different size. For small p the system consists of isolated particles or small clusters: at $p = 0.4$ about half of the system is composed by clusters with less than 10 elements, which are represented in blue. The size of the other clusters with more than 10 elements composing the system, which are represented in red, is limited at this filling probability to about

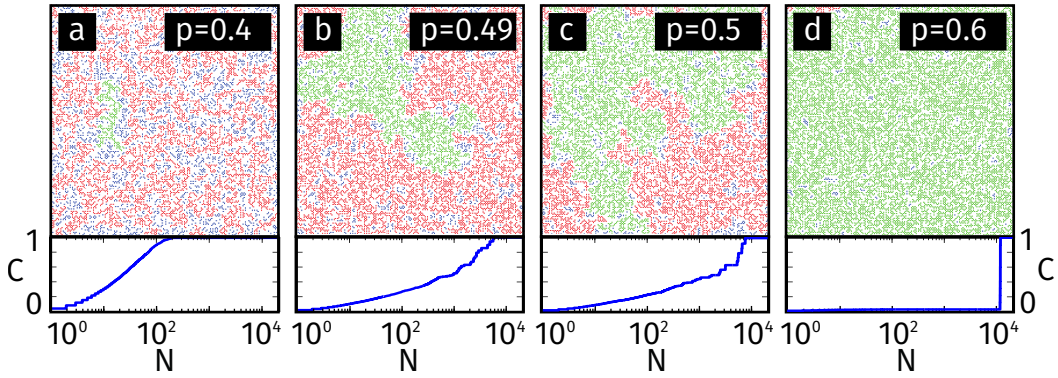

Figure 3.5: Cluster size distributions. Monte Carlo simulations of the nanoantenna network on a 100×100 grid. Realizations at different filling probabilities: a $p = 0.4$, b $p = 0.49$, a $p = 0.5$, d $p = 0.6$. The different colours identify clusters of different sizes: red for clusters with mass bigger than 10 elements, blue for clusters with mass smaller or equal to 10 elements and green for the largest cluster. The cumulative cluster mass distribution $C(N)$ is shown below each structure t At $p = 0.4$ about half of the system is constituted by clusters with less than 10 elements and the maximum cluster size is limited to about 100 nanoantennas. For increasing values of p the average cluster size quickly increases. Above the percolation transition the system is dominated by the percolating cluster.

10^2 elements, which is the size of the largest cluster highlighted in green. As the p increases larger clusters appear with a higher probability and the largest cluster starts to dominate the size distribution when the system approaches the percolation threshold, for instance at $p = 0.49$. At the phase transition ($p = 0.5$) the size of the largest cluster diverges reaching the system size. Above the threshold, the percolating cluster alone dominates and fills almost the whole system apart from few detached clusters of decreasing size.

In order to highlight the percolation transition, we computed the average cluster mass weighted with the cluster mass, which is defined as

$$m = \langle f(n)\ n \rangle\ . \tag{3.2}$$

As $f(n)\ n$ is the fraction of area filled by clusters with n elements, m corresponds to the average mass of the cluster that one would select by choosing a random point of the structure. As shown in Figure 3.6a the average mass grows smoothly far from $p = 0.5$ both in the low and high p range, while it grows quickly approaching the phase transition. We estimate the cluster extension by means of the radius of gyration

$$R_S = \frac{1}{n} \sum |\boldsymbol{r}_i - \boldsymbol{r}_{cm}|^2\ , \tag{3.3}$$

which is the root mean square distance of the elements from the centre of mass

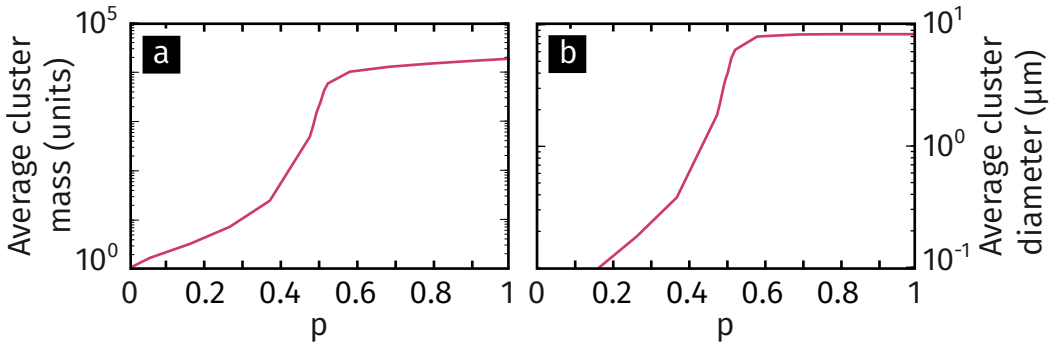

Figure 3.6: Average cluster size. [a] The average cluster mass and [b] the average cluster diameter on a 100×100 grid as a function of the percolation parameter.

of the cluster $\boldsymbol{r}_{cm}$. The average cluster diameter weighted with the cluster mass is

$$d = 2\langle R_S f(n)\, n\rangle \,, \tag{3.4}$$

which is shown in Figure 3.6b.

Two topological properties, the cluster diameter and cluster fractality are expected to be important for the optical properties of the plasmon modes. A plasmon wave is bounded to the metal, and while propagating loses energy both by out-of-plane scattering and by ohmic absorption in the metal. These effects are reflected in the plasmon propagation length l_p which in continuous gold films is typically $5-20$ μm [100]. The optical interference which determines the plasmon modes is limited to components within a length of the order of l_p. The comparison between the cluster diameter and the plasmon propagation length l_p is therefore a good indicator of how the plasmon excitation will spread in the system. If the cluster size is smaller than l_p then its shape and boundary will affect the hybridised plasmon mode and the optical response. Instead, if the cluster size grows larger than l_p, the plasmon response will saturate at a level that will not depend any more on the cluster boundary as no optical excitation will be able to probe it. In our networks in the region $p = 0.3-0.5$ the average cluster diameter grows quickly, approaching the sample size of 10 μm, and eventually crossing the plasmon propagation length (see Figure 3.6b).

The second topological property, the fractality, is harder to be taken into account as it is a multiscale property which acts both on the local features and nanogaps as well as on the long-range shapes. At the phase transition the percolating cluster diverges in size, the structure is self-similar and the clusters are known to be fractal. Besides the average cluster diameter, which is an obvious

topological measure, also the fractal dimension is expected to have very important relation with the optical properties of the plasmon modes. For example, in the self-assembled networks, the degree of fractality of the system, calculated as the ratio of fractal to non-fractal (Euclidean) clusters, has been connected to the normalized variance of the LDOS [35]. For bond percolation networks, the fractal dimension D can be defined as the scaling of the cluster mass versus the area, *i.e.* $m \propto R_S^D$ [98]. At the percolation threshold, the 2D bond percolation model used to design the lithographic networks is known to have a fractal dimension D = 91/48 [98], a typical value for 2D systems; similar values have been found also in semi-continuous films [35, 101]. Above the percolation threshold the gold network evolves towards a continuous uniform film with Euclidean dimension $D = 2$, while for very small values of p the network consists of isolated antennas with no fractal properties and again Euclidean dimension $D = 2$. A crossover between a fractal and a Euclidean network is therefore expected in the region $p > 0.5$.

3.4 Fluorescence dynamics studies

As described in Section 3.1, the LDOS can be extracted from the decay rate of an emitter. We performed fluorescent dynamics measurement via confocal microscopy with individual fluorescent point-like sources dispersed on the surface of the sample. We used dye-doped polymer beads (polystyrene- divinilbenzene) of nominal diameter 50 nm internally doped with red Firefli dye molecules (Thermo Scientific, absorption 542 nm, emission 612 nm). Each bead contains more than $\sim 10^2$ molecules and has a well-defined orientation-independent optical response and decay time that we measured to be $\tau = 5.5 \pm 0.3$ ns ($\langle\tau\rangle \pm \sigma$, where σ is the standard deviation of the distribution) on a glass substrate. The beads were randomly deposited on the structure by spincoating with an average density of ~ 1 bead per μm^2. A 532 nm laser (Nd:Yag second harmonic) with a 10 MHz repetition rate and 100 ps pulses width is used to excite the fluorescent source through an oil immersion objective (NA = 1.45). The same objective collects the light emitted which is directed to an avalanche photodiode (APD) for detection coupled to a time correlating single-photon counting (TCSPC) card for temporal analysis. The beads are identified by scanning the sample by means of a piezo stage and measuring the emitted photons with the APD for an integration time of 1 ms per pixel and a pixel size of 100 nm, as shown in the inset of Figure 3.7. The lifetime of each bead was collected by increasing the acquisition time of the TCSPC to ~ 10 s at a typical laser power of around 1 μW. Typical results are

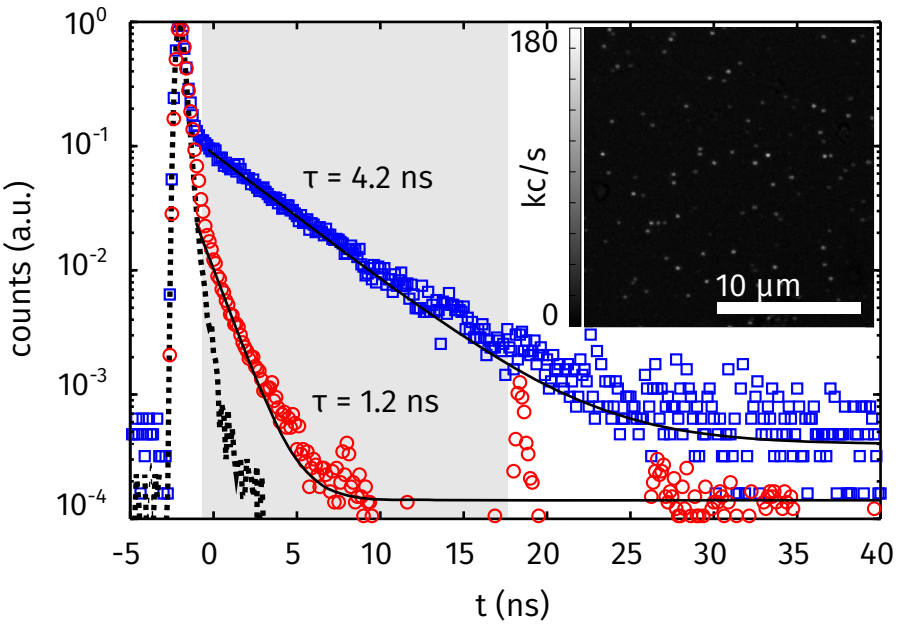

Figure 3.7: **Lifetime measurements**. Lifetime histograms from two emitters at two different positions on a self-assembled network, with high (red open circles) and low (blue open squares) decay rates. The initial peak with very short lifetime comes from the gold self-fluorescence which is resolved as the instrumental response (shown with the black dashed line). The continuous line through the data is the single exponential fit. The spurious signal at $t = 18$ ns is due to after-pulsing which is a common electronic artefact. In the inset, confocal scan on a 20 μm by 20 μm area of the sample which allows to identify the positions of the sources.

plotted in Figure 3.7.

We fitted the data with a single exponential function in the region highlighted in Figure 3.7. The small deviations from the single exponential decay are due to the averaging over the position and direction of the molecules inside the beads which experiment slightly different LDOS as they are at different distances from the gold surface. The large component with very short lifetime, which is more prominent in the self-assembled networks is attributed to gold self-fluorescence. It shows as a peak at short time which is the result of the convolution of a very fast signal with lifetime < 10 ps (as previously reported [102]) with our instrumental response (~ 400 ps). After this first peak, the signal is due to the beads fluorescence. The component we analyse is in the range $2-18$ ns (highlighted in Figure 3.7) with a lifetime in the range $1-5$ ns. For longer times, the signal merges with the background. A peak at $t = 18$ ns is due to after-pulsing in the APD which is an electronic artefact of this type of electronics. The typical statistical error of the fit is $< 5\%$, much smaller than the typical lifetime variation observed.

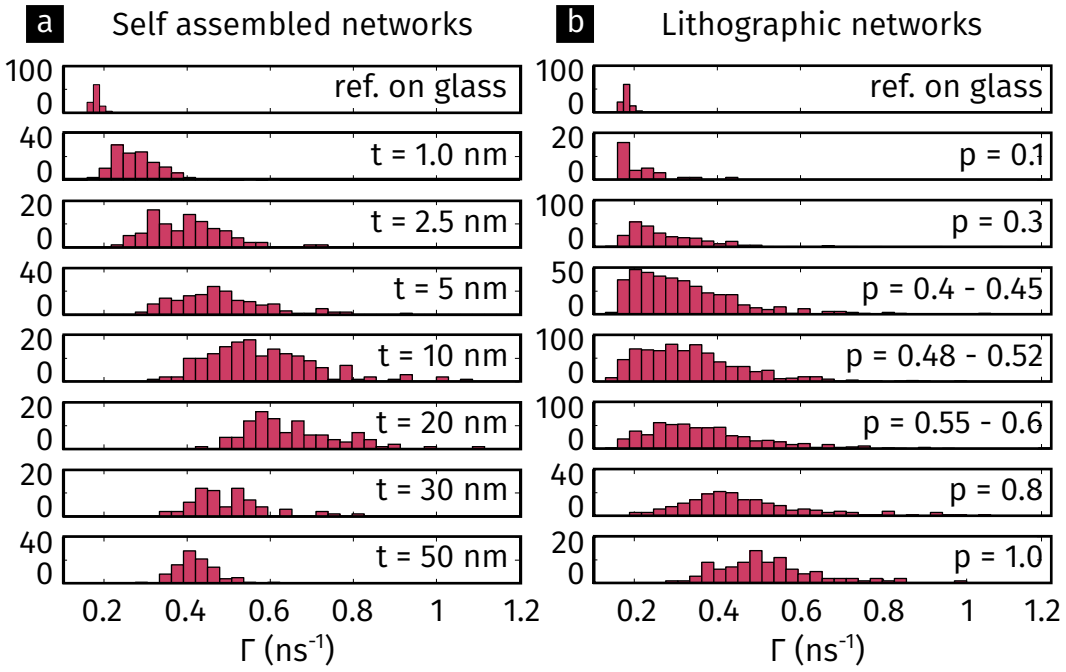

Figure 3.8: Local density of states distributions. a Decay rate statistics of self-assembled networks as a function of the equivalent gold thickness. b The same for lithographic networks as a function of the percolation parameter p. A change of width and position of the decay rate distribution is visible for both cases. The maximum average Purcell enhancement (~ 3) and the maximum variance for self-assembled networks is between an equivalent thickness of 10 to 20 nm which corresponds to the electrical percolation transition. The effect in the lithographic networks is less pronounced and occurs for large p values, beyond the percolation transition. For small p values the distributions are dominated by a significant amount of beads on glass, uncoupled to the structure which accumulate to low decay rates values. The maximum Purcell factor and the maximum FWHM of the distribution occurs towards the full samples ($p \sim 0.8-1$), far from the percolation transition.

3.5 LDOS distributions

We performed an extensive decay rate statistics by collecting the lifetimes of up to 300 beads for each sample. In the case of the self-assembled networks which extend over a few cm^2, a few different areas of the same sample were measured. In the case of lithographic structures several realisations of the networks at the same p where measured on the same sample. The decay rate distributions are shown in Figure 3.8.

The topmost histograms are the references, *i.e.* the decay rate distribution for beads on a glass substrate, which have an average value $\Gamma_0 = 0.18$ ns^{-1}. In both the self-assembled and the lithographic systems the decay distributions change shape and broadens as compared to the reference. From the top to the bottom

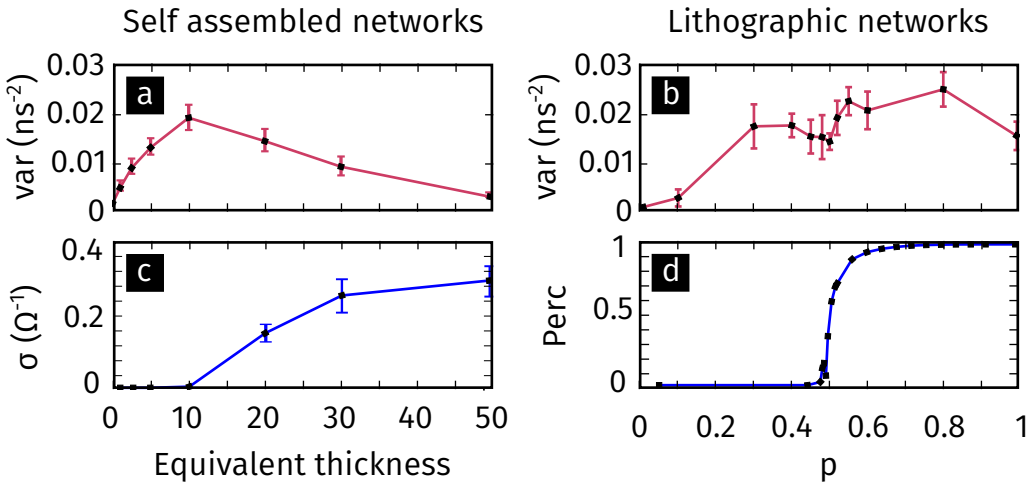

Figure 3.9: **Local density of states and percolation transition.** [a] [b] The variance of the LDOS distributions shown in Figure 3.8 for the self-assembled and lithographic networks respectively. [c] The measured conductibility for the self-assembled network, confirming the crossing of two electrical phases at around 10 nm in correspondence of the maximum of the variance. [d] The percolation function, i.e the probability that a randomly chosen nanoantenna belongs to the percolating cluster computed by Monte Carlo simulations for the lithographic networks.

of Figure 3.8a and 3.8b we present the decay rate distribution resulting from the experiments on networks with increasing filling ratio, which we indicate by \the equivalent thickness t for the self-assembled networks and by the filling probability p for the lithographic one. For the lithographic networks measurements within the p-range of $0.4-0.45$, $0.48-0.52$ and $0.55-0.60$ have been combined. The maximum mean Purcell factors are in the range $0.8-5$ in both cases.

The variance of the distributions is plotted in Figure 3.9a and 3.9b: in both cases the variance of the decay rate distribution increases for increasing value of t and p, as compared to the reference. For self-assembled networks, the variance increases reaching a maximum at around $t = 10$ nm, which corresponds also to the maximum Purcell enhancement, and then decreases to smaller value in the thicker samples. This maximum occurs together with a change in topology in the network, which changes from disconnected clusters to a uniform plasmonic structure. Electrical conductivity measurements confirm the crossing of two electrical phases at around 10 nm as shown in Figure 3.9c. For lower values of deposited gold the conductivity is almost zero, while it grows abruptly once percolation is established just above 10 nm. This value of t corresponds to the peak of the variance in Figure 3.9d. The behaviour of the self-assembled networks we report

is consistent with works on similar samples as shown in Reference [35], although here the variance presents a smoother increase rather than an abrupt increase around the percolation value.

The decay rate distribution from the lithographic networks shown in in Figure 3.8b broadens as p increases but present a different general trend. For small p values the decay distribution is peaked at the same value as the reference, indicating that a significant fraction of the sources maintain an almost unchanged decay rate which we attribute to sources on glass, far and thus not coupled to the gold clusters. This is due to the low gold filling fraction of the system. On the contrary, the smaller grain size of the self-assembled networks guarantees a dense covering of the sample surface down to the nanometer size at any filling ratio. In the lithographic networks, until $p < 0.5$ the distribution grows a long-tail toward larger Γ but no real shift of the mean is visible. For $p > 0.6$, where the network is covered almost everywhere by the percolating cluster, as shown in Figure 3.5d, the distribution shifts to larger values of the decay rate and the maximal values are achieved towards the higher density samples, towards $p = 1$. The marked difference with the self-assembled networks is a monotonic increase of the mean and variance of the distribution which does not seem to decrease again, nor to have a special behaviour around the percolation transition. This transition is expected at $p = 0.5$ as highlighted in Figure 3.9d by plotting the percolating function Perc(p), which is the probability of a rod to be part of the percolating cluster and is thus related to the conductivity of the system [103]. Below $p = 0.5$, there is no percolating cluster. At $p = 0.5$, where the percolating cluster begins to dominate the network, the probability that the antenna is part of the percolating cluster rapidly increases and for $p > 0.6$ it grows linearly as almost all rods which are added to the system are in the percolating cluster. Comparison of Figure 3.9b and Figure 3.9d indicates that the decay rate variance on the lithographic networks does not show a well-defined relation with the topological percolation transition. Only a minor dip in the variance is visible at $p = 0.5$, instead of the maximum of the self-assembled networks shown in Figure 3.9a.

In Section 3.3.1 we have discussed the cluster size and the cluster fractality as two aspects which are expected to affect the plasmon response of the system. In the case of the lithographic networks these quantities can be calculated, therefore an assessment of their role can be attempted. In the region of very small p-values the spatial extension of the plasmonic modes l_p is expected to be larger than the average clusters size d which is < 1 μm. For increasing values of p we expect the cluster size d to become larger than l_p and therefore to saturate

the optical response. Such an effect does not appear in our data. However, it is worth noting that the large number of uncoupled beads makes the analysis in the region below percolation difficult. Regarding the fractality of the system, for a 2D bond-percolating network structural fractality occurs only in a small region close to $p = 0.5$ while the system is not fractal, as discussed in Section 3.3.1 , both for very small p-values or in the region $p > 0.5$ when the percolating and large clusters dominate the system. Our data do not show an evident effect related to the fractality around $p = 0.5$. On the contrary, the general shift of the distribution happens for $p > 0.6$, when the percolating clusters spans already all the system. For $p > 0.6$ the main structural difference is the local connectivity of the system: the sample is always dense but as p increases the average number of linked rods at each node (equal to $4p$) approaches its maximal value of 4. It has to be noted that for self-assembled networks the fractality of the system can extend down to the nanometer level, thus resulting in gaps between the metal particles of nanometer size; on the contrary the lithographic networks always present a fixed gap of ~ 25 nm.

Another difference between the self-assembled and lithographic networks is related to the network shape as while in the former the components are physically connected, in the latter the rods are spaced by ~ 25 nm. As we discussed in Section 3.3, both networks are optically connected as the plasmons couple from rod to rod, instead the self-assembled ones are also electrically connected. This design was chosen to highlight the topology-related effects over those coming from the resonant natures of the elements composing the network. Our results seem to indicate that more attention and future investigations are required to fully understand the impact on the LDOS distribution of the resonant response, changing with the percolation paramenter and extending to the IR.

3.6 Conclusions

We have fabricated metal percolation networks by thermal self-assembly of semi-continuos films and by EBL fabrication of gold nanorods matrices. We have investigated the LDOS distribution for different filling ratios of the systems by measuring extensive statistics of decay rate and we have compared the broadening and shift of the distributions in the two cases. While both the average Purcell factor and the variance of the decay rate distribution evolve following the network topology, in the self-assembled films they peak close to the percolation threshold, while for the lithographic case the most significant effect is not observed in the

vicinity of the percolation transition but at higher filling probabilities. These considerations suggest that the effect on fluorescence modification is dominated by the local properties such as node connectivity and number of nanorods around each position and are much less influenced by the degree of percolation, the fractality or the extension of the modes. It is tempting to extend the results of this observation to the self-assembled networks, but the lack of real control over the topological parameters and a change of the shape of the building block with t makes this far-fetched.

4 Spectral analysis of diffusive random lasing: tuning the emission and probing the chemical environment

We study random lasing, *i.e.* amplification of light in a medium with multiple scattering, in which light propagation can be described by a diffusion equation. We focus in particular on how the spectral characteristics of the lasing emission and threshold behaviour depends on the physical properties, such as the sample size, composition and mesoscopic structure, and chemical parameters of the system, *i.e.* the dye molecule properties, by extending existing diffusive models including the full spectral features. We solve a multimode diffusion model and calculate multiple light scattering in presence of optical gain which includes dispersion in both scattering and gain. In the first part of the chapter we present a detailed numerical investigation of the tunability of random lasing in photonic glasses when the resonances of monodisperse Mie scattering particles are controlled via the particle size. In the second part of the chapter we focus on how the chemical properties of the dye constituting the gain affects the emission. In particular, building on the fluorescence sensing technology, we show how this can constitute a promising sensing scheme, also providing a proof-of-concept experimental realisation.

4.1 Introduction

Hitherto, we have considered either isolated or localized emitters and focused on their interaction with the environment. In this chapter, we study a system composed of many emitters ($\sim 10^{16}$–10^{17} per cm^3), distributed into disordered media. In such conditions, newly collective phenomena may occur. In particular, the emission by stimulated radiation may become dominant leading to lasing emission. These systems are known as random lasers and are the topic of this chapter. Despite its potential for practical applications [43], random lasing technology is still in its infancy with pioneering applications such as low coherence light source [104] and sensing [105, 106, 107]. The difficulty of controlling the wavelength and directionality of the emission is one of the factors that has limited practical applications. In conventional lasers the lasing emission can be tuned by engineering the high finesse cavity which provides the feedback and thus defines the lasing mode. In random lasing instead, feedback is provided by multiple scattering and the lasing emission properties are determined by the complex interplay between gain and losses. Recent experiments have shown lasing emission controlled by exploiting scattering dispersion via resonant scattering sustained by spherical particles [108, 109] or by gain dispersion achieved by artificially increasing absorption in a spectral band [110]. Active tuning of the lasing properties has also been achieved by shaping the pump profile to selectively excite one or a few lasing modes [111, 112, 113]. Two main regimes are usually considered: a *coherent feed-back regime* characterized by narrow spikes ($\ll 1$ nm) above threshold, strongly sensitive to the local scattering properties, with chaotic behaviour and large pulse to pulse variability; a *diffusive regime* in which, due to for example a long pumping pulse or large excitation area, the interference does not directly appear in the recorded emission due to the averaging of a large number of modes, leading to a smoother emission characterized by a narrowing of the emission down to few nanometres. Here we will focus on diffusive systems.

This chapter is divided in two parts: in the former a diffusive model is employed to investigate numerically the range of tunability of a photonic glass system with resonant scattering, describing for instance a system composed by monodisperse particles. In the latter, the application of random lasing systems as a sensing device exploiting the inherent light-matter interaction enhancement and its non linear response is investigated with the same numerical model and experimentally realised on a biocompatible system.

4.2 Diffusion of light

Light is a vectorial wave phenomenon, which is fully described by Maxwell equations. When considering disordered systems, the complete solution of the electromagnetic problem on system of randomly varying refractive index is often impractical. Moreover, the solution depends on the actual microscopic properties of the realisation under examination, requiring to perform an average on multiple disorder realisations to obtain the observable quantities. Instead, different procedure lead to approximate solutions of which the diffusion approximation is one of the simplest, yet has proven to be describe very well the multiple scattering regime in opaque media. In this approximation, the interference effects are neglected as they are averaged out by a large amount of independent scattering events from randomly positioned particles. The transport is independent from the wave nature of light, which is instead described by its intensity distribution $I(\boldsymbol{r}, t)$, while the media properties are described by a diffusion constant D, independently from the microscopic properties of the scatterers. The light intensity density $I(\boldsymbol{r}, t)$ obeys the diffusion equation:

$$\frac{\partial}{\partial t} I(\boldsymbol{r}, t) = D \nabla^2 I(\boldsymbol{r}, t). \tag{4.1}$$

This macroscopic approximation can be derived from the mesoscopic length-scale in the framework of the Radiative transfer equation [114] or from the "ladder approximation" of the Green function expansion of random point scatterers at the microscopic length scale [115].

The most relevant physical quantity in a diffusive system is the transport mean free path ℓ_t, which corresponds to the average path required to fully randomize light propagation:

$$\ell_t = \ell_s / (1 - \langle \cos(\theta) \rangle, \tag{4.2}$$

where ℓ_s is the average distance between scattering events and θ is the scattering angle, from which the diffusion constant is obtained as:

$$D = \ell_t v / 3,$$

where v is the speed of energy in the medium. Compared to ballistic propagation, the diffusion relation gives rise to a linear intensity decay inside the medium, the so called Ohm law for light, as shown in Figure 4.1 (blue line). In presence of absorption with extinction length ℓ_a, the scattering further decreases the propagation depth to $L_a \propto \sqrt{\ell_t \ell_a}$ (orange line).

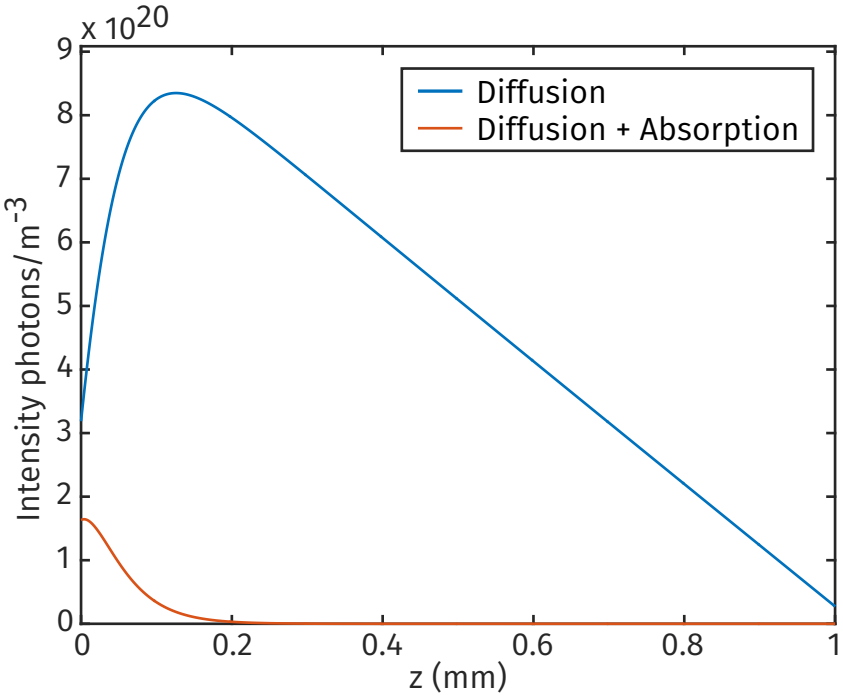

Figure 4.1: **Diffusion of light**. 1D diffusive system ($\ell_t = 40\,\mu$m) is pumped from the front surface ($z = 0$). Beside the initial transition from a ballistic to the diffusive regime for $z \lesssim \ell_t$, the propagation of light in a diffusive medium results in a linear decrease of the intensity with the depth (Ohms law for light, blue line). In presence of absorption ($\ell_a = 56\,\mu$m) the penetration depth is strongly reduced (orange line).

The same framework has proven to describe very well light propagation in scattering media with gain in a large variety of realistic conditions.

4.3 Diffusive random lasing modelling

Different theoretical approaches to model random lasing action have been developed. For uncorrelated random systems in which interference between the scattered waves can be neglected, diffusive models as introduced in the previous section are very accurate even in presence of optical gain [116, 117] and they provide the time evolution of the lasing process and a smooth lasing spectrum with no spiking lasing behaviour [118]. The radiative transport model with gain can also be solved for instance with Monte Carlo simulations which consider a random walk of photons [119, 120] and in which amplification of single paths can be important in defining the spectral properties [121], and by solving the complete radiative transfer equations [122]. These approaches allow the study of large systems (> 100s mean free paths) and geometries similar to real experiments. More complete models including field calculations and interference effects

have been developed, based for example on Maxwell-Bloch equations [123, 124] and the finite-difference time-domain solution of Maxwell equations in nonlinear media [125, 126, 127], but typically limited to volumes of a few wavelengths cubed.

Given a diffusive system with diffusion constant D, the optical gain, typically provided by organic molecules, is described by the stimulated emission cross-section σ_e, the absorption cross section σ_a, and the lifetime of the excited state τ. The molecules composing the gain can be brought to the excited state by an intense pump laser. Here we label N_1 the density of molecules in the excited state, which defines the gain length $l_g = (N_1\sigma_e)^{-1}$, and N the total molecule density. We model a translational invariant slab geometry similar to most experiments with the 1D diffusion equation for the pump $W_p(x,t)$ and the emitted light $W^i(x,t)$. These equations are coupled to a four level system gain described by one rate equation for the radiative transition. The set of equation is the following:

$$\frac{\partial N_1}{\partial t} = \sigma_a W_p[N - N_1]v - \sum_i \sigma_e^i W^i N_1 v - \frac{N_1}{\tau} \tag{4.3}$$

$$\frac{\partial W_p}{\partial t} = D\frac{\partial^2 W_p}{\partial x^2} - \sigma_a W_p[N - N_1]v + \frac{I_p}{\ell_e} \tag{4.4}$$

$$\frac{\partial W^i}{\partial t} = D\frac{\partial^2 W_i}{\partial x^2} + \sigma_e^i W^i N_1 v + \Phi\frac{\varphi^i}{\tau}N_1 \tag{4.5}$$

where the emitted light is discretised in spectral bands λ_i, and $i = 1..n$. $I_p(x,t)$ is the intensity temporal profile of the pump, ℓ_a is its absorption length and v is the velocity of light in inside the medium, and Φ is the quantum efficiency of the process. The spontaneous emission (fluorescence) spectrum defines the quantities φ^i, with $\sum\varphi^i = 1$. We solve the diffusion equations (4.3-4.5) by means of standard ODE solvers implemented in MATLAB for typical experimental configurations by including the full spectral dispersion of both scattering and gain, beyond the stationary case [116] and few modes model [118], and we calculate the full spatial, spectral and lasing dynamics, including mode competition and threshold variation. The main advantage of this multimode diffusive model is that it includes spectral dispersion of scattering, absorption and gain, without any assumptions about the β parameter, which compared to previous works [117, 110], is not a free parameter any more, but comes as a solution to the problem.

We choose to simulate typical experimental conditions [108]: the sample is a slab 50 μm thick, with $\ell_t = 1.5$ μm, and doped with a concentration of 1mM of rhodamine 6G dye whose emission properties are taken from Ref. [128], and the quantum efficiency is assumed to be unity ($\Phi = 1$). The system is pumped with a 6 ns laser pulse at a wavelength of 532 nm.

Firstly, we consider a conventional RL, such as a polydisperse TiO_2 powder, where ℓ_t is not dispersive but roughly constant over the gain spectrum. In Figure 4.2 we plot the peak spectral fluence diffusing from the system at the air-sample interface together with the full width half maximum (FWHM) of the emission spectra as a function of the pump energy density. The onset of the lasing emis-

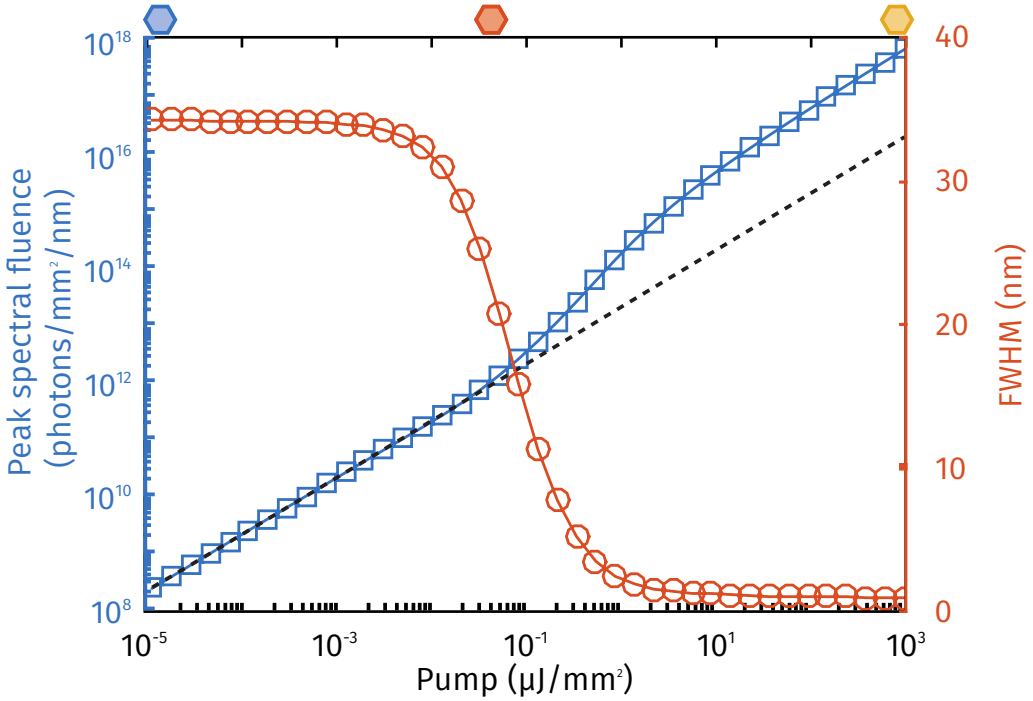

Figure 4.2: Characteristic plot of a random laser. The total peak intensity (blue squares) and FWHM of the emission spectrum (orange circles) are plotted for increasing pump energy density for a slab system of thickness $L = 50\ \mu$m, transport scattering length $\ell_t = 1.5\ \mu$m, and a 1 mM concentration of rhodamine 6G providing the gain, excited by a single pulse of duration $d = 6\ n$s at 532 nm. The black dashed line is a guide to the eye to highlight the change of regime from fluorescence to lasing.

sion is at $P = 0.07$ mJ/mm^2, at higher pump intensities the peak fluence increases super-linearly until gain saturation is reached; at the same time the emission width quickly decreases from the broad fluorescence emission to a narrow almost constant value at saturation. The threshold of the lasing emission is usually identified in analogy to conventional lasing by considering the change in slope of the pump-peak emission intensity relation or by considering the narrowing of the lasing emission. We identify the threshold as the half narrowing of the emission spectrum, which is a typical experimental parameter more accessible than the change of slope [129]. The FWHM of the emission narrows from the initial ~ 35 nm of the rhodamine fluorescence spectrum to ~ 0.8 nm of maximum lasing narrowing. The β parameter can be calculated from Figure 4.2 to be $\beta \simeq 0.04$.

In Figure 4.3 the emission spectra below and above threshold and for an intermediate value are shown. Lasing occurs at the maximum of the gain, which is $\lambda = 555.5$ nm. The width of the lasing peak is limited by the losses through

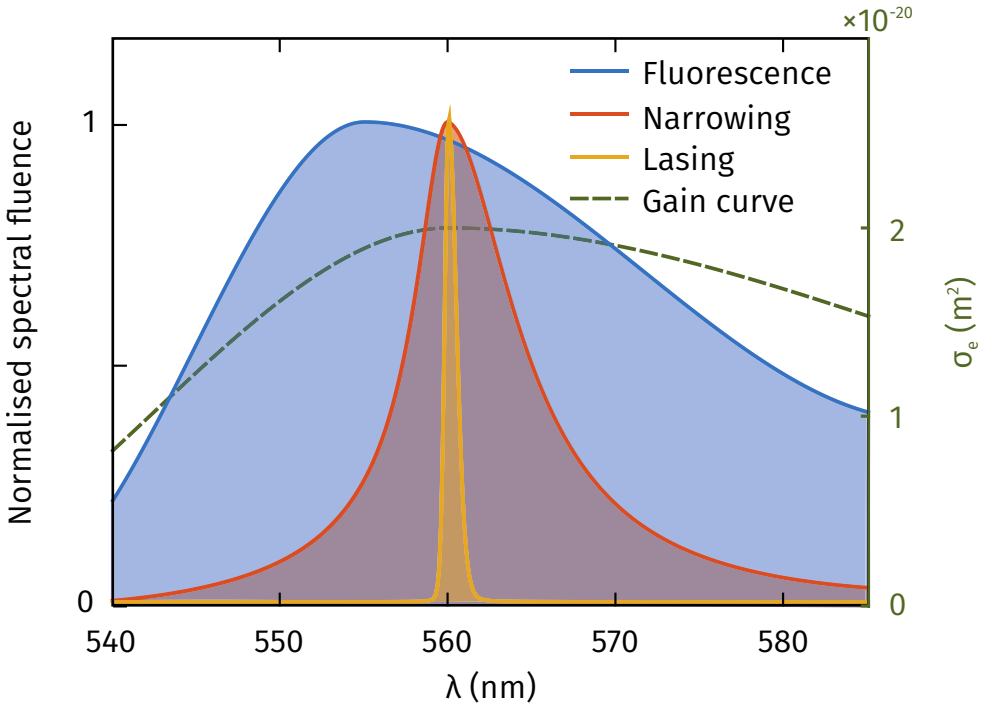

Figure 4.3: Random lasing emission. The emission spectra (normalised) are reported at different pump intensities: the fluorescence spectrum (blue) narrows down for increasing pump intensity (red line) down to a 0.8 nm FWHM (yellow line). The corresponding pump intensities are colour coded by the hexagons in Figure 4.2. The lasing occurs at the maximum of the gain curve (dashed green line).

the sample boundaries and by the gain saturation, and, as we confirmed, it is not affected by the numerical spectral discretisation which is set to 0.1 nm. This value differs from the typical experimental observations where the final linewidth is typically in the range 5–10 nm [129, 108], as we are not considering any additional homogeneous and inhomogeneous line-broadening effects, nor the underlying complex multimode nature of the lasing peak.

4.4 Tuning random lasing in photonic glasses

In this section we investigate the range of tunability of a diffusive random lasing with intensity feedback when Mie resonances are excited. The model presented in the previous section allows us to investigate a realistic photonic glass made of latex spheres and rhodamine and to quantify both the lasing wavelength tunability

range and the lasing threshold.

We consider now the case of a medium characterised by resonant Mie scattering. We simulate a system composed of close-packed ($n = 1.6$, filling fraction $f = 0.5$) dielectric spheres with 1% radial polydispersity. We calculate ℓ_t by using Mie theory in the approximation of independent scatterers [130]. The Mie resonances modulate ℓ_t as shown by the full lines in Figure 4.4a, where scattering is plotted together with the predicted lasing peaks for three sphere diameters. Qualitatively, the lasing frequency is pulled towards the strongest scattering frequency within the gain curve. Compared to what is shown in Figure 4.3b, now the lasing frequency can be tuned by choosing the Mie resonance.

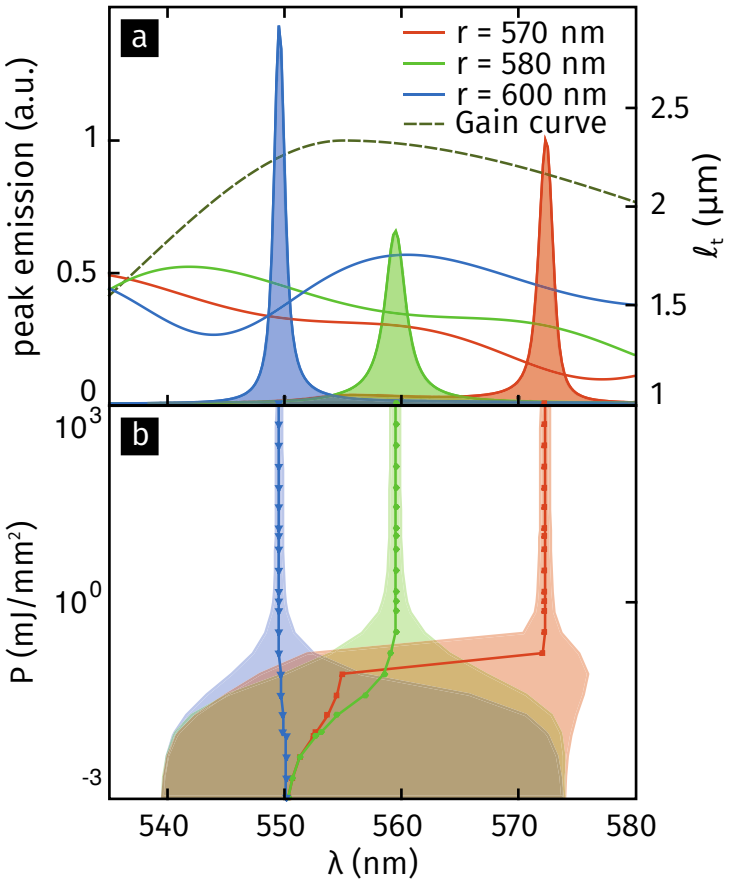

Figure 4.4: Effects of resonant scattering on the lasing spectrum. a The Mie resonances of spherical scatterers ($n = 1.6$ in air) of similar size (polydispersty 1%) are exploited to tune the lasing emission. The emission wavelength is close to the minimum of the transport mean free path (shown with the same colour of the corresponding lasing peak) while inside the gain region (black line). b At increasing pump power the emission peak wavelength shifts from the fluorescence maximum to the lasing wavelength, stabilizing above threshold.

Figure 4.4b shows the narrowing and shifting of the emission peak while increasing the pump energy. The crossing of the lasing threshold is now evident as

a narrowing of the emission spectrum while the lasing peak shifts away from the maximum of the fluorescence curve. Frequencies close to the maximum of the gain initially dominate, as they receive a larger fraction of the spontaneous emission, but those with larger scattering and gain eventually prevail above threshold.

Finally, we study the range of tunability that can be achieved by resonant scattering. In Figure 4.5a we present the calculated transport mean free path at $\lambda_{\text{gain}} = 555.5$ nm, which is the wavelength corresponding to the maximum of the gain. For very small scatterers, which are in the Rayleigh regime, the scattering

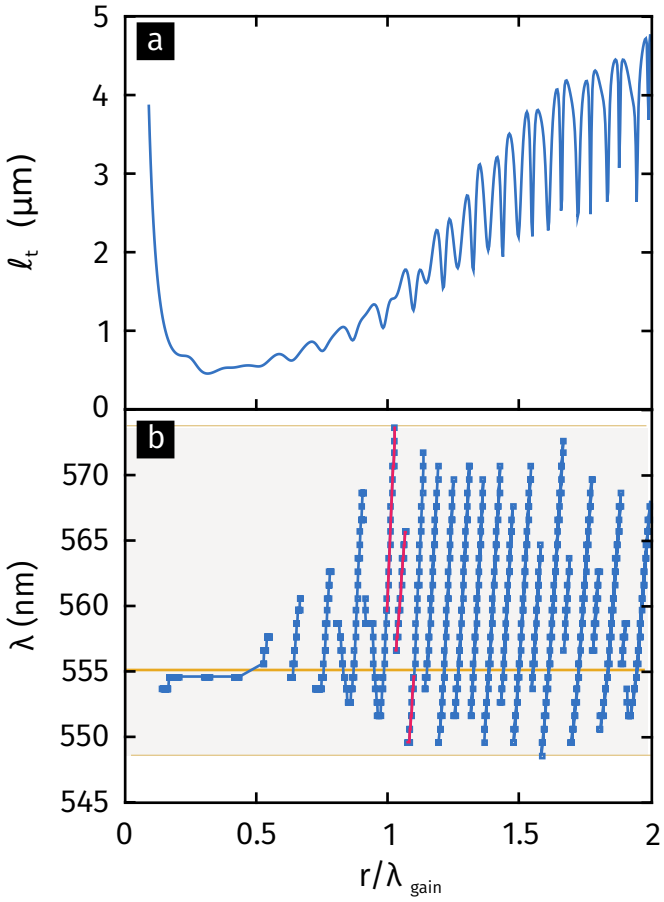

Figure 4.5: Tuning the lasing emission wavelength via resonant scattering. a Transport scattering mean free path ℓ_t computed by Mie scattering (spheres of refractive index $n = 1.6$ in air, filling ratio $f = 0.5$ and 1% polydispersity) at $\lambda_{\text{gain}} = 555.5$ nm. b Lasing emission wavelength for resonant scattering. When the particle size is increased from non-resonant Rayleigh scattering ($r \ll \lambda$) to Mie scattering, the lasing emission wavelength is tuned to follow the scattering resonance in a range of 25 nm inside the gain curve (grey area). The red lines are further plotted in Figure 4.6a.

increases with the particle size; instead this trend is reversed approaching the Mie regime. The minimum scattering length is achieved at $r \lesssim \lambda/2$, which corresponds to the onset of the first Mie resonances; subsequently ℓ_t increases with

a resonant behaviour, while the resonances get closer and closer. As previously shown in Figure 4.4, this modulation in the scattering induces a tuning of the emission wavelength which is now explicit in Figure 4.5b where we plot the lasing frequency versus the particle reduced radius r/λ_{gain}. While in the Rayleigh regime the lasing emission follows the maximum of the gain, for $r > \lambda/2$ the emission starts to red-shift following the Mie resonances. The wavelength jumps correspond to the appearance of a more favourable resonance which pulls the lasing wavelength in the blue part of the gain region. The tunability range for the simulated system is highlighted by the area in grey and it is roughly 25 nm.

Figure 4.6.a is a zoom in of Figure 4.5.b and shows in detail the lasing frequency evolution around $r = \lambda$. The curve consists of three different continuous branches

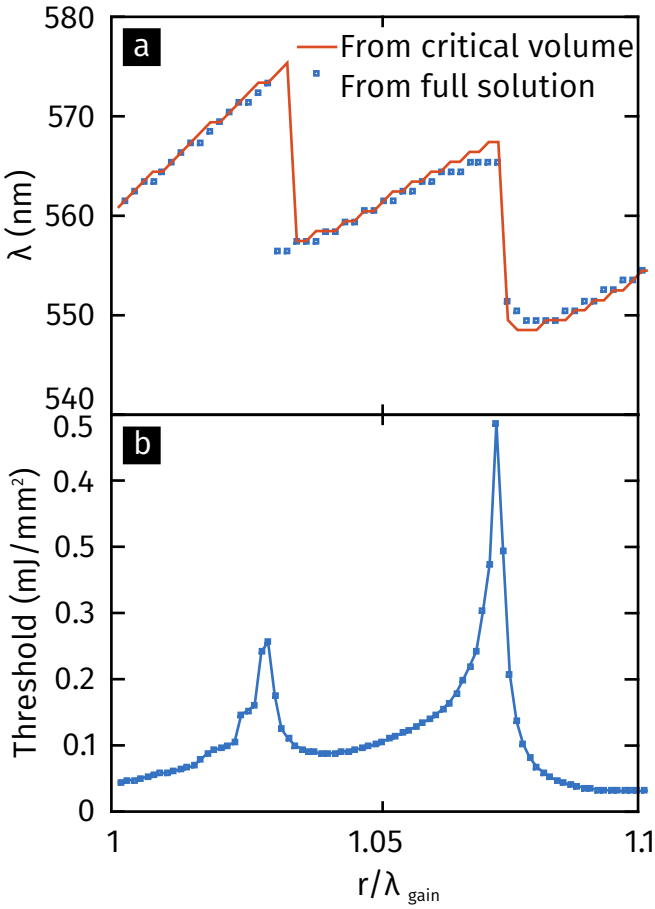

Figure 4.6: Details of the emission wavelength and lasing threshold. a Pulled by the Mie resonances, the lasing emission redshifts until the next Mie resonance enters the gain spectral region. This competition is shown by the tooth-saw profile. The numerical values (squares) are compared to the analytical prediction (orange line) obtained by the minimum of the critical length $L_{cr} = \pi\sqrt{\ell_t \ell_g/3}$. b The threshold, defined as the point of half emission narrowing, is quite constant in the tuning range apart close to the frequency jumps, when the competition between the two lasing peaks strongly increases it.

separated by two jumps. The numerical results of the model are compared to analytical diffusion calculations which predict lasing occurring at the wavelength which minimises the critical length L_{cr} [108, 109], the length above which the gain exceeds the losses. In a slab geometry, and under the approximation of uniform gain, the critical length is $L_{\mathrm{cr}} = \pi\sqrt{\ell_t l_g/3}$. The minimum of L_{cr} and the numerical results are in good agreement, with significant differences only close to the wavelength jumps where the simplified analytical model fails to account for the competition for the gain. We attribute this to the increased mode competition between two different Mie resonances. Mode competition is strong for particle sizes around $r = 571$ nm and 595.5 nm, and this is reflected by an increased threshold. For instance, the threshold does not always decreases monotonically when the lasing emission approaches λ_{gain}. For the other lasing frequencies the threshold is quite constant in the whole region of tunability with values around 0.1 mJ/mm^2. In addition, Figure 4.7 shows that for particles size $r = 571.9$ nm, corresponding to the lasing wavelength jump at $r/\lambda_{\mathrm{gain}} \simeq 1.03$ in Figure 4.6, the spectrum develops two competing peaks, one corresponding to the maximum of the gain and one corresponding to the minimum of the scattering length, of

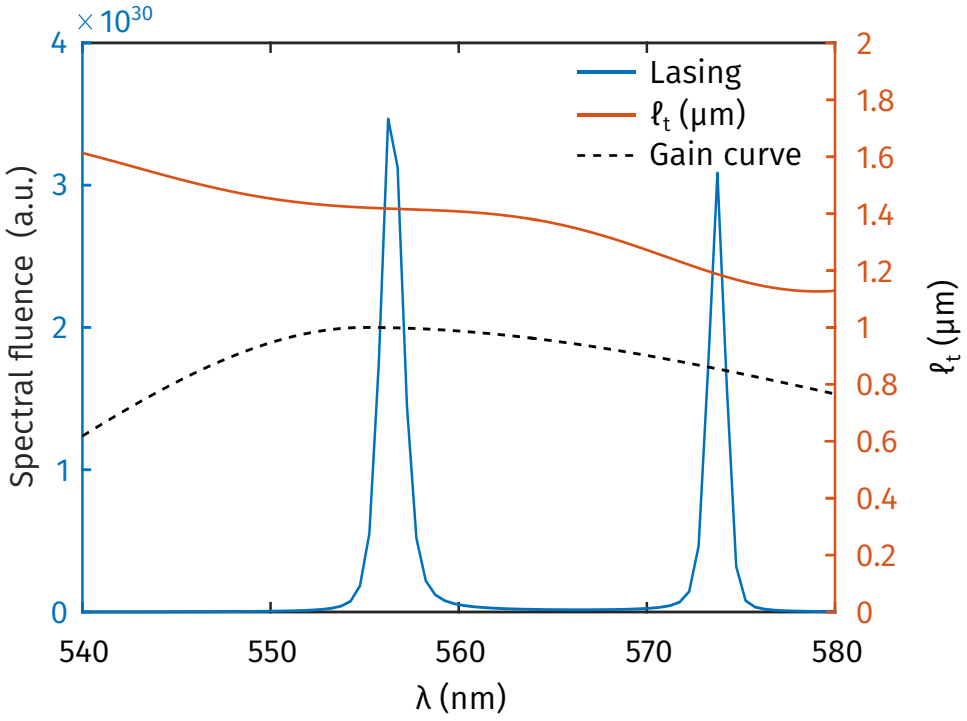

Figure 4.7: **Mode competition**. The emission spectrum for particle size $\{r = 571.9\}$ nm ($r/\lambda_{\mathrm{gain}} \simeq 1.03$, $P = 13.7$ mJ/mm^2) show two competing peaks, one corresponding to the maximum of the gain (black dashed line) and one corresponding to the minimum of the scattering length (orange line), of which one finally prevails for large enough pump energy.

which one finally prevails for large enough pump energy. A similar behaviour is produced at $r = 595.4$ nm.

4.5 How random lasing senses its environment

We have seen in the first part of this chapter how the the physical properties of the scattering system can control the lasing emission. While the range of tunability can be quite large, this has be obtained prior to fabrication by designing the scattering properties of the system, or by structurally changing the scattering properties as for instance in systems based on liquid crystals [131]. Diffusive random lasing is indeed quite robust to mechanical changes in the system, for instance due to sample deformation as a consequence implantation in an aqueous environment or temperature change, as well as small refractive index changes. This makes it appear not suitable for sensing purposes, when compared to the high sensitivity to subtle change of the refractive index that can be achieved by exploiting the resonant behaviour of structures, as it has been done for surface plasmons [132]. Nevertheless, in lasing systems the gain process which depends on the underlying molecular properties also plays a fundamental role. Therefore, molecular changes, such as the shift of the fluorescence emission in response to a target analyte, can be exploited for sensing purpose. Indeed, sensing using laser light is emerging as a promising field with prospect in sensitive biosensing [133, 134], a constantly advancing field of research, seeking for new sensitive and cost-effective detection devices. Unlike conventional fluorescence techniques which can have a low signal to noise ratio, the amplification of the signal inherent to a laser can overcome these limitations [135] supported by the transition from a broad spectrum (30–60 nm FWHM), characteristic of fluorescence, to an emission concentrated around a narrow emission line.

Random laser combines the non-linear character and amplification of the lasing response with the cavity-less nature of diffusive systems. Scattering is a universal robust phenomenon that can be engineered into a variety of hosting materials, including biocompatible ones such as silk (as shown in Section 4.7) or naturally present structures such as beetle scales [136], human tissue [137] and bone [138]; moreover, provided strong enough scattering and gain, the critical length $L_{\mathrm{cr}} \sim \sqrt{\ell_t \ell_g}$ can be achieved in systems as small as few μms [139], making random lasing appealing for bio-sensing purposes, especially for implantation into biological environment, owing to its stronger robustness to mechanical deformation of conventional cell-size lasers [140, 141].

Sensing with random lasers has been studied in terms of change in scattering strength [137, 142] and temperature [131], and discussed focusing on the effect of the change of the narrow line emission in coherent random lasing [106]; in contrast, we will focus on change in chemical environment for fixed scattering characteristics in diffusive random lasing [105]. Here we experimentally realise a proof of concept of random-lasing based biocompatible sensor and study numerically with the model discussed in Section 4.3 the dependence of the lasing on the molecular properties, identifying the parameters more suitable for sensing.

4.6 Random lasing sensing schemes

The principle of a random lasing sensing we investigate is based on the change of the "net gain". In Figure 4.8 we consider a reference system (1 mM rhodamine 6G, $\ell_t = 2$ μm, 50 μm slab) and model a change in the gain properties. We first study a reduction of the gain by a factor α, as resulting in realistic applications for example due to the quenching of molecules [143] by the formation of a non-fluorescent dimers or a the disruption of hydrogen bonds with solvent molecules [144]. Figure 4.8a shows the typical transition from the fluorescence emission at low pump fluence (purple line) to the lasing behaviour at larger pump (yellow line), characterised by a narrowing of the the emission spectra down to 5–10 nm which peaks at the maximum of the gain. Compared to fluorescence, the gain plays a fundamental role in controlling the lasing emission: Figure 4.8a shows the spectral change due to a reduction of the gain: while the fluorescence is unaffected (red line), a reduction of the gain by a factor ($\alpha = 0.15$) results in a massive change in terms of intensity and spectra of the lasing emission (blue line), as a larger pump intensity is necessary to achieve the lasing. This highlights a first aspect of the lasing based sensor, *i.e.* the sensitivity to molecular parameters usually not easily accessible from fluorescence based measurements.

Moreover, we address a possible spectral translation of the gain maximum, by a simple wavelength shift of the fluorescence emission. Figure 4.8b shows the effect of the spectral shift of the molecule emission properties, which can be up to 100 nm in specific dyes [145]. In this case, both fluorescence and lasing are expected to shift in a similar way, although the smaller bandwidth of the lasing peaks potentially allows larger signal to noise ratio and better sensitivity. The ability to expose otherwise hidden molecular properties combined with the larger spectral purity of the lasing emission is at the base of the sensing scheme we here propose.

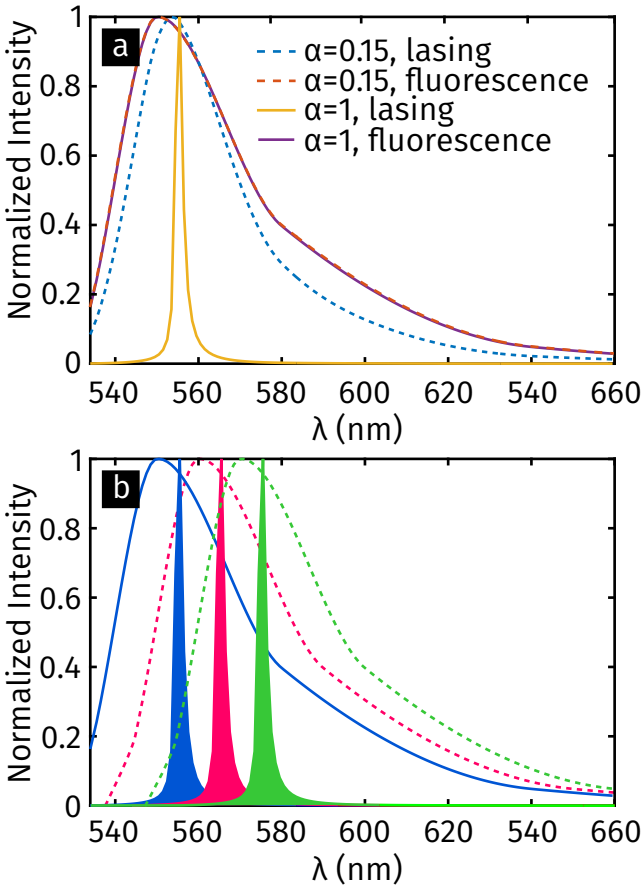

Figure 4.8: Random lasing sensing scheme. [a] Effect of a gain magnitude change: while the fluorescence spectra is not affected, in the lasing regime a large change from the lasing FWHM of $\sim 5-10$ nm (yellow line) to a broader emission spectrum with a FWHM of $\sim 30-40$ nm (blue line) close the the fluorescence emission (purple line) occurs. [b] Effect of a emission and gain spectral shift: the fluorescence (dashed lines) and lasing (solid filled lines) response shift similarly; the narrower FWHM of the lasing peaks allows for a better resolution and sensitivity.

4.7 Experimental realisation of a biocompatible random lasing based sensor

In this section, a proof of concept of a random lasing sensor is experimentally demonstrated in a system based on Bombyx Mori silk-fibroin, a flexible biopolimer obtained from the processing of silk worms cocoons with good optical properties [146]. The lasing system is fabricated as follow: an organic dye (rhodamine 6G) is dissolved in a solution of silk in water. A mixed direct photonic glass of polystyrene spheres (diameter $D = 1.24\,\mu$m) and silk is first grown, and then the inverse photonic glass structure is obtained by removing the sphere via selective chemical etching in toluene, as sketched in Figure 4.9a. This produce

planar films with a thickness of $\sim 100\,\mu$m, a transport scattering length $\ell_t \sim 4\,\mu$m in dry conditions, which increases to $\sim 14\,\mu$m when in an aqueous environment due to reduction of the contrast in the index of refraction. An SEM image of the sample is hown in Figure 4.9b.

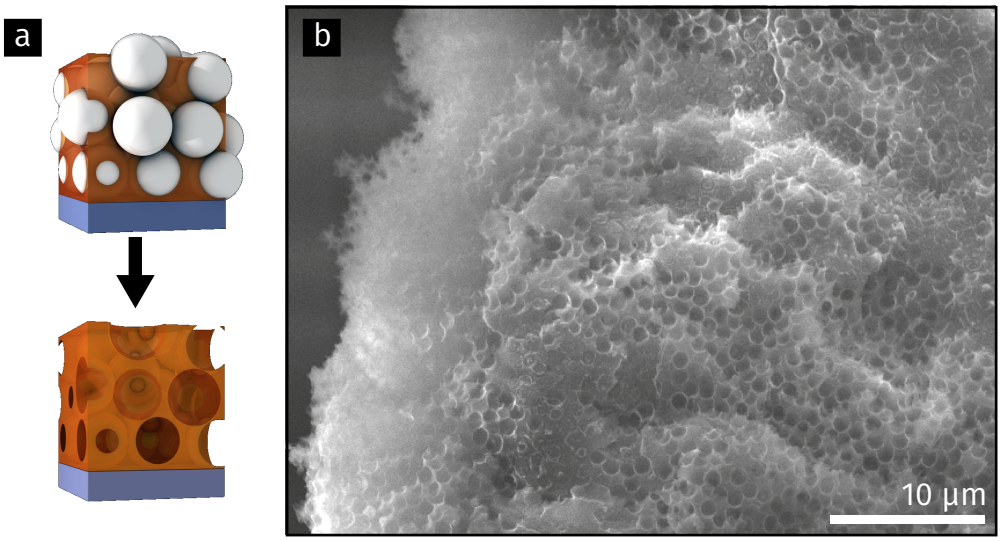

Figure 4.9: SEM picture of silk random lasing. a Sketch of the fabrication process from the direct to the inverse structure. b A scanning electron microscopy image of the final structure (Courtesy of Soraya Caixeiro).

A spot with a diameter of ~ 1 mm is pumped with single pulses of a 532 nm laser, with a pulse width of 6 ns. Figure 4.10 reports the experimental lasing emission characteristics at increasing pump power. The crossover from fluorescent to lasing emission is observed with a threshold $T_{\text{exp}} = 70\,\mu\text{J/mm}^2$. The change of emission regime is marked by both a spectral narrowing (red circles) and an increase of emission at the lasing wavelength (blue circles). The emission spectra are smooth curves as one would expect for diffusive or incoherent random lasing with non-resonant feedback. The data can be therefore modelled appropriately with the diffusive random lasing model discussed in this chapter. The theoretical predictions are shown by the lines in Figure 4.10. The molecular parameters are taken from literature[128], while the transport scattering length was measured with transmission experiments ($\tau = 2.5\,$ns, $\ell_s = 4\,\mu$m). The theoretical curve is normalised by the detected signal at low power, which is only fluorescence, showing good agreement with the experiment. The theoretical line-width above threshold is underestimated as it is limited only by gain saturation. Instead, the threshold position is obtained with a remarkable precision, $T_{\text{th}} = 50\ \mu\text{J/mm}^2$ which compares well with the experimental value $T_{\text{exp}} = 70\ \mu\text{J/mm}^2$.

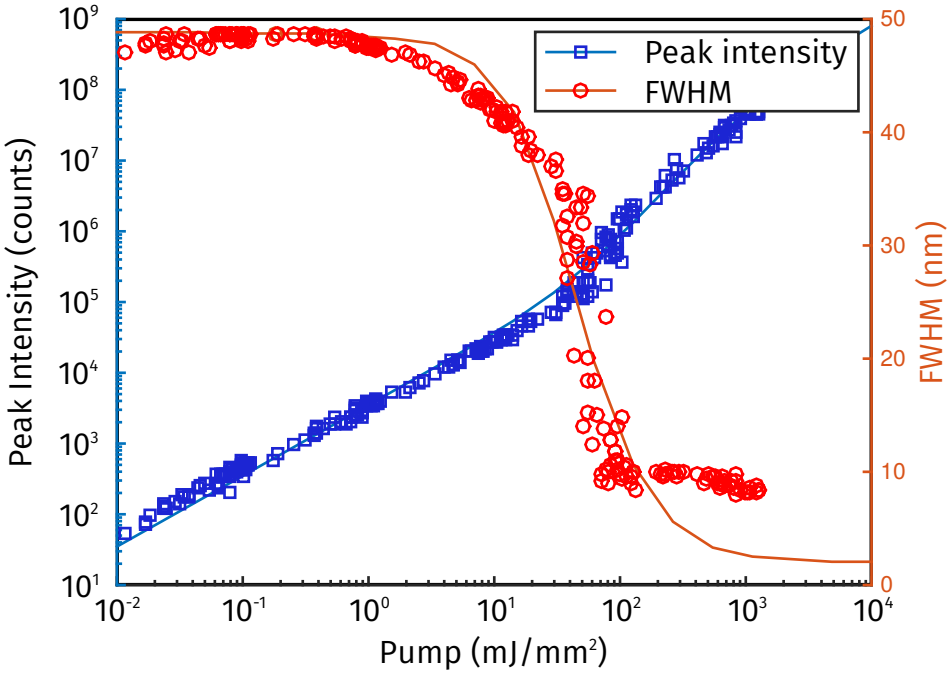

Figure 4.10: Silk random lasing - theory and experiment. The empty symbols correspond to the experimental data while the lines are the theoretical calculations for a slab thickness 100 μm, $\ell_t = 4\mu$m and $\tau = 2.5$ ns. The experimental fluorescent spectrum of our dye was used together with typical values of rhodamine 6G absorption and stimulated emission cross-section . The model gives a theoretical threshold $T_{\text{th}} = 50\,\mu\text{J/mm}^2$which compares well with the experimental value $T_{\text{exp}} = 70\,\mu\text{J/mm}^2$. The theoretical line-width above threshold is underestimated, as it is limited only by gain saturation.

A proof of principle of pH sensing is provided by operating the system in an aqueous solutions. The emission characteristic of the sample immersed in aqueous solution is measured at a fixed pump power while the pH is modified by changing the concentration of NaOH. The results are shown in Figure 4.11.

When pumped in the lasing regime ($P = 840\ \mu\text{K/mm}^2$) the emission is strongly affected affected by the pH change (Figure 4.11a). This is also visible in Figure 4.11b, showing that the lasing is suppress at around pH$\sim$ 13, corresponding to a large decrease in the peak emission intensity and broadening of the emission bandwidth. On the other hand when pumped in the fluorescence regime ($P = 8\ \mu\text{J/mm}^2$) the emission spectrum almost does not change for different values of pH (Figure 4.11c), while the emission intensity change is less prominent than in the lasing case (Figure 4.11d). Therefore, the lasing process amplifies the variation of the molecular properties at different pH conditions. Moreover, the lasing can be recovered by restoring the pH. These experimental results could be explained assuming a change of the gain available in the scattering medium, due

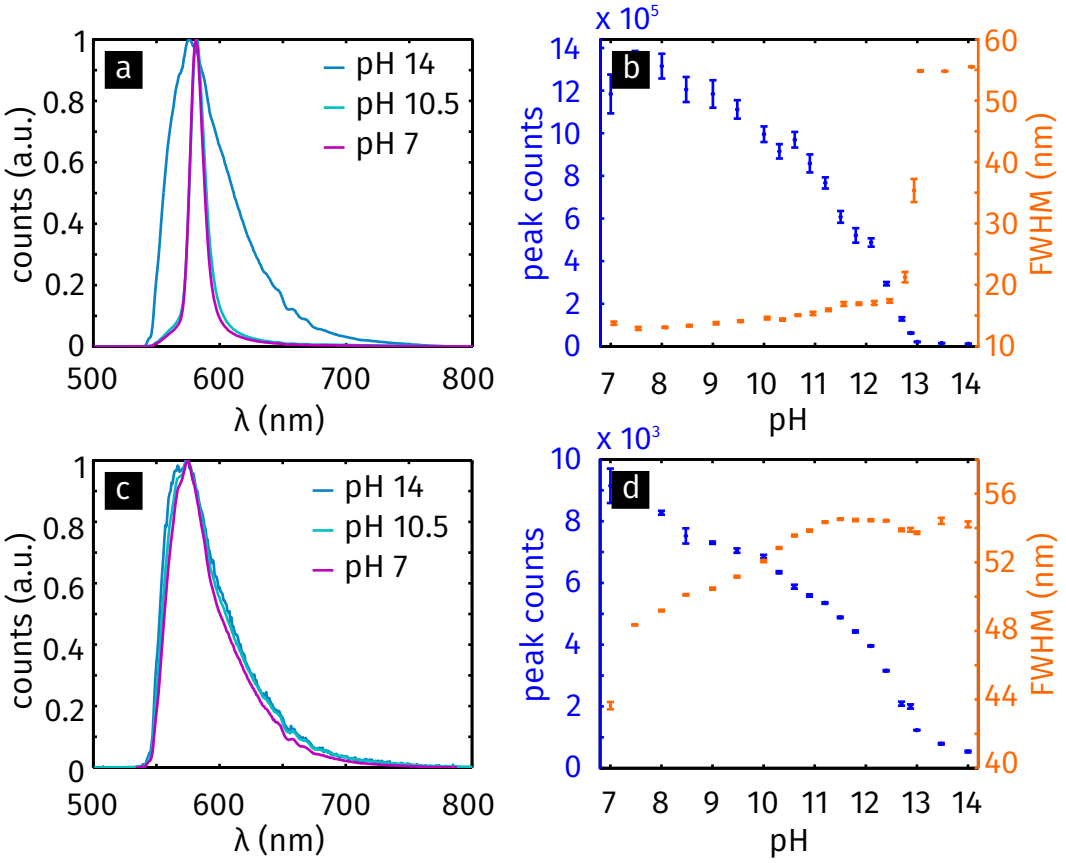

Figure 4.11: Experimental proof of principle of the random lasing scheme. a A silk based random lasing system is pumped at high intensity ($P = 840\,\mu\text{J/mm}^2$): the emission characteristics as a function of the pH of the solution, showing suppression of the lasing at large pH values; b spectra comparison for two values of pH, highlighting the transition from lasing to non lasing. c The same sample is pumped with lower intensity ($P = 8\,\mu\text{J/mm}^2$): a reduction of the intensity emitted is visible in the emission characteristics; d in this case the spectral properties are roughly constant at all values of pH.

to reduced amplification or increased absorption. Instead, a structural change of the silk structure, i.e. a change of the scattering properties has been rule out by direct SEM measurements. In order to understand how the different molecular parameters affect the lasing emission and how they can be exploited for sensing, in the next section we investigate in details their different roles.

4.8 Random lasing sensing analysis

As introduced in Section 4.6, the "net gain" available in the system results from the balance between the stimulated emission process and the loss channels, *i.e.* fluorescence, non-radiative decay, and absorption, dominates the lasing process.

In order to understand the different contributions and how these can be exploited for sensing, we first consider a simplified case of Equations (4.3–4.5) by neglecting the spatial and spectral dependence and considering the stationary case:

$$\sigma_a P[N-N_1]v-\sigma_e I N_1 v-\frac{N_1}{\Phi\tau_r} = 0 \tag{4.6}$$

$$\sigma_e I N_1 v+\beta\frac{N_1}{\tau_r}-\frac{I}{\tau_c} = 0 \tag{4.7}$$

Here I is the light intensity in the lasing band and and the pump intensity is described by P. A loss term dependent on the the Thouless time τ_c, i.e the average time a photon stays inside the samples which depends on the scattering length and samples size ($\tau_c \sim L^2/\ell_t$), has been added in place of losses at the boundary conditions, and the spectral properties are summarised in the β factor[1], describing the fraction of the fluorescence emission in the lasing mode. In Equations (4.3–4.5) we express separately the radiative decay rate τ_r and the quantum efficiency which we model by introducing a non radiative decay rate$\Gamma_{nr} = 1/\tau_{nr}$, as:

$$\Phi = \frac{\Gamma_r}{\Gamma_r+\Gamma_{nr}} = \frac{\tau_r}{\tau}. \tag{4.8}$$

Solving Equations (4.6–4.7) lead to two asymptotic behaviours. A regime where the emission intensity is dominated by fluorescence (I_F) at low pump intensity ($\sigma_e I N_1 v \ll N_1/\tau$) and below fluorescence saturation ($\tau_r\Phi\sigma_a P \ll 1$):

$$I_F(P) \propto \sigma_a N P \tau_c \beta \Phi, \tag{4.9}$$

and a regime dominated by lasing emission (I_l) at hight pump intensity ($\sigma_e I N_1 v \gg N_1/\tau$):

$$I_L(P) \propto \frac{-1+\sigma_a P\tau_r\Phi(N\tau_c\sigma_e v-1)}{v\sigma_e\tau_r\Phi}. \tag{4.10}$$

As the sensing mechanism is based on the transition between the fluorescence and lasing behaviour, we consider the threshold T which is is the pump intensity marking the onset of the lasing process. Different threshold definitions are often used, but they are typically proportional to each others. An operative definition of the threshold in experimental conditions is the pump power corresponding to half narrowing of the emission spectra, which can be measured by measuring the spectrum of the emission at different pump. For this simplified treatment that does not include the spectral properties instead the threshold T can be extrapolated

[1]Not to be confused with the β factor introduced in Chapter 2

from the intercept of the lasing trend ($I_L(T)=0$): the relation between the systems properties and the threshold is therefore given by the following trend:

$$T \simeq [(N\tau_c v\sigma_e - 1)\tau_r \Phi \sigma_a]^{-1}. \tag{4.11}$$

The change of the threshold of the lasing process is the key element for a RL sensing scheme. As the threshold moves, different measurable parameters such as the light intensity and FWHM of the emission can be monitores to quantify the change. We will now consider in details the effect of the different molecular parameters, *i.e.* the stimulated emission cross section σ_e, quantum efficiency Φ, lifetime of the excited states τ_r, which all appear in Equation (4.11). We solve numerically the complete systems to describe realistic experimental conditions, and we compare with existing dyes properties. Although these parameters are typically linked in real dyes, we consider them independently to highlight their role.

Gain (stimulated emission cross section)

Among all the parameters we first consider the direct role of the gain, as already qualitatively discussed in Section 4.6. The gain depends on the density of gain molecules and their properties, and on the pump intensity bringing the system to population inversion conditions. From the microscopic point of view, a change in gain can be modelled as a modification of the stimulated emission cross section σ_e. We decrease σ_e starting from the reference system previously discussed (1 mM rhodamine 6G, $\ell_t = 2$ μm, 50 μm slab). Figure 4.12a shows the threshold dependence as a function of σ_e/σ_0. For $\sigma_e/\sigma_0 \simeq 0.2$ no lasing occurs regardless of the intensity of the pump. In fact, a minimum amount of gain is necessary to overcome the losses at the surface of the sample ($N_0 v\sigma_e \lesssim \tau_c$) and due to absorption in the medium. Larger systems (which have larger Thouless time) can reach the critical length with smaller gain.

Figure 4.12b reports the emission intensity response as a function of the pump intensity. At low pump power (fluorescence regime) the response is linear and similar for all gain values. Instead, when the system is operated above the critical length the sudden change in regime between fluorescence and lasing result in a large sensitivity to the gain value. The large variation in the intensity response with a sub-linear behaviour for low σ_e/σ_0 values is due to the loss of the pump intensity, as the fluorescence is not fast enough to allow the dye molecules to absorb it before it escapes the system.

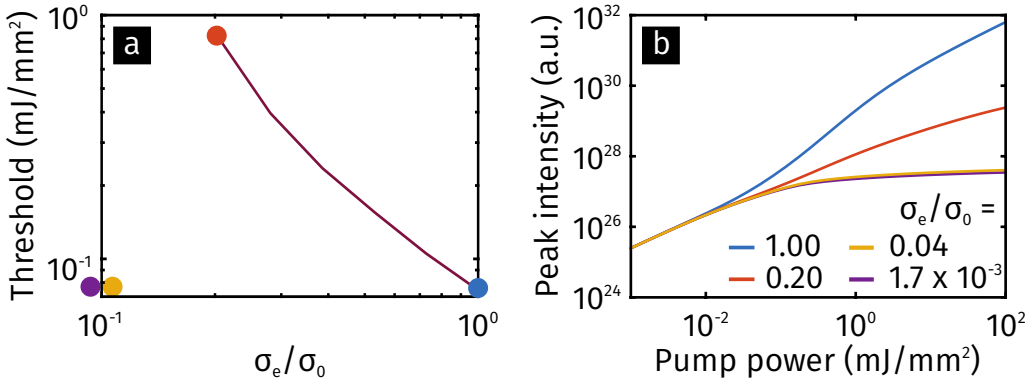

Figure 4.12: Sensing of the gain. a The threshold increases decreasing gain compare to the reference value, until the lasing is stopped at $\sigma_e/\sigma_0 \simeq 0.2$ for the sample size under examination. b The peak intensity response showing that instead of a lasing regime with higher intensity a saturation of the emission occurs due to the saturation of the fluorescence (pump power is lost). The corresponding position of the threshold are indicated by the coloured circles in panel a.

In order to investigate an ideal sensing scheme, we consider the variation of two easily measurable quantities, the peak intensity and the width of the emitted spectra, upon change of the gain while keeping the pump intensity at a constant value, as reported in Figure 4.13. Each line in Figure 4.13a corresponds to the intensity response at a different pump intensity, *i.e.* to a vertical cross section in Figure 4.12b. A larger slope of such curves corresponds to larger sensitivity. The lower curves, corresponding to lower pump intensity in the fluorescence regime, show no sensitivity to the gain variation. Instead, For increasing pump intensities the system becomes gradually more sensitive. The same analysis is performed for the emission spectral width. The FWHM is reported in Figure 4.13b, showing similar behaviour with increasing sensitivity as the pump power is increased. In particular, for the choice of the sample parameters, a region of increased sensitivity with a non-linear response appears at around $\sigma_e/\sigma_0 \simeq 0.2$, that is when the lasing is suppressed by the lack of net gain (a more detailed analysis of the sensitivity is presented at the end of this section). Different parameter configurations, in particular the samples dimension, can shift this region. For instance, smaller samples result in a transition at large values of σ_e/σ_0, which also becomes more prominent.

Quantum efficiency

The quantum efficiency (or quantum yield) Φ is the ratio between the light radiated and light absorbed, i.e is a measure of the efficiency in re-emitting a photon

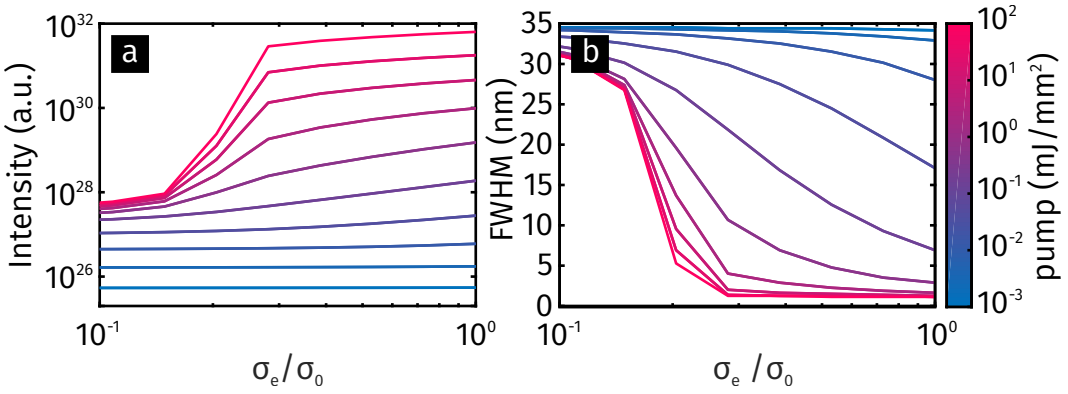

Figure 4.13: Sensing by gain response. a Output intensity response as a function of the gain (σ_e/σ_0) at different pump power as indicated by the colorbar. b The corresponding output spectra width (FWHM) response.

rather than dissipating the photon energy in non-radiative processes. Typical lasing dyes have $\Phi \simeq 1$, and variations are found to be typical in the range $\sim 10\%$ [147] for standard laser dyes in different solvents; however when considering engineered dyes 100 fold decrease of the quantum efficiency has been observed [145].

Figure 4.14a shows the threshold behaviour for a reference system (0.1 mM rhodamine 6G, $\ell_t = 2$ μm, 50 μm slab, *i.e.* the system of the previous section but with reduced gain molecules concentration in order to highlight the lasing transition); the hyperbolic behaviour of Equation (4.11) is reproduced, with the threshold diverging when approaching $\Phi = 0$. Unlike the previous case the lasing

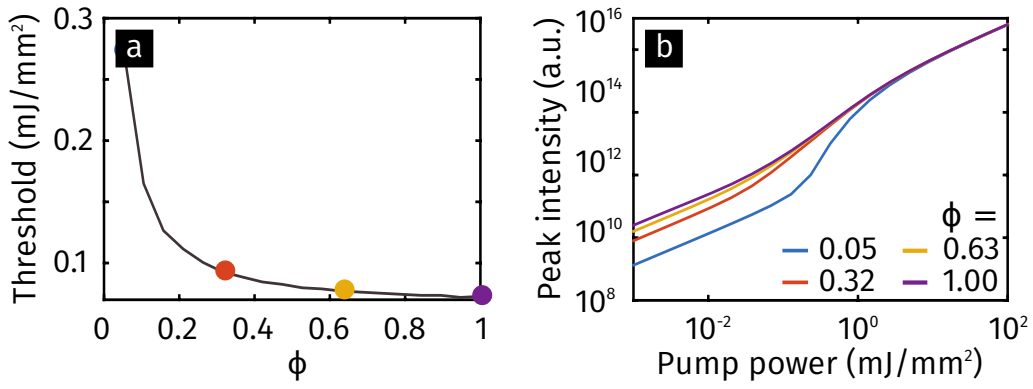

Figure 4.14: Sensing of the quantum efficiency a Lasing threshold change for different quantum efficiencies. The threshold (T) increases five-fold for $\Phi \sim 0.05$. The relative sensitivity is in the range b Intensity response for different quantum efficiencies: while the fluorescence response ($P < 10^{-1}$ mJ/mm^2) is strongly affected by the quantum efficiency change, in the lasing regime ($P > 1$ mJ/mm^2) is mostly unaffected. The corresponding position of the threshold are indicated by the coloured circles in panel a.

process is never suppressed, although it becomes realistically unachievable due to the high pump intensity required; in fact, as shown in Figure 4.14b where the intensity evolution at different pump power for few different Φ values is plotted, while in the fluorescence regime ($P < 10^{-1}$ mJ/mm^2) the intensity is proportional to Φ, in the lasing regime instead ($P > 1$ mJ/mm^2), even if the onset of lasing is shifted to higher pump fluence, the emission behaviour is not affected as the the non-radiative channel decay rate becomes negligible compared to the stimulated emission process.

At first sight, working in the lasing regime appears to be detrimental. However, an increase in sensitivity when compared to fluorescence can be obtained in the transition from the fluorescence to the lasing regime. This is shown in Figure 4.15a where the intensity response as a function of Φ are shown for different pump intensity. In fact, if $\Phi \simeq 1$, the sensitivity is maximized by working in the

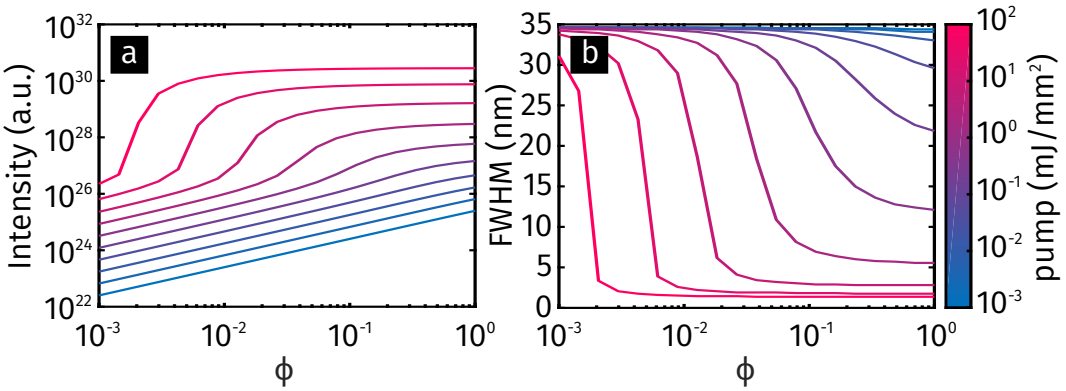

Figure 4.15: Sensing by quantum efficiency response. [a] Output intensity response as a function of quantum efficiency (Φ) at different pump power indicated by the colourbar. [b] The corresponding output spectra width (FWHM) response.

fluorescence regime (lower curves in Figure 4.15a, where the intensity is proportional to Φ) while the response in the lasing regime is flat. Instead, if $\Phi \lesssim 0.1$, the fluorescence-lasing transition becomes more abrupt, as the molecules effectively act as absorption in the fluorescence regime and as gain in the lasing regime, and the change of peak intensity from fluorescent to lasing is more prominent with a increase by a factor $1/\Phi$. This corresponds to the increase in the slope of the curves in the upper part of Figure 4.15a. In the same region with increased intensity sensitivity, the FWHM of the spectrum reported in Figure4.15b also shows the largest and steepest variation.

Lifetime of the excited state

The lifetime of the excited state τ is an important parameter of fluorescence dynamics, which can change upon binding of a fluorescence molecule to targets analytes [144]. While this might be linked to the change in quantum efficiency as a new non-radiative channel might be introduced in the system, for the sake of clarity we analyse the sensing behaviour assuming $\Phi = 1$, *i.e.* $\tau = \tau_r$.

The lifetime τ is typically measured with dedicated and fast (ps) electronics in a confocal microscope. According to Equation (4.11), a dependence of the lasing threshold is also expected, since long fluorescence lifetimes help reaching the population inversion with lower pumps. Figure 4.16a shows the threshold behaviour for our usual reference system (1 mM rhodamine 6G, $\ell_t = 2$ μm, 50 μm slab), which is roughly inversely proportional to the lifetime ($T \sim \tau^{-1}$) up to $\tau \sim$ 10 ns, when the finite size of the system starts becoming important. The lifetime of

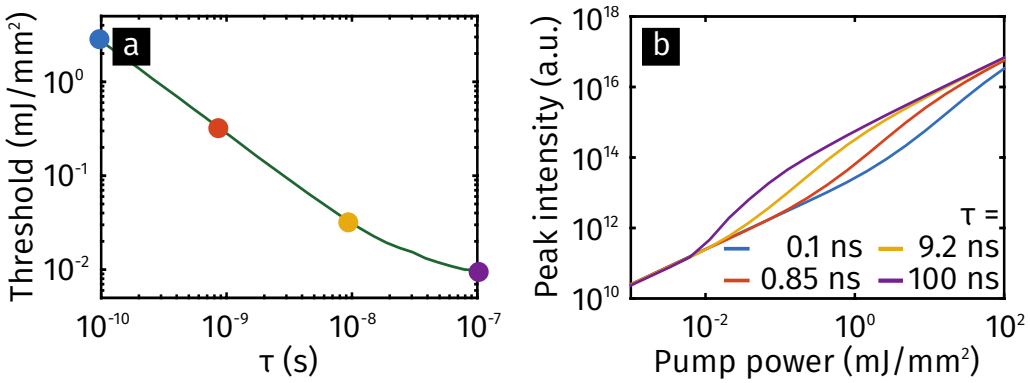

Figure 4.16: Sensing of the decay rate. a Lasing threshold change for different decay rates. The threshold decreases with a power law for increasing decay rates ($T \sim \tau^{-1}$), until a saturation value is reached for $\tau > 100$ ns. b The intensity response shifts accordingly with the increase of the decay rate. The corresponding position of the threshold are indicated by the coloured circles in panel a.

the excited state has a negligible effect on the fluorescence intensity (Figure 4.17a, $P < 10^{-2}$ mJ/mm^2); the lasing process instead exposes τ with an easily measurable quantity without the need of dedicated electronics for $P > 10^{-2}$ mJ/mm^2.

Figure 4.17 shows the intensity and FWHM variation as a function of τ for different pump intensities. Also in In this case the response is flat at low pump intensities, while at larger values a fluorescence-lasing transition is found, occurring smoothly in a large wide τ range (roughly one order of magnitude), and positioned at higher pump intensity for smaller lifetime. Similarly, the FWHM of the spectrum evolves slowly narrowing at increasing τ in the corresponding area.

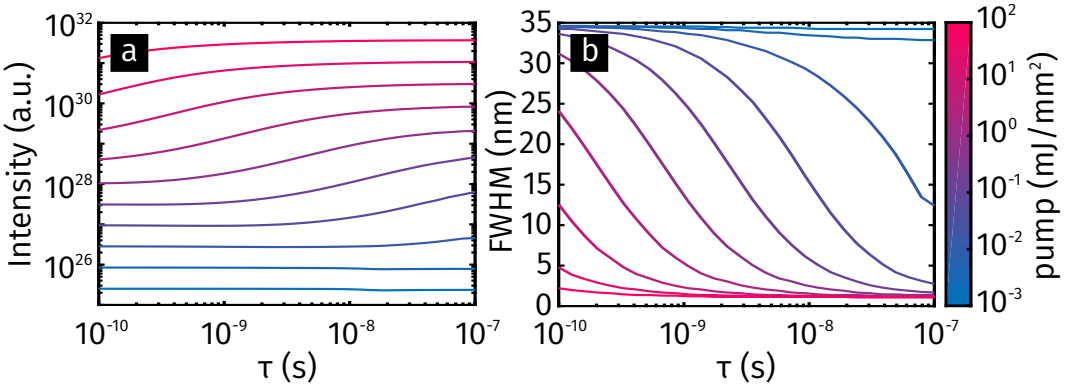

Figure 4.17: Sensing by decay rate response. a Output intensity response as a function of the lifetime (τ) at different pump power indicated by the colourbar. b The corresponding output spectra width (FWHM) response.

4.9 Sensitivity analysis

To summarize the results of the previous section, we compare now the sensitivity sensitivity obtained from the different parameters. In order to highlight the non-linear response of the lasing process, we choose the peak intensity (I) relative sensitivity as figure of merit:

$$S_\alpha = \frac{dI/I}{d\alpha/\alpha},$$

where α is one of the parameters examined: Φ, τ, σ_e. The linear response typical of the fluorescence regime would give $S_\alpha \leq 1$. The relative sensitivity is reported in Figure 4.18 for different working pump intensities with colormaps highlighting the regions of larger sensitivity.

Depending on the value of the sensing parameter a different pump power is required to achieve maximum sensitivity. In all cases the maximum relative sensitivity is obtained around the threshold transition which is marked by white dashed lines. This corresponds to the intermediate non-linear regime between two linear region. At low pump fluorescence is either non-sensitive for lifetime and gain (S_τ, $S_{\sigma_e} \ll 1$) or provides a linear response in the case of the quantum efficiency ($S_\Phi \simeq 1$). At large pump intensities the lasing response becomes linear due to gain saturation, reducing the sensitivity in all cases. At intermediate pump intensities instead, in the case of lifetime an increased sensitivity is obtained ($S_\tau \simeq 5$) in a wide area around the lasing threshold. In the case of both Φ and σ_e large relative sensitivities ($S_\Phi \simeq 600$, $S_{\sigma_e} \simeq 300$) — two order of magnitude higher than fluorescence — in narrow parameter regions are obtained. This analysis show that the sample properties, such as the scattering length, sample size or density of gain molecules have to be designed to match the most sensitive region of the dye, as

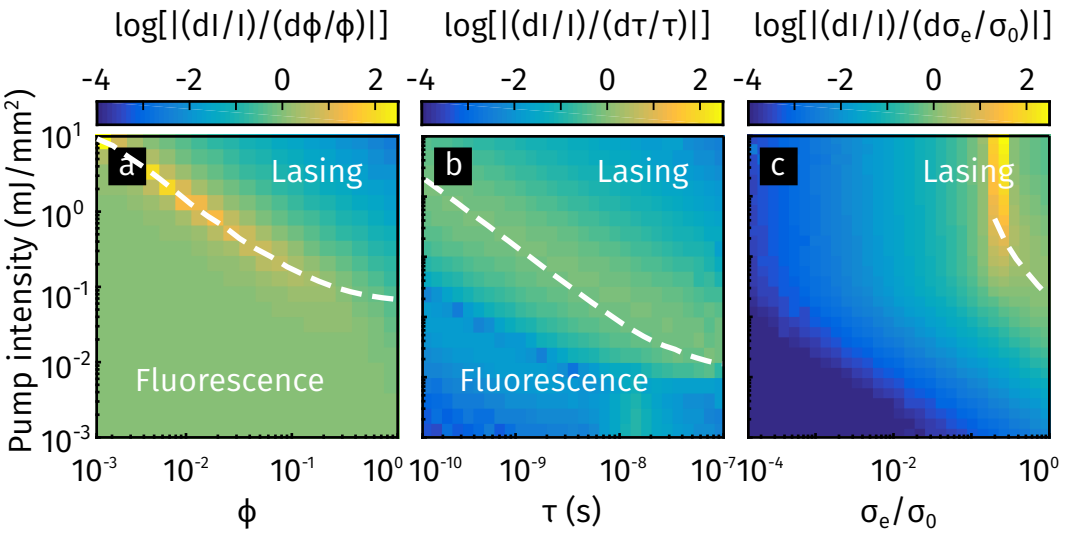

Figure 4.18: **Relative sensitivity**. The peak intensity relative sensitivity is shown with a logarithmic colourmap for the parameters under consideration at different pump powers. [a] Quantum efficiency (Φ), [b] excited state lifetime (τ), [c] stimulated emission cross section (σ_e). The white dashed line is the lasing threshold. In all cases the larger relative sensitivity is found in the non-linear regime around the lasing transition.

well as to keep the working power at reasonable values.

This sensing technique, that we proved experimentally for NaOH in Section 4.7, could be applied to relevant biomolecules, in principle with the same broad range of targets as in fluorescence sensing, but with the advantage of increased sensitivity due to the non-linear lasing process.

4.10 Conclusions

In conclusion, a dispersive diffusive gain model is capable to simulate random lasing action in realistic conditions. In particular, for resonant scattering we calculated a 25 nm emission tuning range, with minimal threshold increase. The dispersive model does not require any assumption on the β parameter and can predict mode competition and a non-trivial threshold dependence. Beyond what is expected by diffusive monochromatic models, the highest threshold is found when the competition between the lasing modes is strongest and not when the lasing wavelength is furthest from the maximum of the gain curve. As a further extension, the model can include arbitrary absorption curves and dispersion also for the energy velocity, and can be extended to the full three-dimensional case at the expense of increased computing time.

The same model was used to investigate the potential sensing application of a system based on random lasing, motivated by the possibility to fabricate fully biocompatible devices. We considered few important fluorescence parameters already used in fluorescence-based sensors. We showed that by working in the lasing regime additional properties such as the FWHM can be exploited for sensing, and that the change of otherwise not directly observable quantities can be recovered, revealing the underlying biochemical process. A much higher relative sensitivity (> 100-fold) is achieved when crossing the lasing threshold, exploiting the non-linear behaviour of the lasing process: therefore the key element is to design and operate the systems close to its critical volume, where upon sensing of an analyte the system can change from the lasing to the non lasing regime or vice-versa. Surprisingly, the complexity of the disordered medium leads to a great simplicity of the overall device. In fact, we showed that random lasing can be obtained from biocompatible constituents, and we forecast that random lasing devices could eventually be integrated in biological tissues or on-skin for bioengineering applications with the potential to provide a new tool to image and sense biological properties inside human body.

Conclusions and outlook

The goal of this thesis has been to study nanostructured systems which have potential as building blocks to realise complex photonic networks capable of controlling light-matter interaction, directing individual photons, and bringing collective emission phenomena such as lasing; we pursued applications such as biosensing via biocompatible photonic random lasers, as well as at future implementations of nanoscale quantum optics.

Achieving coupling and long distance transport of light emitted by nanoscopic sources, end eventually coupling between multiple emitters, is challenging task, owing to the intrinsic multiscale nature of the problem: the interaction between the electronic transition at the sub-nanometre length-scale and the the electromagnetic radiation at visible wavelength (~micron) is typically inefficient. The emitted photons need to be transported at long distances ($\gg \lambda$). Furthermore, any realistic architecture is required to have the potential of scalability up to the macroscopic world of extended complex devices. This requires the simultaneous engineering of both the near-field and far-field.

In the first chapter we developed a single-photon architecture — single emitter in a nanowaveguide — combining large coupling and propagation length, suitable for room temperature operation due to the broadband nature of these structures, and competitive with current schemes such as plasmonic systems. The results discussed here are the building block for the realisation of interconnected systems. The fabrication and characterisation of simple connected designs, would be the natural evolution to approach the study of networks-like architectures. In fact, owing to their simple design and fabrication process, these nanofibres are a promising tool for the implementation of extended geometries of increasing complexity, where one or more sources can be embedded, although without a precise control of the design. Therefore, a nanoscale network is particularly suitable for the study the effect of those properties which require the statistical study in multiple realisations, such as the degree of connectivity, in open and closed topologies; it is moreover a platform for the initial investigation and prototyping of architectures which might be eventually implemented with more conventional lithographic

methods. Beside studies of single emitters, these nanofibres are also suitable of transport studies, for instance investigating scattering and diffusion in network-like geometries, where topologies with multiple input and output channels could be controlled. Random lasing in such systems could also help to highlight the relation between the network topology and the optical properties.

However, this purely dielectric architecture does not provides strong light-matter interaction enhancement, due to the weakly sub-wavelength mode squeezing of the nanofibres. In the second chapter we focused on plasmonic structures in order to study systems allowing squeezing of light to deeply sub-wavelength hotspots, which are therefore appealing for enhance light-matter interaction. Plasmonic systems such as nano-antennas like structures, allow to efficiently control the near-field, which is ideal when it concerns controlling *one* emitter, but poses major limitations to long transport and scalability due their intrinsic metal losses. Instead, here we considered extended systems presenting electromagnetic hotsposts as well as long-range correlations; we tried to reproduce in a controlled way the modal properties of similar self-assembled systems, to explore the opportunity to exploit the localisation properties of the electromagnetic modes for the coupling of emitters. We confirmed the importance of the percolation transition in self-assembled structures, while the lithographic structures, although showing a response evolving with the percolation level, did not show marked behaviour at the percolation transition. This suggests that the observed LDOS fluctuations in the self-assembled networks are driven by local properties such as the formation of nanogaps, which cannot be obtained with lithographic techniques. However, it is still unclear whether long-range characteristics can also play a role in the control of the emission of light. Further development of this research would include exploring self-assembly techniques with more controlled designs in order to focus on the smaller features, while lithography could be employed to investigate a connected architectures, exploiting propagating plasmons rather than individual coupled antenna resonances.

It is natural to consider pursuing an hybrid dielectric-plasmonic approach to combine the benefits of the both architectures. The flexibility of the electrospinning fabrication process of the nanofibres discussed in chapter 1 would allow the integration of metallic nano-structures. For examples, gold nanoantennas with coupled emitters could be integrated in the nanofibre core, combining strong light-matter interaction and large coupling and transport towards more far-fetched goals such as enhancing the energy transfer between remote emitters. Another effective approach would be to realise hybrid metallic-dielectric structures: coating

the nanofibres with metal is a viable possibility.

In the last chapter we approached the problem of dealing with more than one emitter starting from diffusive lasing systems. This is admittedly an extreme case of the class of systems we decided to investigate, *i.e.* a randomised system where many modes participate to the lasing behaviour in an averaged fashion. However, this allowed us to numerically model macroscopic systems, quantifying the change in the emission due to modification of the sample parameters. We studied and experimentally demonstrate a promising sensing application, based on the variation of threshold of the lasing system due a change in the chemical environment affecting the gain molecules, a scheme that can provide increased performance when compared to fluorescence. In particular, the silk-based random lasing biosensor we proposed is made by all natural processes and materials. Therefore, it is an environmentally friendly product, potentially cheap and easily mass-produced, that can be at the basis of future silk-biophotonic applications in technology and medicine. This would require the investigation of specific sensing dyes, drawing inspiration from available fluorescence compounds, studying their compatibility with silk, and the optimization of their operation, with the aid of the numerical model described here. Due to the flexibility of the design, the same architecture could be studied in alternative biocompatible hosting materials. Moreover, it is crucial to improve the miniaturization of these lasing systems, for example exploring small spherical systems which can be obtained by self-assembly techniques: achieving lasing systems of size smaller than tens of micrometers would allow for instance the integration within living cells.

□

Bibliography

[1] Koenderink, A. F., Alu, A. & Polman, A. Nanophotonics: Shrinking light-based technology. *Science* **348**, 516–521 (2015).

[2] Kraus, H. *et al.* Magnetic field and temperature sensing with atomic-scale spin defects in silicon carbide. *Scientific reports* **4**, 5303 (2014).

[3] Aharonovich, I. *et al.* Diamond-based single-photon emitters. *Reports on Progress in Physics* **74**, 076501 (2011).

[4] Michler, P., Kiraz, A., Becher, C. & Schoenfeld, W. V. A Quantum Dot Single-Photon Turnstile Device (1999).

[5] Basché, T., Moerner, W. E., Orrit, M. & Talon, H. Photon antibunching in the fluorescence of a single dye molecule trapped in a solid. *Physical Review Letters* **69**, 1516–1519 (1992).

[6] Hennrich, M., Legero, T., Kuhn, A. & Rempe, G. Photon statistics of a non-stationary periodically driven single-photon source. *New Journal of Physics* **6**, 86–86 (2004).

[7] Maurer, C., Becher, C., Russo, C., Eschner, J. & Blatt, R. A single-photon source based on a single Ca^+ ion. *New Journal of Physics* **6**, 94–94 (2004).

[8] Eisaman, M. D., Fan, J., Migdall, A. & Polyakov, S. V. Invited Review Article: Single-photon sources and detectors. *Review of Scientific Instruments* **82**, 071101 (2011).

[9] Kok, P. *et al.* Linear optical quantum computing with photonic qubits. *Reviews of Modern Physics* **79**, 135–174 (2007).

[10] Chang, D. E., Vuletić, V. & Lukin, M. D. Quantum nonlinear opticsÂ - Â photon by photon. *Nat. Photonics* **8**, 685–694 (2014).

[11] Chang, D. E., Sørensen, A. S., Demler, E. a. & Lukin, M. D. A single-photon transistor using nanoscale surface plasmons. *Nat. Phys.* **3**, 807–812 (2007).

[12] Hwang, J. *et al.* A single-molecule optical transistor. *Nature* **460**, 76–80 (2009).

[13] Kimble, H. J. The quantum internet. *Nature* **453**, 1023–1030 (2008).

[14] Cirac, J. I., Zoller, P., Kimble, H. J. & Mabuchi, H. Quantum State Transfer and Entanglement Distribution among Distant Nodes in a Quantum Network. *Physical Review Letters* **78**, 3221–3224 (1997).

[15] Walther, H., Varcoe, B. T. H., Englert, B.-g. & Becker, T. Cavity quantum electrodynamics. *Reports on Progress in Physics* **69**, 1325–1382 (2006).

[16] Bransden, B. & Joachain, C. *Physics of Atoms and Molecules.* Pearson Education (Prentice Hall, 2003).

[17] Gaponenko, S. *Introduction to Nanophotonics* (Cambridge University Press, 2010).

[18] Loudon, R. *The Quantum Theory of Light* (OUP Oxford, 2000).

[19] Taminiau, T. H., Karaveli, S., van Hulst, N. F. & Zia, R. Quantifying the magnetic nature of light emission. *Nature communications* **3**, 979 (2012).

[20] Novotny, L. & Hecht, B. *Principles of Nano-Optics.* Principles of Nano-optics (Cambridge University Press, 2012).

[21] Carminati, R. *et al.* Electromagnetic density of states in complex plasmonic systems. *Surface Science Reports* **70**, 1–41 (2015).

[22] Novotny, L. Strong coupling, energy splitting, and level crossings: A classical perspective. *American Journal of Physics* **78**, 1199 (2010).

[23] Drexhage, K. Influence of a dielectric interface on fluorescent decay time. *Journal of Luminescence* **2**, 693–701 (1970).

[24] Maier, S. *Plasmonics: Fundamentals and Applications: Fundamentals and Applications* (Springer, 2007).

[25] Kress, S. J. P. *et al.* Wedge Waveguides and Resonators for Quantum Plasmonics. *Nano Letters* 150820154341001 (2015).

[26] Bermúdez-Ureña, E. *et al.* Coupling of individual quantum emitters to channel plasmons. *Nature Communications* **6**, 7883 (2015).

[27] Novotny, L. & van Hulst, N. Antennas for light. *Nature Photonics* **5**, 83–90 (2011).

[28] Kinkhabwala, A. *et al.* Large single-molecule fluorescence enhancements produced by a bowtie nanoantenna. *Nature Photonics* **3**, 654–657 (2009).

[29] Punj, D. *et al.* A plasmonic 'antenna-in-box' platform for enhanced single-molecule analysis at micromolar concentrations. *Nature nanotechnology* **8**, 512–6 (2013).

[30] Aouani, H. *et al.* Bright unidirectional fluorescence emission of molecules in a nanoaperture with plasmonic corrugations. *Nano Letters* **11**, 637–644 (2011).

[31] Curto, A. G. *et al.* Unidirectional emission of a quantum dot coupled to a nanoantenna. *Science (New York, N.Y.)* **329**, 930–3 (2010).

[32] Froufe-Pérez, L., Carminati, R. & Sáenz, J. Fluorescence decay rate statistics of a single molecule in a disordered cluster of nanoparticles. *Physical Review A* **76**, 013835 (2007).

[33] Sapienza, R. *et al.* Observation of resonant behavior in the energy velocity of diffused light. *Phys. Rev. Lett.* **99**, 233902 (2007).

[34] Birowosuto, M. D., Skipetrov, S. E., Vos, W. L. & Mosk, a. P. Observation of Spatial Fluctuations of the Local Density of States in Random Photonic Media. *Physical Review Letters* **105**, 013904 (2010).

[35] Krachmalnicoff, V., Castanié, E., De Wilde, Y. & Carminati, R. Fluctuations of the Local Density of States Probe Localized Surface Plasmons on Disordered Metal Films. *Physical Review Letters* **105**, 1–4 (2010).

[36] Castanié, E. *et al.* Distance dependence of the local density of states in the near field of a disordered plasmonic film. *Opt. Lett.* **37**, 3006–3008 (2012).

[37] Krachmalnicoff, V. *et al.* Towards a full characterization of a plasmonic nanostructure with a fluorescent near-field probe. *Opt. Express* **21**, 11536–11545 (2013).

[38] Man, W. *et al.* Isotropic band gaps and freeform waveguides observed in hyperuniform disordered photonic solids. *Proceedings of the National Academy of Sciences of the United States of America* 1–6 (2013).

[39] Leseur, O., Pierrat, R. & Carminati, R. High-density hyperuniform materials can be transparent (2015).

[40] Albert, R. & Barabási, A. Statistical mechanics of complex networks. *Reviews of modern physics* **74** (2002).

[41] Newman, M. The physics of networks. *Physics Today* **61**, 33 (2008).

[42] Lawandy, N. M., Balachandran, R. M., Gomes, A. S. L. & Sauvain, E. Laser action in strongly scattering media. *Nature* **368**, 436–438 (1994).

[43] Wiersma, D. The physics and applications of random lasers. *Nature Physics* **4** (2008).

[44] Cao, H. Review on latest developments in random lasers with coherent feedback. *Journal of Physics A: Mathematical and General* **39**, 467 (2006).

[45] Ghofraniha, N. *et al.* Experimental evidence of replica symmetry breaking in random lasers. *Nature communications* **6**, 6058 (2015).

[46] Goodman, J. *Introduction to Fourier Optics.* McGraw-Hill physical and quantum electronics series (Roberts & Company, 2005).

[47] Akimov, A. V. *et al.* Generation of single optical plasmons in metallic nanowires coupled to quantum dots. *Nature* **450**, 402–6 (2007).

[48] Chang, D., Sørensen, A., Hemmer, P. & Lukin, M. Quantum Optics with Surface Plasmons. *Physical Review Letters* **97**, 053002 (2006).

[49] Le Kien, F., Gupta, S. D., Nayak, K. P. & Hakuta, K. Nanofiber-mediated radiative transfer between two distant atoms. *Physical Review A - Atomic, Molecular, and Optical Physics* **72**, 1–11 (2005).

[50] Nayak, K. P. *et al.* Optical nanofiber as an efficient tool for manipulating and probing atomic Fluorescence. *Optics express* **15**, 5431–5438 (2007).

[51] Vetsch, E. *et al.* Optical interface created by laser-cooled atoms trapped in the evanescent field surrounding an optical nanofiber. *Physical Review Letters* **104**, 1–4 (2010).

[52] Chang, D. E., Cirac, J. I. & Kimble, H. J. Self-organization of atoms along a nanophotonic waveguide. *Physical Review Letters* **110**, 1–6 (2013).

[53] Arcari, M. *et al.* Near-Unity Coupling Efficiency of a Quantum Emitter to a Photonic Crystal Waveguide. *Physical Review Letters* **113**, 093603 (2014).

[54] Fujiwara, M., Toubaru, K., Noda, T., Zhao, H.-Q. & Takeuchi, S. Highly efficient coupling of photons from nanoemitters into single-mode optical fibers. *Nano letters* **11**, 4362–5 (2011).

[55] Yalla, R., Le Kien, F., Morinaga, M. & Hakuta, K. Efficient channeling of fluorescence photons from single quantum dots into guided modes of optical nanofiber. *Physical Review Letters* **109**, 1–5 (2012).

[56] Klimov, V. V. & Ducloy, M. Spontaneous emission rate of an excited atom placed near a nanofiber. *Physical Review A* **69**, 013812 (2004).

[57] Kolchin, P. *et al.* High Purcell Factor Due To Coupling of a Single Emitter to a Dielectric Slot Waveguide. *Nano Letters* **15**, 464–468 (2015).

[58] Benabid, F., Knight, J. C., Antonopoulos, G. & Russell, P. S. J. Stimulated Raman scattering in hydrogen-filled hollow-core photonic crystal fiber. *Science (New York, N.Y.)* **298**, 399–402 (2002).

[59] Faez, S., Türschmann, P., Haakh, H. R., Götzinger, S. & Sandoghdar, V. Coherent Interaction of Light and Single Molecules in a Dielectric Nanoguide. *Physical Review Letters* **113**, 213601 (2014).

[60] Persano, L., Camposeo, A. & Pisignano, D. Active polymer nanofibers for photonics, electronics, energy generation and micromechanics. *Progress in Polymer Science* **43**, 48–95 (2014).

[61] Lounis, B., Bechtel, H., Gerion, D., Alivisatos, P. & Moerner, W. Photon antibunching in single CdSe/ZnS quantum dot fluorescence. *Chemical Physics Letters* **329**, 399–404 (2000).

[62] Lounis, B. & Moerner, W. E. Single photons on demand from a single molecule at room temperature. *Nature* **407**, 491–493 (2000).

[63] Tien, P. K. Light waves in thin films and integrated optics. *Applied optics* **10**, 2395–2413 (1971).

[64] Snyder, A. & Love, J. *Optical Waveguide Theory* (Springer US, 2012).

[65] Goban, a. *et al.* Atom-light interactions in photonic crystals. *Nature communications* **5**, 3808 (2014).

[66] Mayer, K. M. & Hafner, J. H. Localized Surface Plasmon Resonance Sensors. *Chemical Reviews* **111**, 3828–3857 (2011).

[67] Mivelle, M., van Zanten, T. S. & Garcia-Parajo, M. F. Hybrid Photonic Antennas for Subnanometer Multicolor Localization and Nanoimaging of Single Molecules. *Nano Letters* **14**, 4895–4900 (2014).

[68] Kauranen, M. & Zayats, A. V. Nonlinear plasmonics. *Nature Photonics* **6**, 737–748 (2012).

[69] Averitt, R. D., Westcott, S. L. & Halas, N. J. Linear optical properties of gold nanoshells. *Journal of the Optical Society of America B* **16**, 1824 (1999).

[70] Aizpurua, J. *et al.* Optical Properties of Gold Nanorings. *Physical Review Letters* **90**, 057401 (2003).

[71] Aubry, A. *et al.* Plasmonic light-harvesting devices over the whole visible spectrum. *Nano Letters* **10**, 2574–2579 (2010).

[72] Nordlander, P., Oubre, C., Prodan, E., Li, K. & Stockman, M. I. Plasmon Hybridization in Nanoparticle Dimers. *Nano Letters* **4**, 899–903 (2004).

[73] Romero, I., Aizpurua, J., Bryant, G. W. & García De Abajo, F. J. Plasmons in nearly touching metallic nanoparticles: singular response in the limit of touching dimers. *Optics express* **14**, 9988–99 (2006).

[74] Esteban, R., Taylor, R. W., Baumberg, J. J. & Aizpurua, J. How chain plasmons govern the optical response in strongly interacting self-assembled metallic clusters of nanoparticles. *Langmuir : the ACS journal of surfaces and colloids* **28**, 8881–90 (2012).

[75] Kabashin, A. V. *et al.* Plasmonic nanorod metamaterials for biosensing. *Nat. Mater.* **8**, 867–871 (2009).

[76] Chen, S. *et al.* How To Light Special Hot Spots in Multiparticle-Film Configurations. *ACS Nano* acsnano.5b05605 (2015).

[77] Gopinath, A., Boriskina, S. V., Feng, N.-N., Reinhard, B. M. & Dal Negro, L. Photonic-plasmonic scattering resonances in deterministic aperiodic structures. *Nano Lett.* **8**, 2423–31 (2008).

[78] Afshinmanesh, F., Curto, A. G., Milaninia, K. M., van Hulst, N. F. & Brongersma, M. L. Transparent metallic fractal electrodes for semiconductor devices. *Nano letters* **14**, 5068–74 (2014).

[79] Yu, N. *et al.* Light propagation with phase discontinuities: generalized laws of reflection and refraction. *Science* **334**, 333–7 (2011).

[80] Grésillon, S. *et al.* Experimental Observation of Localized Optical Excitations in Random Metal-Dielectric Films. *Physical Review Letters* **82**, 4520–4523 (1999).

[81] Stockman, M., Faleev, S. & Bergman, D. Localization versus Delocalization of Surface Plasmons in Nanosystems: Can One State Have Both Characteristics? *Physical Review Letters* **87**, 167401 (2001).

[82] Seal, K. *et al.* Coexistence of localized and delocalized surface plasmon modes in percolating metal films. *Phys. Rev. Lett.* **97**, 206103 (2006).

[83] Bondareff, P., Volpe, G., Gigan, S. & Gresillon, S. Probing Extended Modes on Disordered Plasmonic Networks by Wavefront Shaping. *ACS Photonics* **2**, 1658–1662 (2015).

[84] Frimmer, M., Chen, Y. & Koenderink, A. F. Scanning emitter lifetime imaging microscopy for spontaneous emission control. *Phys. Rev. Lett.* **107**, 123602 (2011).

[85] Sapienza, R. *et al.* Deep-subwavelength imaging of the modal dispersion of light. *Nat Mater* **11**, 781–787 (2012).

[86] Joulain, K., Carminati, R., Mulet, J.-P. & Greffet, J.-J. Definition and measurement of the local density of electromagnetic states close to an interface 538–539 (2004).

[87] Vignolini, S. *et al.* Polarization-sensitive near-field investigation of photonic crystal microcavities. *Appl. Phys. Lett.* **94**, 163102 (2009).

[88] Colas des Francs, G., Girard, C., Weeber, J.-C. & Dereux, A. Relationship between scanning near-field optical images and local density of photonic states. *Chem. Phys. Lett.* **345**, 512–516 (2001).

[89] Vallée, R. A. L., Van Der Auweraer, M., De Schryver, F. C., Beljonne, D. & Orrit, M. A microscopic model for the fluctuations of local field and spontaneous emission of single molecules in disordered media. *ChemPhysChem* **6**, 81–91 (2005).

[90] Vallée, R. A. L., Tomczak, N., Kuipers, L., Vancso, G. J. & van Hulst, N. F. Single molecule lifetime fluctuations reveal segmental dynamics in polymers. *Phys. Rev. Lett.* **91**, 038301 (2003).

[91] García, P. D., Stobbe, S., Söllner, I. & Lodahl, P. Nonuniversal intensity correlations in a two-dimensional anderson-localizing random medium. *Phys. Rev. Lett.* **109**, 253902 (2012).

[92] Sapienza, R. *et al.* Long-tail statistics of the purcell factor in disordered media driven by near-field interactions. *Phys. Rev. Lett.* **106**, 163902 (2011).

[93] Cazé, A., Pierrat, R. & Carminati, R. Radiative and non-radiative local density of states on disordered plasmonic films. *Photonics and Nanostructures - Fundamentals and Applications* **10**, 339–344 (2012).

[94] Cazé, A., Pierrat, R. & Carminati, R. Spatial Coherence in Complex Photonic and Plasmonic Systems. *Physical Review Letters* **110**, 063903 (2013).

[95] Duan, H., Fernández-Domínguez, A. I., Bosman, M., Maier, S. a. & Yang, J. K. W. Nanoplasmonics: classical down to the nanometer scale. *Nano letters* **12**, 1683–9 (2012).

[96] Gopinath, A., Boriskina, S. V., Reinhard, B. M. & Negro, L. D. Deterministic aperiodic arrays of metal nanoparticles for surface-enhanced raman scattering (sers). *Opt. Express* **17**, 3741–3753 (2009).

[97] Brinks, D., Castro-Lopez, M., Hildner, R. & van Hulst, N. F. Plasmonic antennas as design elements for coherent ultrafast nanophotonics. *Proceedings of the National Academy of Sciences* **110**, 18386–18390 (2013).

[98] Aharony, A. & Stauffer, D. *Introduction To Percolation Theory* (Taylor & Francis, 2003).

[99] Taminiau, T. H., Stefani, F. D. & van Hulst, N. F. Optical nanorod antennas modeled as cavities for dipolar emitters: Evolution of sub- and super-radiant modes. *Nano Letters* **11**, 1020–1024 (2011). PMID: 21322590.

[100] Kinkhabwala, A. *et al.* Large single-molecule fluorescence enhancements produced by a bowtie nanoantenna. *Nat Photon* **3**, 654–657 (2009).

[101] Losquin, A. *et al.* Experimental evidence of nanometer-scale confinement of plasmonic eigenmodes responsible for hot spots in random metallic films. *Phys. Rev. B* **88**, 115427 (2013).

[102] Beversluis, M. R., Bouhelier, A. & Novotny, L. Continuum generation from single gold nanostructures through near-field mediated intraband transitions. *Phys. Rev. B* **68**, 115433 (2003).

[103] Kirkpatrick, S. Percolation and conduction. *Rev. Mod. Phys.* **45**, 574–588 (1973).

[104] Redding, B., Choma, M. A. & Cao, H. Speckle-free laser imaging using random laser illumination. *Nat Phot.* **6**, 355–359 (2012).

[105] Deng, C. *et al.* Conjugated polymer-titania nanoparticle hybrid films: random lasing action and ultrasensitive detection of explosive vapors. *The journal of physical chemistry. B* **114**, 4725–30 (2010).

[106] Choi, S. H. & Kim, Y. L. The potential of naturally occurring lasing for biological and chemical sensors. *Biomedical Engineering Letters* **4**, 201–212 (2014).

[107] Wan Ismail, W. Z., Liu, G., Zhang, K., Goldys, E. M. & Dawes, J. M. Dopamine sensing and measurement using threshold and spectral measurements in random lasers. *Optics Express* **24**, A85 (2016).

[108] Gottardo, S. *et al.* Resonance-driven random lasing. *Nat Phot.* **2**, 429–432 (2008).

[109] Uppu, R. & Mujumdar, S. Persistent coherent random lasing using resonant scatterers. *Opt. Express* **19**, 23523–23531 (2011).

[110] El-Dardiry, R. G. & Lagendijk, A. Tuning random lasers by engineered absorption. *Applied Physics Letters* **98**, 161106–161106–3 (2011).

[111] Bachelard, N., Andreasen, J., Gigan, S. & Sebbah, P. Taming random lasers through active spatial control of the pump. *Phys. Rev. Lett.* **109**, 033903 (2012).

[112] Hisch, T., Liertzer, M., Pogany, D., Mintert, F. & Rotter, S. Pump-controlled directional light emission from random lasers. *Phys. Rev. Lett.* **111**, 023902 (2013).

[113] Bachelard, N., Gigan, S., Noblin, X. & Sebbah, P. Adaptive pumping for spectral control of random lasers. *Nat. Phys.* **10**, 426–431 (2014).

[114] Chandrasekhar, S. *Radiative Transfer.* Dover Books on Intermediate and Advanced Mathematics (Dover Publications, 1960).

[115] van Rossum, M. C. W. & Nieuwenhuizen, T. M. Multiple scattering of classical waves: microscopy, mesoscopy, and diffusion. *Reviews of Modern Physics* **71**, 313–371 (1999).

[116] John, S. & Pang, G. Theory of lasing in a multiple-scattering medium. *Phys. Rev. A* **54**, 3642–3652 (1996).

[117] Wiersma, D. & Lagendijk, A. Light diffusion with gain and random lasers. *Physical Review E* **54**, 4256–4265 (1996).

[118] El-Dardiry, R. G. S., Mooiweer, R. & Lagendijk, A. Experimental phase diagram for random laser spectra. *New Journal of Physics* **14**, 113031 (2012).

[119] Balachandran, R. M., Lawandy, N. M. & Moon, J. A. Theory of laser action in scattering gain media. *Opt. Lett.* **22**, 319–321 (1997).

[120] Berger, G. A., Kempe, M. & Genack, A. Z. Dynamics of stimulated emission from random media. *Phys. Rev. E* **56**, 6118–6122 (1997).

[121] Mujumdar, S., Ricci, M., Torre, R. & Wiersma, D. S. Amplified extended modes in random lasers. *Phys. Rev. Lett.* **93**, 053903 (2004).

[122] Pierrat, R. & Carminati, R. Threshold of random lasers in the incoherent transport regime. *Phys. Rev. A* **76**, 023821 (2007).

[123] Türeci, H. E., Stone, A. D. & Collier, B. Self-consistent multimode lasing theory for complex or random lasing media. *Phys. Rev. A* **74**, 043822 (2006).

[124] Tureci, H. E., Stone, A. D., Ge, L., Rotter, S. & Tandy, R. J. Ab initio self-consistent laser theory and random lasers. *Nonlinearity* **22**, C1 (2009).

[125] Jiang, X. & Soukoulis, C. M. Time dependent theory for random lasers. *Phys. Rev. Lett.* **85**, 70–73 (2000).

[126] Sebbah, P. & Vanneste, C. Random laser in the localized regime. *Phys. Rev. B* **66**, 144202 (2002).

[127] Conti, C., Angelani, L. & Ruocco, G. Light diffusion and localization in three-dimensional nonlinear disordered media. *Phys. Rev. A* **75**, 033812 (2007).

[128] Holzer, W. *et al.* Photo-physical characterization of rhodamine 6G in a 2-hydroxyethyl-methacrylate methyl-methacrylate copolymer. *Chemical Physics* **256**, 125–136 (2000).

[129] van Soest, G., Tomita, M. & Lagendijk, A. Amplifying volume in scattering media. *Opt. Lett.* **24**, 306–308 (1999).

[130] Bohren, C. F. & Huffman, D. *Absorption and scattering of light by small particles.* Wiley science paperback series (Wiley, 1983).

[131] Wiersma, D. D. & Cavalieri, S. Temperature-controlled random laser action in liquid crystal infiltrated systems. *Physical Review E* **66**, 056612 (2002).

[132] Homola, J. Surface plasmon resonance sensors for detection of chemical and biological species. *Chemical reviews* **108**, 462–493 (2008).

[133] Rose, A., Zhu, Z., Madigan, C. F., Swager, T. M. & Bulović, V. Sensitivity gains in chemosensing by lasing action in organic polymers. *Nature* **434**, 876–879 (2005).

[134] Fan, X. & Yun, S.-H. The potential of optofluidic biolasers. *Nature methods* **11**, 141–7 (2014).

[135] Hokr, B. H. *et al.* Single-shot stand-off chemical identification of powders using random Raman lasing. *Proceedings of the National Academy of Sciences of the United States of America* **111**, 12320–4 (2014).

[136] Cortese, L. *et al.* Anisotropic Light Transport in White Beetle Scales. *Advanced Optical Materials* n/a–n/a (2015).

[137] Polson, R. C. & Vardeny, Z. V. Random lasing in human tissues. *Applied Physics Letters* **85**, 1289–1291 (2004).

[138] Song, Q. *et al.* Random lasing in bone tissue. *Optics letters* **35**, 1425–7 (2010).

[139] Cao, H. *et al.* Spatial confinement of laser light in active random media. *Physical Review Letters* **84**, 5584–5587 (2000).

[140] Humar, M. & Hyun Yun, S. Intracellular microlasers. *Nature Photonics* **9**, 572–576 (2015).

[141] Schubert, M. *et al.* Lasing within Live Cells Containing Intracellular Optical Microresonators for Barcode-Type Cell Tagging and Tracking. *Nano Letters* **15**, 5647–5652 (2015).

[142] Ho Choi, S. & Kim, Y. L. Random lasing mode alterations by single-nanoparticle perturbations. *Applied Physics Letters* **100**, 041101 (2012).

[143] Chen, L. *et al.* Highly sensitive biological and chemical sensors based on reversible fluorescence quenching in a conjugated polymer. *Proc. Nat. Acad. Sci.* **96**, 12287–92 (1999).

[144] Demchenko, A. *Introduction to Fluorescence Sensing.* Biomedical and Life Sciences (Springer Netherlands, 2008).

[145] Vázquez, M. E., Blanco, J. B. & Imperiali, B. Photophysics and biological applications of the environment-sensitive fluorophore 6-N,N-dimethylamino-2,3-naphthalimide. *Journal of the American Chemical Society* **127**, 1300–1306 (2005).

[146] Omenetto, F. G. & Kaplan, D. L. New opportunities for an ancient material. *Science (New York, N.Y.)* **329**, 528–31 (2010).

[147] Magde, D., Wong, R. & Seybold, P. G. Fluorescence quantum yields and their relation to lifetimes of rhodamine 6G and fluorescein in nine solvents: improved absolute standards for quantum yields. *Photochemistry and photobiology* **75**, 327–334 (2002).